

# Purification of Liquid Scintillator and Monte Carlo Simulations of Relevant Internal Backgrounds in SNO+

by

Sarah Elizabeth Quirk

A thesis submitted to the Department of Physics, Engineering Physics and  
Astronomy in conformity with the requirements for the degree of Master of Science

Queen's University

Kingston, Ontario, Canada

January 2008

Copyright ©Sarah Quirk, 2008

# Abstract

The SNO+ experiment has begun research and development to engineer replacing the heavy water in the Sudbury Neutrino Observatory with liquid scintillator in order to study low energy solar neutrinos, double beta decay, and many other exciting physics topics. Experimentation and simulation have been combined to evaluate the purification of the liquid scintillator, linear alkylbenzene, for the SNO+ project. Four radiopurification methods were tested: water and acid extraction, adsorption and distillation. The combination of adsorption and distillation yielded the best results with a reduction factor of 10000. Optical purification tests showed that double distillation and the combination of adsorption and distillation provided the best method of removing optical impurities from the liquid scintillator. Simulation studies showed that it is necessary to minimize internal radioisotopes:  $^{210}\text{Bi}$ ,  $^{210}\text{Pb}$ , uranium chain, thorium chain, and  $^{40}\text{K}$  in order to achieve desired uncertainty levels in the measurement of the *pep* solar neutrino signal.

# Acknowledgments

First and foremost I would like to thank my supervisor, Mark Chen, who has made my experience here at Queen's very enjoyable and really helped give me a solid foundation in my research. He was always available for my questions and emails, while allowing me the freedom to work independently.

Next, I would like to thank the rest of the SNO+ group, your questions, comments and ideas have really helped me with my research. Specifically, I would like to thank Xin Dai, who taught me everything I know about purification and for all the fun (long) days in the lab that we shared. I would also like to thank Alex Wright for always taking the time to answer my questions, helping me with my code and helping me get rid of the pests in my apartment. I would also like to thank the rest of my colleagues and friends at Queens; I've enjoyed sharing the basement with you for the last two years. Thanks to Ryan, Jennifer, Jay and Ben for jumping on board when I started the basketball team, for almost winning at volleyball every year, and to the rest of the gang, Mark, Ryan, John, Jeff, Paradorn and anyone else I'm forgetting for a very memorable time at Queen's.

I would like to thank my parents for their support throughout this whole process. I would also like to thank my sister, Amanda, who came to visit me often, proof read my thesis, helped with chemistry, and was never more than a phone call or an instant message away. Lastly I would like to thank David for late night trips to the lab, bringing me lunch, always being there to brighten my day and for keeping me sane.

# Contents

Abstract . . . . .	i
Acknowledgments . . . . .	ii
List of Tables . . . . .	vi
List of Figures . . . . .	viii
<b>Chapter 1. Introduction</b>	<b>1</b>
1.1 Objectives and Motivation . . . . .	2
1.2 Scope of Thesis . . . . .	2
<b>Chapter 2. Solar Neutrinos</b>	<b>4</b>
2.1 Standard Solar Models . . . . .	5
2.2 Solar Experiments . . . . .	9
2.2.1 Radiochemical Experiments . . . . .	10
2.2.2 Water Čerenkov Experiments . . . . .	13
2.2.3 Liquid Scintillator Experiments . . . . .	16
2.3 Neutrino Oscillations . . . . .	19
<b>Chapter 3. SNO+ Introduction</b>	<b>26</b>
3.1 Transition from SNO . . . . .	26
3.2 The Science and Motivation . . . . .	28
3.2.1 CNO and <i>pep</i> Neutrinos . . . . .	29
3.2.2 Survival Probability . . . . .	29

3.2.3	Neutrinoless Double Beta Decay . . . . .	31
3.2.4	Geo-neutrinos . . . . .	31
3.3	The Liquid Scintillator . . . . .	32
3.3.1	Linear Alkylbenzene . . . . .	33
3.4	Neutrino Signal in SNO+ . . . . .	34
3.5	The Backgrounds in SNO+ . . . . .	36
3.5.1	Internal Backgrounds . . . . .	36
3.5.2	External Backgrounds . . . . .	40
<b>Chapter 4. Radiopurification Results and Analysis</b>		<b>42</b>
4.1	Spike Setup . . . . .	43
4.2	$\beta$ - $\alpha$ Counting Technique . . . . .	48
4.3	Water and Acid Extraction . . . . .	52
4.4	Adsorption . . . . .	57
4.5	Vacuum Distillation . . . . .	64
4.6	Conclusions from Purification Tests . . . . .	73
<b>Chapter 5. Optical Purity</b>		<b>75</b>
5.1	Adsorption Column . . . . .	76
5.2	Other Optical Tests . . . . .	78
5.3	Optical Purification Conclusions . . . . .	79
<b>Chapter 6. Simulation of Background Effects on Signal</b>		<b>81</b>
6.1	Preliminary Code . . . . .	83
6.1.1	Enhanced Code: Low energy alphas, equilibrium constraints, $^7\text{Be}$ and $^8\text{B}$ spectra. . . . .	85
6.2	Sensitivity Studies . . . . .	89
6.3	Constraining lead via bismuth and polonium . . . . .	94
6.3.1	Results of $^{210}\text{Po}$ Constraint . . . . .	94

---

Chapter 7. Summary and Conclusion	97
References . . . . .	100

# List of Tables

2.1	Solar input parameters. . . . .	6
2.2	Solar neutrino fluxes . . . . .	6
3.1	Background purification level goals for SNO+ . . . . .	37
3.2	Known internal backgrounds . . . . .	38
3.3	Amount of external radioactivity in major components of SNO+ . . . . .	41
4.1	Activities from first small spike. . . . .	45
4.2	Activities from small spike . . . . .	46
4.3	Raw data from LAB extraction from spiked UPW . . . . .	54
4.4	Results from water extraction from spiked LAB . . . . .	54
4.5	Raw data from LAB extraction from spiked UPW . . . . .	54
4.6	Results from LAB extraction from spiked UPW . . . . .	55
4.7	Raw data from hot water extraction test . . . . .	55
4.8	Results from hot water extraction from spiked LAB . . . . .	55
4.9	Raw data from acid extraction test . . . . .	56
4.10	Results from acid extraction from spiked LAB . . . . .	56
4.11	Raw data from preliminary results for adsorption tests . . . . .	59
4.12	Preliminary results from adsorption tests. . . . .	60
4.13	Raw data from secondary adsorption tests . . . . .	60
4.14	Results from secondary adsorption tests . . . . .	61

---

4.15	Raw data from equilibrium and desorption tests . . . . .	62
4.16	Results from equilibrium and desorption tests. Tests are completed for different stirring times. . . . .	62
4.17	Raw data from Al <sub>2</sub> O <sub>3</sub> exhaustion tests . . . . .	63
4.18	Results to determine if Al <sub>2</sub> O <sub>3</sub> can be quickly exhausted. . . . .	63
4.19	Raw data from initial vacuum distillation tests. . . . .	65
4.20	Vacuum distillation results. . . . .	66
4.21	Activities from new, larger spike. . . . .	68
4.22	Raw data from vacuum distillation tests . . . . .	72
4.23	Results from purification tests using the larger spike setup. Results included are from tests using distillation, distillation plus alumina ad- sorption and double distillation. . . . .	72
6.1	Table of expected internal backgrounds, with values based on Kam- LAND's post-purification levels. . . . .	82
6.2	Input values for simulation . . . . .	83

# List of Figures

2.1	Proton-proton chains . . . . .	7
2.2	CNO reaction chains . . . . .	8
2.3	Neutrino spectrum . . . . .	8
2.4	Electron neutrino survival probability . . . . .	25
3.1	Probing vacuum-matter transition with pep measurement . . . . .	30
3.2	Neutrino signal measured in SNO+ . . . . .	35
3.3	Uranium and thorium decay chains . . . . .	39
4.1	Spike setup for lead tests . . . . .	44
4.2	Photograph of spike setup . . . . .	47
4.3	Beta - alpha coincidence decays . . . . .	49
4.4	Beta-alpha coincidence counting detector . . . . .	49
4.5	$\beta$ - $\alpha$ counting system schematic . . . . .	50
4.6	Circuit diagram . . . . .	50
4.7	Liquid-liquid extraction . . . . .	52
4.8	Depiction of impurities being adsorbed onto a bead of $\text{Al}_2\text{O}_3$ . . . . .	58
4.9	Vacuum distillation setup. . . . .	65
4.10	New Spike Set Up . . . . .	67
4.11	Thorium free spike . . . . .	69
5.1	Alumina column set up. . . . .	77

---

5.2	Results from optical purification alumina tests. . . . .	78
5.3	Results from all optical purification tests . . . . .	80
6.1	Old code, with only high energy betas, energy threshold of 700 keV. . . . .	84
6.2	Preliminary neutrino spectrum . . . . .	84
6.3	Decay events constrained by equilibrium . . . . .	86
6.4	New code, with addition of low energy alphas, energy threshold of 400 keV, and equilibrium used to constraint in fit. . . . .	87
6.5	Enhanced neutrino spectrum . . . . .	88
6.6	Similar spectrum as Figure 6.5 with an expanded low energy region 0-1.5 MeV . . . . .	88
6.7	Thorium chain sensitivity studies . . . . .	91
6.8	Uranium chain sensitivity studies . . . . .	92
6.9	Argon and krypton sensitivity studies. . . . .	93
6.10	Potassium sensitivity studies. . . . .	93
6.11	Comparison of constraint to no constraint of bismuth . . . . .	95
6.12	Comparison of constraint to no constraint of bismuth, three live time years . . . . .	96

# Chapter 1

## Introduction

The Sudbury Neutrino Observatory (SNO) is starting a new phase after very successful results during its three heavy water phases. The new stage of SNO is called SNO+ which stands for SNO plus liquid scintillator. It involves replacing the heavy water in the SNO detector with an organic liquid scintillator. This transformation will boost the light yield by a factor of fifty, detecting scintillation light instead of Čerenkov radiation. SNO+ is able to use the existing infrastructure and electronics of SNO and minimal engineering adjustments are needed to transform the existing detector into a liquid scintillator detector.

SNO+ will be sensitive to a wide range of new physics objectives and it will operate in two phases: a solar neutrino phase and a neutrinoless double beta decay phase. The solar neutrino phase will be sensitive to low energy solar neutrinos including *pep* (part of the proton-proton reaction chain) and CNO (carbon-nitrogen-oxygen cycle) neutrinos. As well this low energy range will allow measurements that contribute to precise calculations of neutrino oscillation parameters. The double beta decay phase involves adding an isotope that may undergo neutrinoless double beta decay, detected in the SNO+liquid scintillator. There is also the possibility to study geoneutrinos and reactor neutrinos during the solar neutrino phase of SNO+ without having to alter

the detector in any way.

## 1.1 Objectives and Motivation

For the solar neutrino phase of SNO+, the physics of interest exists in the low energy range of the neutrino spectrum. One of the most important challenges that SNO+ is faced with is internal backgrounds in this energy range of interest. These backgrounds need to be studied so that they can be understood and minimized. Specifically, the following objectives were pursued:

1. To create detailed sensitivity studies to determine how fluctuations and constraints of background levels affect the uncertainty of the physics of interest
2. To investigate methods of removing radio-impurities , specifically  $^{212}\text{Pb}$ , from the liquid scintillator
3. To evaluate methods to improve the optical purity of the liquid scintillator

## 1.2 Scope of Thesis

This thesis is divided into seven chapters. Following this introduction is an overview of solar neutrino physics and relevant theory pertaining to the physics of interest for the SNO+ experiment. Chapter 3 gives an overview of the physics goals of SNO+. Chapter 4 details the radio-purification methods used and results from all purification tests. Chapter 5 uses the results from the radio-purification tests to determine which purification methods will be used to improve the optical purity of the liquid scintillator. Background studies are investigated in Chapter 6 with detailed simulations of the solar neutrino energy spectrum and effects of background levels on the uncertainties of the physical parameters of interest, in particular the *pep* neutrino flux. Finally,

Chapter 7 provides concluding remarks and a summary of the knowledge obtained from these studies.

# Chapter 2

## Solar Neutrinos

According to the standard model of particle physics, neutrinos are massless, neutral particles. There are three different *flavours* of neutrinos: electron ( $\nu_e$ ), muon ( $\nu_\mu$ ), and tau ( $\nu_\tau$ ) neutrinos, corresponding to their respective leptons. The neutrino was first proposed by Wolfgang Pauli in 1930 to preserve energy conservation in beta decay. The first successful neutrino detection was made by F. Reines and C. L. Cowan *et al.* [1].

Neutrinos are produced in large quantities; a human on Earth has approximately  $10^{16}$  neutrinos passing through them every second. There are many sources of neutrinos including solar neutrinos, atmospheric neutrinos, neutrinos produced by reactors, neutrinos produced by the Earth, and supernova neutrinos. Solar neutrinos are a result of nuclear reactions in the Sun and are one of the few probes of the solar interior. This is especially interesting as it relates to our Sun and can give very useful information about stellar evolution and stability. Neutrinos only interact through the weak interaction, via W and Z boson exchange. As a result they have a very small interaction cross-section and can travel from the interior of the Sun to Earth completely unhindered. The next sections will review the origin of solar neutrinos as specified by the standard solar model and the solar neutrino experiments that have

been successful in acquiring information on these small neutral particles.

## 2.1 Standard Solar Models

Standard solar model gives a quantitative description of the Sun based on results from solar observations and measurements. It describes the Sun's current state and evolution from the time of its formation billions of years ago, to its current status. There are many different standard solar models with slight variations of some input values, however all are based on similar assumptions. There are a few basic assumptions: *Hydrostatic equilibrium* is an assumed condition for the Sun, with the radiative and particle pressures exactly balancing gravity. In the interior of the Sun, *energy transport* is primarily achieved through photon radiation, although convection dominates on the surface of the Sun and electron conduction has a small contribution in the innermost regions. As well, a small amount of energy is transported via neutrino loss. Energy generation in the Sun is by *nuclear fusion*, burning hydrogen fuel. The sun initially was *homogeneous in composition*; and only over time with nuclear fusion have local abundances of isotopes changed in the solar interior, while the outer layers of the Sun maintain the original composition [2].

There are input parameters (Table 2.1) in the solar model that are of special importance to neutrino physics, including the accurate determination of the solar luminosity, mass and the initial heavy-element-to-hydrogen ratio. The luminosity boundary condition is especially important in the calculation of neutrino fluxes, as both are direct outcomes of nuclear reactions deep in the solar interior.

The nuclear reactions in the core of the Sun are responsible for the production of neutrinos that can be measured here on Earth. There are thought to be two series of nuclear fusion reactions in the Sun that produce the energy-sustaining luminosity and measurable neutrino fluxes: the *proton-proton chain* (Figure 2.1) and the CNO

Quantity	Symbol	Value
Solar mass	$M_{\odot}$	$1.98844(30) \times 10^{30}$ kg
Solar Luminosity	$L_{\odot}$	$(3.846 \pm 0.008) \times 10^{26}$ W
Solar radius	$R_{\odot}$	$6.961 \times 10^8$ m
Initial hydrogen abundance (by mass)	X	0.71
Initial heavy element abundance	Z	0.020
Initial helium abundance	Y	0.27

Table 2.1: Some important solar quantities as input parameters for the solar models [3].

(carbon-nitrogen-oxygen) cycle (Figure 2.2). Table 2.2 outlines these nuclear reactions with rows 1-5 showing the proton chain and rows 6-8 as part of the CNO cycle. It can also be seen in Table 2.2 that the neutrino flux varies in magnitude from the largest at  $6 \times 10^{10} \text{ cm}^{-2}\text{s}^{-1}$  from the pp neutrinos to the smallest from *hep* neutrinos with a flux on the order of  $8 \times 10^3 \text{ cm}^{-2}\text{s}^{-1}$ . Figure 2.3 shows the entire neutrino spectrum with flux as a function of energy. Different solar neutrino experiments have detected neutrinos with different energies from different parts of the solar neutrino spectrum. The energy thresholds for a selection of experiments are indicated by the horizontal lines at the top of Figure 2.3.

Reaction	Source	Solar Neutrino Flux ( $\text{cm}^{-2}\text{s}^{-1}$ )
$p + p \rightarrow {}^2\text{H} + e^+ + \nu_e$	pp	$5.99(1.00 \pm 0.01) \times 10^{10}$
$p + p + e^- \rightarrow {}^2\text{H} + \nu_e$	pep	$1.42(1.00 \pm 0.02) \times 10^8$
${}^3\text{He} + p \rightarrow {}^3\text{He} + e^+ + \nu_e$	hep	$7.93(1.00 \pm 0.16) \times 10^3$
${}^7\text{Be} + e^- \rightarrow {}^7\text{Li} + \gamma$	${}^7\text{Be}$	$4.84(1.00 \pm 0.11) \times 10^9$
${}^8\text{B} \rightarrow {}^2\text{He} + e^+ + \nu_e$	${}^8\text{B}$	$5.69(1.00 \pm 0.16) \times 10^6$
${}^{13}\text{N} \rightarrow {}^{13}\text{C} + e^+ + \nu_e$	${}^{13}\text{N}$	$3.07(1.00^{+0.31}_{-0.28}) \times 10^8$
${}^{15}\text{O} \rightarrow {}^{15}\text{N} + e^+ + \nu_e$	${}^{15}\text{O}$	$2.33(1.00^{+0.33}_{-0.29}) \times 10^8$
${}^{17}\text{F} \rightarrow {}^{17}\text{O} + e^+ + \nu_e$	${}^{17}\text{F}$	$5.84(1.00 \pm 0.52) \times 10^6$

Table 2.2: Most currently, widely used predicted solar neutrino fluxes from the standard solar model [4, 5].

Figure 2.1 shows a schematic of the pp chain, where the pp reaction occurs 99.8% of the time and the *pep* reaction only 0.2% of the time. A measurement of the

*pep* neutrino flux or the *pp* neutrino flux gives equivalent information about this fundamental step in the solar model [6]. Also in Figure 2.1 it is shown that the reactions that take place are split into 3 distinct branches, referred to as *pp* Branch I, II, and III. Figure 2.1 shows pictorial the *pp* reaction chain.

Some of the steps in the CNO reaction cycle are shown in rows 6-8 of Table 2.2 and is also shown pictorially in Figure 2.2. In 1939, this reaction chain was first proposed by Bethe who stated that “the most important source of energy in ordinary stars is the reactions of carbon and nitrogen with protons” [7]. It has been almost 70 years since that pivotal paper and much debate as well as many more papers have been published on the topic. In 2003, Bahcall *et al.* used current solar neutrino experimental data to set an upper limit of 7.8% as the fraction of energy that the Sun produces via the CNO cycle [8]. The standard model prediction of 1.5% of the solar luminosity produced by the CNO cycle is within this upper bound of 7.8%, however a measurement would significantly narrow down the range. To this point, solar neutrino experiments have not been able to make a precise measurement of the CNO flux.

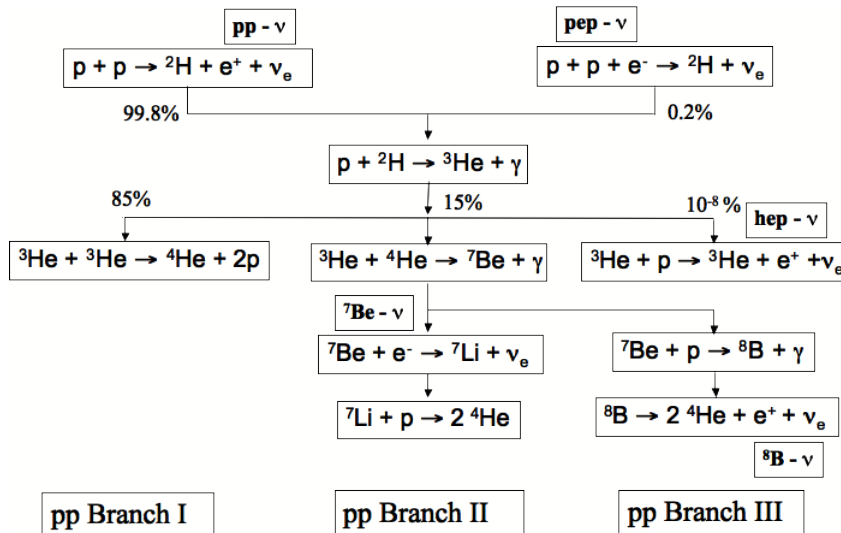


Figure 2.1: *pp* chain reactions in the sun

John Bahcall led the development of standard solar models in neutrino physics.

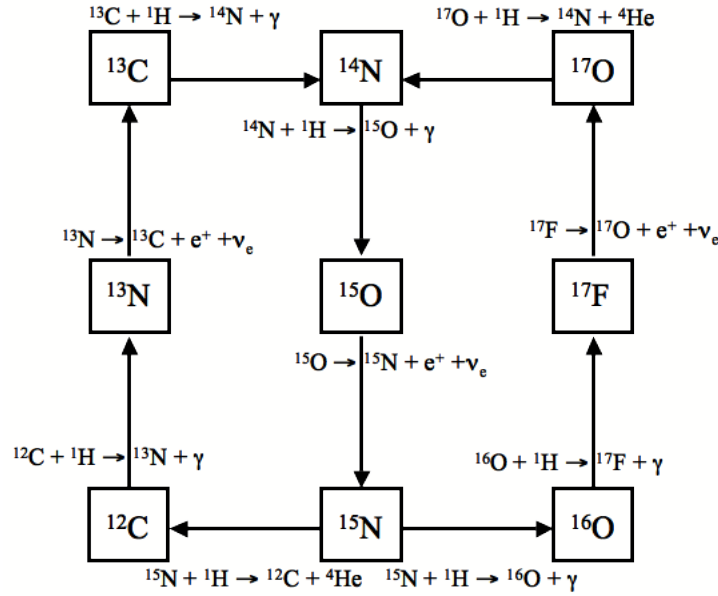


Figure 2.2: CNO reactions chain believed to occur in the sun

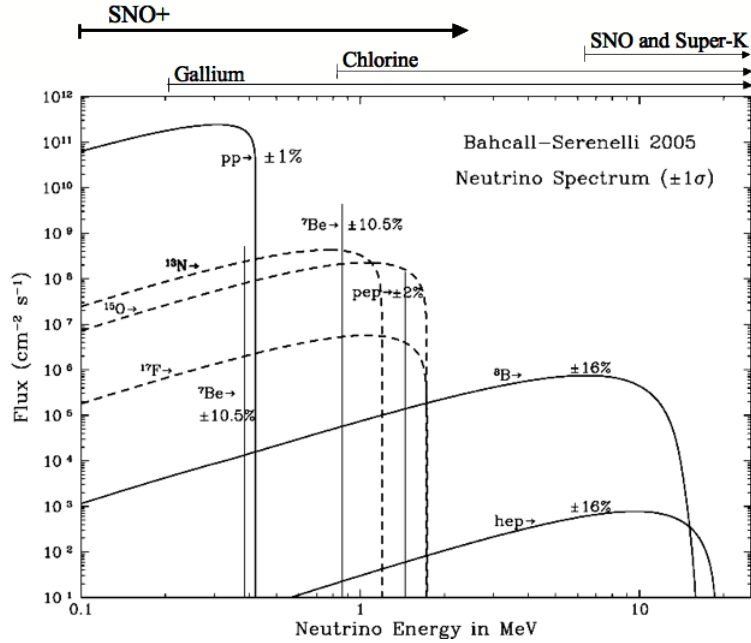


Figure 2.3: Plot of neutrino energy versus neutrino flux for pp, pep, <sup>7</sup>Be, <sup>8</sup>B, hep, and CNO neutrinos. Adapted from [9, 4]

Bahcall calculated the first solar model prediction of neutrino fluxes in 1962 and continued to produce updates as input values changed with updated observations and calculations until his death in 2005 [4, 10, 11, 12, 13, 14, 15, 16]. Over these forty

years the solar models were refined with many changes, reflecting advances made in related fields, including changes in rates for reactions such as  ${}^3\text{He}$ - ${}^3\text{He}$ , theoretical calculations of the pp reaction, and changes in observations of the heavy element to hydrogen ratio in the Sun. With advancements in computer simulations other improvements including revised calculations of stellar radiative opacities and equation of state were able to be made. In recent years, the models that have been most used in the solar neutrino community are BP00 (Bahcall and Pinsonneault, 2000) [14], BP04 (Bahcall and Pinsonneault, 2004) [15], and BS2005 (Bahcall and Serenelli, 2005) [4]. Improvements from BP00 to BP04 include improvements to nuclear fusion cross-sections, changes to the equation of state for the solar interior, including relativistic corrections and a more accurate treatment of molecules, and arguably most important, changes to the surface chemical composition for the Sun, which affect the radiative opacity and physical characteristics of the solar model [9]. Currently the most widely used solar model, BS05, was constructed with newly calculated radiative opacities and newly determined heavy-element abundances.

## 2.2 Solar Experiments

There have been many very successful solar neutrino experiments that have built a solid foundation on which to base new experiments. In the past forty years one of the biggest puzzles in science, the solar neutrino problem, has been investigated and recently solved based on the results of these experiments. The solar neutrino problem was the inconsistency between the theoretical calculations and experimental results of the first experiments discussed below. The first round of experiments were radiochemical experiments, including the Homestake, GALLEX, GNO, and SAGE experiments. Radiochemical experiments do not directly measure the neutrino spectrum, but instead measure the neutrino capture rate ( $R$ ) from the integrated flux. This rate is

measured in the Solar Neutrino Unit (SNU) which is equivalent to 1 neutrino event per second for each  $10^{36}$  target atoms. In the following section large water detectors KamiokaNDE, Super-KamiokaNDE and the Sudbury Neutrino Observatory will be discussed, followed by large liquid scintillator detectors Borexino and KamLAND.

### 2.2.1 Radiochemical Experiments

In 1965, the first solar neutrino experiment was built in an abandoned gold mine in Homestake, South Dakota. The experiment, led by Ray Davis, is often referred to as the Davis experiment, and was built to measure the total flux of solar neutrinos above an energy threshold of 0.814 MeV. The detector is sensitive to only electron type neutrinos, the majority of the measured flux being from  ${}^7\text{Be}$  and  ${}^8\text{B}$  neutrino reactions in the Sun. The experiment was a giant sealed tank of 390000 liters of liquid perchloroethylene ( $\text{C}_2\text{Cl}_4$ ) located 4850 feet underground [17]. The experiment utilizes neutrino capture on chlorine:



Every 60-70 days the argon atoms were extracted from the large volume of chlorine by passing helium through the tanks and removing  ${}^{37}\text{Ar}$  from the gas by a charcoal trap [18, 19]. The radioactive  ${}^{37}\text{Ar}$  was then observed using small proportional counters. After a remarkable 25 years (1970-1995) of data taking, the measured solar neutrino rate from the experiment is [18]:

$$R_{exp} = 2.56 \pm 0.16(\text{statistical}) \pm 0.16(\text{systematic}) \text{ SNU} \quad (2.2)$$

This is much smaller than the standard solar model (SSM) calculated value of [14]:

$$R_{SSM} = 7.6_{-1.1}^{+1.3} \text{ SNU} \quad (2.3)$$

The discrepancy between theoretical prediction and experimental measurement was apparent, although it was not clear to physicists whether the experimental results or the theoretical calculations were incorrect. After much debate and reanalysis of both the theory and the experimental results the discrepancy between the results, became known as the Solar Neutrino Problem.

The Homestake experiment led to a round of neutrino experiments, also chemical in nature, with gallium as the target mass. Two consecutive experiments using gallium as a target were located in Gran Sasso Underground Laboratories. The GALLEX (GALLium EXperiment), a collaboration of Germany, Italy, France, USA, and Israel, ran from 1990-1997 and in 1998, the original collaborators, Italy and Germany, continued the experiment under the new name GNO (Gallium Neutrino Observatory) which took data until the spring of 2003. The target for these experiments was 103 tons of  $\text{GaCl}_3 \cdot \text{HCl}$  in  $\text{H}_2\text{O}$ . The experiment was designed to measure low energy neutrinos, primarily from the proton-proton reaction, with an energy threshold of 0.233 MeV using the reaction:



Typically, the germanium was chemically extracted every three to four weeks and then  ${}^{71}\text{Ge}$  was counted using low background proportional counters. The GALLEX experiment results, from all 65 runs, measure a solar neutrino rate of [20, 21]:

$$R_{exp} = 77.5 \pm 6.2(\text{statistical})_{-4.7}^{+4.3}(\text{systematic}) \text{ SNU} \quad (2.5)$$

The GNO experiment, 58 runs, give a rate of [20, 22]:

$$R_{exp} = 62.9_{-5.3}^{+5.5}(\text{statistical}) \pm 2.5(\text{systematic}) \text{ SNU} \quad (2.6)$$

The combination of the both data sets from GALLEX and GNO, with 123 runs in total, give a rate of [20, 22]:

$$R_{exp} = 69.3 \pm 4.1(\text{statistical}) \pm 3.6(\text{systematic}) \text{ SNU} \quad (2.7)$$

Again, the observed solar neutrino flux is much smaller than the predicted Standard Solar Model prediction [4, 5]:

$$R_{SSM} = 126 \pm 10 \text{ SNU} \quad (2.8)$$

Another gallium radiochemical experiment was performed independently from the GALLEX/GNO collaborations. This experiment was SAGE (ruSsian American Gallium Experiment), located at Baksan Neutrino Observatory in the Caucasus mountains in Russia. SAGE uses the same reaction  ${}^{71}\text{Ga}(\nu_e, e){}^{71}\text{Ge}$  as GALLEX/GNO, but for a target uses 49 tons of metallic gallium. SAGE took data from 1990 to 2001; and had an energy threshold of 0.233 MeV focusing on neutrinos from the proton-proton reaction in the Sun. The SAGE experiment used an exposure time of about four weeks and then extract and count  ${}^{71}\text{Ge}$  with a proportional counter [23].

The SAGE result for the neutrino capture rate was [24]:

$$R_{exp} = 70.8_{-5.2}^{+5.3}(\text{statistical})_{-3.2}^{+3.7}(\text{systematic}) \text{ SNU} \quad (2.9)$$

The results for SAGE are consistent with the results from GALLEX and GNO (Equation 2.5,2.6,2.7) but still considerably lower than the neutrino capture rate as predicted by the solar standard model (Equation 2.8). The gallium experiments did not solve the solar neutrino problem; rather, they gave further backing to the Ray Davis experiment in providing added support that there was not an experimental error occurring as now three independent experiments all reported similar deficits of

solar neutrinos.

### 2.2.2 Water Čerenkov Experiments

Just before GALLEX and SAGE started, there was another type of solar neutrino experiment starting in Japan. The KamiokaNDE (Kamioka Nucleon Decay Experiment) experiment was a large water Čerenkov detector started in 1982 as an experiment to look for proton decay and stability of bound neutrons. In 1985, KamiokaNDE was converted into a neutrino detector and became known as KamiokaNDE II, running from January 1987 to April 1990. It was located in the Mozumi underground mine (2700 m water equivalent) of the Kamioka Mining and Smelting Co. near the city of Hida, Japan. The KamiokaNDE detector was a cylindrical water tank 16.1 m in height and 15.6 m in diameter that contained 3000 tons of ultra-pure water. It was surrounded by 948 photomultiplier tubes (PMTs) that detected the Čerenkov radiation emitted by energetic electrons released in neutrino events. The experiment continued with KamiokaNDE III from December 1990 to February 1995. Unlike the radiochemical detectors that were mainly counting experiments, KamiokaNDE was a real-time experiment that measured the time, the energy and the recoil direction of the event [25, 26, 27]. The measured  ${}^8\text{B}$  solar flux from KamiokaNDE in phase II and III, after 2079 days of data taking, was determined to be [28]:

$$\phi_{exp} = 2.80 \pm 0.19(\text{statistical}) \pm 0.33(\text{systematic}) \times 10^6 \text{ cm}^{-2}\text{s}^{-1} \quad (2.10)$$

The results showed clearly a signal that pointed back to the Sun, but only half the expected rate from the solar standard model (Equation 2.11) [25]:

$$\phi_{SSM} = 5.69(1.00 \pm 0.16) \times 10^6 \text{ cm}^{-2}\text{s}^{-1} \quad (2.11)$$

To improve the KamiokaNDE results, a next generation water Čerenkov detector, Super Kamiokande (Super-K) was built. Located in the same mine (but different cavity), Super-K is larger in volume than KamiokaNDE, with a diameter of 40 m and 50 000 tons of pure water surrounded by about 11,200 photomultiplier tubes. The increased size and enhanced water purity enabled a decrease in energy detection threshold for solar neutrinos to below 5 MeV [25, 29]. After 1496 days of data taking, the results of the  $^8\text{B}$  solar neutrino flux measurement were [30]:

$$\phi_{exp} = 2.35 \pm 0.02(\textit{statistical}) \pm 0.08(\textit{systematic}) \times 10^6 \text{ cm}^{-2}\text{s}^{-1} \quad (2.12)$$

The results from KamiokaNDE and Super-K (Equation 2.10, 2.12) can be compared to the Standard Solar Model prediction for water as the target material [4, 14]. Although Super-K and KamiokaNDE made great progress in advancing neutrino detection with real-time abilities, there was still a deficit in the comparison of theory and experimental measurement.

The next generation large scale experiment was the Sudbury Neutrino Observatory (SNO). The SNO experiment was designed to determine the source of the deficit of observed solar neutrinos and to test one of the suggested theories that solar neutrinos changed flavour on the way from the Sun to Earth. [31]. The SNO detector is 2092 m (6010 m water equivalent) underground and its target mass is 1000 tonnes of heavy water ( $\text{D}_2\text{O}$ ) contained in a transparent acrylic vessel. The vessel is surrounded by 9600 photomultiplier tubes that detect flashes of light produced by neutrino interactions. SNO can detect solar neutrinos through three available neutrino reactions, elastic scattering (Equation 2.13), charged current (Equation 2.14), and neutral current (Equation 2.15)

$$\nu_x + e^- \rightarrow \nu_x + e^- \quad (\text{ES}) \quad (2.13)$$

$$\nu_e + d \rightarrow p + p + e^- \quad (\text{CC}) \quad (2.14)$$

$$\nu_x + d \rightarrow p + n + \nu_x \quad (\text{NC}) \quad (2.15)$$

where  $x = e, \mu, \tau$ , and  $d$  is deuterium. Using these three channels of detection, SNO measured the  $\nu_e$  flux using the charged current reaction and compared it to the flux of all other flavours ( $x = e, \mu, \tau$ ) of neutrinos coming from the Sun, using the neutral current reaction [31]. In the elastic scattering (Equation 2.13) of electrons by neutrinos, the reaction is highly directional and confirms that the Sun is the source of neutrinos. SNO's measured elastic scattering flux is [32, 33, 34, 35]:

$$R_{exp,ES} = 2.21_{-0.26}^{+0.31}(\text{statistical}) \pm 0.10(\text{systematic}) \times 10^6 \text{ cm}^{-2}\text{s}^{-1} \quad (2.16)$$

In the charged current reaction (Equation 2.14), the electron neutrinos are absorbed on deuterons producing an electron of energy closely related to that of the neutrino. The charge current has a flux for electron neutrinos of [32, 33, 34, 35]:

$$R_{exp,CC} = 1.59_{-0.07}^{+0.08}(\text{statistical})_{-0.08}^{+0.06}(\text{systematic}) \times 10^6 \text{ cm}^{-2}\text{s}^{-1} \quad (2.17)$$

In the second phase of the SNO experiment, NaCl was added to the heavy water to increase the efficiency of the neutral current interaction. All the neutrino flavours were measured using the neutral current reaction and for the neutral current phase the flux was found to be [32, 34, 35]:

$$R_{exp,NC} = 5.21 \pm 0.27(\text{statistical}) \pm 0.38(\text{systematic}) \times 10^6 \text{ cm}^{-2}\text{s}^{-1} \quad (2.18)$$

The total neutrino flux measured by SNO can be determined from these three different measurements and compared to standard model calculated value [4, 5]:

$$R_{SSM} = 5.69(1.00 \pm 0.16) \times 10^6 \text{cm}^{-2}\text{s}^{-1} \quad (2.19)$$

The excellent agreement of the standard solar model calculations with the measurement made by the SNO experiment gives strong evidence that neutrinos undergo a “flavour change” on the journey from the Sun to Earth. Meaning that it was possible neutrinos that started in the Sun as electron flavour neutrinos changed flavour to tau or muon type neutrinos.

### 2.2.3 Liquid Scintillator Experiments

The next round of experiments explore using an organic liquid scintillator as the target material, the two forerunners at this are BOREXINO and KamLAND. BOREXINO is a low background, large mass, real-time detector for solar neutrinos. It is a transparent nylon vessel of 8.5 m in diameter and surrounded by 2200 photomultiplier tubes located on a stainless steel sphere of 13.7 m in diameter. The detector is located in an underground facility (3500 m water equivalent) at Laboratori Nazionali del Gran Sasso in Italy. The main goal is the detection of 0.862 MeV  ${}^7\text{Be}$  solar neutrinos through the scattering interaction [36, 37]:

$$\nu_x + e^- \rightarrow \nu_x + e^- \quad (2.20)$$

The BOREXINO active medium consists of 300 tonnes of a liquid scintillator cocktail comprised of ultrapure pseudocumene and PPO(2,5 diphenyloxazole). The energy threshold is 250 keV, which allows the detection of the 0.862 MeV monoenergetic  ${}^7\text{Be}$  neutrinos, producing a continuum recoil spectrum (maximum energy of 0.66 MeV) in the detector [36, 38, 37, 39].

In 1994, before BOREXINO began with the main detector, a prototype was deployed to get a better understanding of the backgrounds and purity goals required to operate at such a low energy threshold; it was called the Counting Test Facility (CTF). The CTF is 4.3 tonnes of the liquid scintillator surrounded by 1000 tonnes of high purity water shield and viewed by 100 photomultiplier tubes. The results of the CTF indicated that the desired high radiopurity levels could be reached and led to the design finalization and construction of BOREXINO beginning at the end of 1996. For results and more information see [40, 41, 42].

BOREXINO has recently published the first results of the direct measurement of the  ${}^7\text{Be}$  solar neutrino signal rate [43]:

$$R_{\text{BOREXINO}} = 47 \pm 7(\text{statistical}) \pm 12(\text{systematic}) \text{ counts}/(\text{day} \cdot 100 \text{ tons}) \quad (2.21)$$

This is in perfect agreement with the rate averaged over the earth orbit (to account for change in flux) based on solar models and neutrino oscillations:

$$R_{\text{SSM}} = 49 \pm 4 \text{ counts}/(\text{day} \cdot 100 \text{ ton}) \quad (2.22)$$

These results are from 47.4 live days of data taking between May and July 2007.

Another liquid scintillator experiment is KamLAND (Kamioka Liquid Scintillator Antineutrino Detector) which is designed to study low energy neutrinos and antineutrinos. The detector is in the cavity originally used for KamiokaNDE. Since data taking began in 2002, KamLAND has had excellent success in the observation of the oscillation of reactor antineutrinos. The anti-neutrino events recorded in KamLAND originated from 53 power reactor units in Japan. KamLAND contains 1000 tons of liquid scintillator (80% dodecane, 20% pseudocumene, and PPO) and is surrounded by 1900 photomultiplier tubes [44]. The antineutrinos interact with the protons in the scintillator by the inverse beta decay (Equation 2.23).

$$\bar{\nu}_e + p \rightarrow n + e^+ \quad (2.23)$$

This reaction has a threshold of 1.8 MeV. After the inverse beta decay the positron almost immediately annihilates with an electron, the neutron is thermalized and about 200  $\mu\text{s}$  later is captured by another proton, releasing a 2.2 MeV gamma. The coincidence of this gamma and the  $e^+$  energy provide a powerful signal discriminant. KamLAND experiment is a disappearance experiment, as it measures the deficit of electron type antineutrinos from the calculated flux of antineutrinos from the surrounding nuclear detectors [45]. After 145.1 days of exposure, the ratio of the number of observed events to the expected number without disappearance events is:

$$\frac{N_{obs} - N_{BG}}{N_{exp}} = 0.611 \pm 0.85(\text{statistical}) \pm 0.041(\text{systematic}) \quad (2.24)$$

where  $N_{obs}$  is the number of observed events,  $N_{BG}$  is the number of background events and  $N_{exp}$  is the number of expected events if the disappearance did not occur. The expected  $\bar{\nu}_e$  flux is inconsistent with the observed number of events at the 99.95% confidence level [46].

Beyond reactor neutrino measurements, another area that KamLAND has made the first measurements is in the field of geoneutrinos. Geoneutrinos are the antineutrinos produced by the decay of  $^{238}\text{U}$  and  $^{232}\text{Th}$  from the interior of the Earth. The Earth has a radiogenic core, but the exact source of the radiogenic power is not known accurately and the KamLAND measurement gives an upper limit on the geoneutrino contribution. The interaction measured is the same as that used in the reactor neutrino measurement (Equation 2.23). This first measurement found  $25_{-18}^{+19}$  geoneutrino events, which gives an upper limit on the radiogenic power from  $^{238}\text{U}$  and  $^{232}\text{Th}$  decay in the Earth of 60 TW [47].

KamLAND is now in a re-purification stage to improve radiopurity in order that

${}^7\text{Be}$  solar neutrino measurements may be made. The liquid scintillator has been contaminated with mainly  ${}^{210}\text{Pb}$  due to radon exposure from the air; and the re-purification will reduce the impurity level by several orders of magnitude.

## 2.3 Neutrino Oscillations

The solar neutrino experiments over the past four decades have pieced together one of the greatest physics achievements of the last century. The phenomenon of the *missing solar neutrinos* was solved by the SNO experiment after measuring the neutrino flux from the Sun of all flavours of neutrinos and comparing it to the other experimental results which only measured the electron flavour neutrino flux. The explanation is the neutrinos change flavour on their way from the Sun to the Earth. The experiments that were only sensitive to electron type neutrinos saw less than the predicted flux for all neutrino flavours, whereas the experiment sensitive to all flavours (SNO) was able to measure the complete SSM predicted neutrino flux.

The mechanism by which neutrinos oscillate is somewhat of an open question in neutrino physics; there are a variety of theories that the available information and measurements support and not enough evidence to determine which model is correct. However, the model that is most widely accepted is the *Large Mixing Angle Mikheyev-Smirnov-Wolfenstein* (LMA MSW) model which is supported by solar [32], and reactor [48] neutrino experiments. One of the important predictions of the LMA MSW model is that the electron neutrino survival probability (the probability that an electron neutrino from the Sun will be detected as an electron neutrino on Earth) will increase at low energies.

The following is a mathematical description of the phenomenon of neutrino oscillations. There are three flavours of neutrinos as previously discussed. Each of the three flavours of neutrinos are denoted as a flavour eigenstate:  $|\nu_\alpha\rangle$  ( $\alpha = e, \mu, \tau$ ).

Each of these flavour eigenstates can be described as a superposition of mass eigenstates usually labeled as  $|\nu_k\rangle$  ( $k = 1, 2, 3$  to denote  $m_1, m_2, m_3$ ) corresponding to three neutrino masses (Equation 2.25).

$$|\nu_\alpha\rangle = \sum_k U_{\alpha k} |\nu_k\rangle \quad (2.25)$$

The neutrino mass states  $|\nu_i\rangle$  are eigenstates of the Hamiltonian:  $\mathcal{H}|\nu_k\rangle = E_k|\nu_k\rangle$ , where  $E_k = \sqrt{p^2 + m^2}$  are the energy eigenvalues. The time evolution for a general neutrino state,  $|\nu(t)\rangle$  is given by the Schrödinger equation and implies that the mass neutrino states evolve in time as plane waves shown in Equation 2.26.

$$|\nu_k(t)\rangle = e^{-iE_k t} |\nu_k\rangle \quad (2.26)$$

If the neutrino masses are not identical, the mass eigenstates are different and a mixed neutrino mass eigenstate propagates with different phase for the different mass eigenstates. As a result, while the neutrino travels from the Sun to the Earth different combinations of the mass eigenstates can exist and change over the course of the neutrino's journey. When the neutrino reaches Earth, the observed flavour is determined by a mixture of the mass eigenstates. These two eigenstates,  $|\nu_\alpha\rangle$  and  $|\nu_k\rangle$  can be related by a  $3 \times 3$  unitary matrix as they make up the orthogonal basis for the general neutrino states.

This unitary matrix,  $U$ , is called the Pontecorvo-Maki-Nakagawa-Sakata (PMNS) after the physicists who first described it (Maki, Nakagawa and Sakata) matrix and the physicist who first proposed oscillations (Pontecorvo). This matrix is the lepton mixing matrix and it is analogous to the Cabibbo-Kobayashi-Maskawa matrix in the quark sector. Although there are three massive neutrinos, often when looking at neutrino oscillations a two-neutrino approximation is used in which only two of the three neutrinos are considered. The two-neutrino simplification can be used if two of

the neutrino masses are nearly the same. The result is one of the mass differences  $\Delta m^2 = m_i^2 - m_k^2$  ( $i, j = 1, 2, 3$ ) is much larger than the other two. This is useful because the oscillation formulas depend on fewer parameters and as a result are much more simple. Many experiments are not sensitive to the influence of three-neutrino mixing, which means the data can be analyzed effectively by the two-neutrino model.

In two-neutrino mixing the two flavours considered are:  $\nu_\alpha$  and  $\nu_\beta$ . The possible situations are pure neutrino flavours such as  $\alpha, \beta = e, \mu$  or  $e, \tau$  or  $\mu, \tau$ ; or linear combinations of neutrino flavours such as in a neutrino disappearance experiment where  $\alpha = e$  and  $\beta = c_\mu \nu_\mu + c_\tau \nu_\tau$  and  $c_\tau^2 + c_\mu^2 = 1$ ; or experiments where an electron neutrino changes to a  $\mu$  or  $\tau$  type neutrino ( $\nu_e \rightarrow \nu_{\mu, \tau}$ ), but the final two flavours cannot be distinguished. In the two-neutrino case the mixing matrix can be written down in a very simple form as shown in Equation 2.27.

$$U = \begin{pmatrix} \cos \theta & \sin \theta \\ -\sin \theta & \cos \theta \end{pmatrix} \quad (2.27)$$

In Equation 2.27,  $\theta$  is the mixing angle in vacuum. Also in this two-neutrino case there is only one mass difference that is considered:  $\Delta m^2 \equiv \Delta m_{21} \equiv m_2^2 - m_1^2$ . The mixing matrix is used to express how the flavour and mass basis relate, shown explicitly in Equations 2.28 and 2.29:

$$|\nu_\alpha\rangle = \cos \theta |\nu_1\rangle + \sin \theta |\nu_2\rangle \quad (2.28)$$

$$|\nu_\beta\rangle = -\sin \theta |\nu_1\rangle + \cos \theta |\nu_2\rangle \quad (2.29)$$

The result of Equation 2.26 can be used with the mixing matrix (Equation 2.27) to describe how the flavour eigenstates evolve in time (Equation 2.30):

$$\begin{aligned}
|\nu_\alpha\rangle &= e^{-iE_1 t} \cos\theta |\nu_1\rangle + e^{-iE_2 t} \sin\theta |\nu_2\rangle \\
|\nu_\beta\rangle &= -e^{-iE_1 t} \sin\theta |\nu_1\rangle + e^{-iE_2 t} \cos\theta |\nu_2\rangle
\end{aligned}
\tag{2.30}$$

If the mass of the neutrino is assumed to be much smaller than its momentum, which the current limits suggest, the energies can be approximated as (Equation 2.31).

$$E_k \simeq E + \frac{m_k^2}{2E} \tag{2.31}$$

The two-neutrino case can be approximated further as the difference between the two energies, resulting in an expression dependent on  $\Delta m^2$  (Equation 2.32).

$$E_2 - E_1 \simeq \frac{\Delta m^2}{2E} \tag{2.32}$$

From equations 2.32 and 2.30 it is possible to develop an expression for the probability that a neutrino of one flavour, created at time 0, will be the same flavour when it arrives as time  $t$ ; this is also referred to as the survival probability and is shown for the two-neutrino case in Equation 2.33.

$$\begin{aligned}
P_{\nu_e \rightarrow \nu_e}(t, E) &= |\langle \nu_e(0) | \nu_e(t) \rangle|^2 \\
&= 1 - \sin^2 2\theta \sin^2 \left( \frac{\Delta m^2}{2E} t \right)
\end{aligned}
\tag{2.33}$$

In Equation 2.33, the time  $t$  can be approximated as  $L$ , the distance between the source and the detector. In neutrino experiments, the propagation time is not measured, but the distance  $L$  is a well-known distance, so this approximation is more useful and the survival probability in terms of  $L$  is stated in Equation 2.34.

$$\begin{aligned}
P_{\nu_e \rightarrow \nu_e}(L, E) &= |\langle \nu_e(0) | \nu_e(t) \rangle|^2 \\
&= 1 - \sin^2 2\theta \sin^2 \left( \frac{\Delta m^2}{2E} L \right)
\end{aligned} \tag{2.34}$$

The above situation is for vacuum oscillations, but there are also matter oscillations that occur when neutrinos travel through the Earth or Sun on the way to the detector. All flavour types can interact with the Z boson, but only the electron neutrino can interact with the  $W^\pm$  boson. The electron type neutrino has a larger cross section due to its ability to interact via both the charged current and neutral current interactions. This can significantly change its propagation, resulting in a different probability for flavour changing than in the vacuum. The Mikheyev-Smirnov-Wolfenstein (MSW) effect describes the flavour change that occurs in matter, describing neutrino mass and mixing and neutrino-matter interactions. The effective Hamiltonian for propagation through matter in the two-neutrino case is shown in Equation 2.35 [6].

$$\mathcal{H} = \begin{pmatrix} \frac{\Delta m^2 \cos 2\theta_{12}}{4E} - \frac{\sqrt{2}G_F n_e}{2} & \frac{\Delta m^2 \sin 2\theta_{12}}{2E} \\ \frac{\Delta m^2 \sin 2\theta_{12}}{2E} & -\frac{\Delta m^2 \cos 2\theta_{12}}{4E} + \frac{\sqrt{2}G_F n_e}{2} \end{pmatrix} \tag{2.35}$$

In Equation 2.35,  $\theta_{12}$  is the two-neutrino vacuum mixing angle,  $\Delta m^2$  the difference of the neutrino masses squared, and  $E$  is the neutrino energy. In Equation 2.35, the term  $\frac{\sqrt{2}G_F n_e}{2}$  is included in the diagonal terms to describe matter-induced effects. In this term  $G_F$  is the Fermi coupling constant and  $n_e$  is the electron density through which the neutrino propagates. The ratio of matter to vacuum effects is given by Equation 2.36, in which the factor  $\beta$  parameterizes the relative importance of the MSW matter term and the vacuum term in the Hamiltonian.

$$\beta = \frac{2\sqrt{2}G_F n_e E_\nu}{\Delta m^2} \quad (2.36)$$

The survival probability of the electron neutrino can be expressed by taking into account matter effects for the two neutrino mixing case in the large mixing angle (LMA) region [6, 9].

$$P_{\nu_e \rightarrow \nu_e} = \frac{1}{2} + \frac{1}{2} \cos 2\theta_{12}^M \cos 2\theta_{12} \quad (2.37)$$

where in Equation 2.37,  $\theta_{12}^M$  is the mixing angle in matter and it can be expanded to be [6, 9]:

$$\cos 2\theta_{12}^M = \frac{\cos 2\theta_{12} - \beta}{\sqrt{(\cos 2\theta_{12} - \beta)^2 + \sin^2 2\theta_{12}}} \quad (2.38)$$

The  $\beta$  is calculated at the location where the neutrino is produced, so in the case of solar neutrinos, through the decreasing electron density as the neutrino propagates out of the Sun. The evolution of the neutrino is adiabatic, that is the change in density experienced by the neutrino on its journey is slow enough such that the parameters in the Hamiltonian vary slowly enough that the neutrino follows the changing Hamiltonian eigenstate [9, 6]. The survival probability thus depends on the initial and final density but not on transition density details.

The LMA survival probability has two distinct regions; matter-dominated oscillations and vacuum dominated oscillations. For  $\beta < \cos 2\theta_{12}$  the survival probability is dominated by vacuum (averaged) oscillations (Equation 2.39). For  $\beta > 1$ , the LMA survival probability corresponds to matter-dominated oscillations, referred to as the MSW effect (Equation 2.39).

$$\begin{aligned} P_{\nu_e \rightarrow \nu_e} &= 1 - \frac{1}{2} \sin^2 2\theta_{12} && (\beta < \cos 2\theta_{12}, \text{ vacuum}) \\ P_{\nu_e \rightarrow \nu_e} &= \sin^2 2\theta_{12} && (\beta > 1, \text{ MSW}) \end{aligned} \quad (2.39)$$

The neutrino survival probability is approximately constant at the two extremes ( $\beta < \cos 2\theta_{12}$  and  $\beta > 1$ ), however there are many unknown factors about what occurs at the transition between the two. The exact energy the transition occurs at is unknown and in general depends on the detailed behavior of neutrino oscillations. The factors that affect this behavior include the neutrino source be that  ${}^8\text{B}$ ,  $pp$ ,  ${}^7\text{Be}$ , or any other type of neutrino produced in the Sun and on the  $\Delta m^2$ . Current solar models [6] put the transition around 2 MeV for most neutrino sources. To probe the transition region experimentally and achieve experimental values to compare to the solar models, neutrino experiments in the 2 MeV regime should be performed.

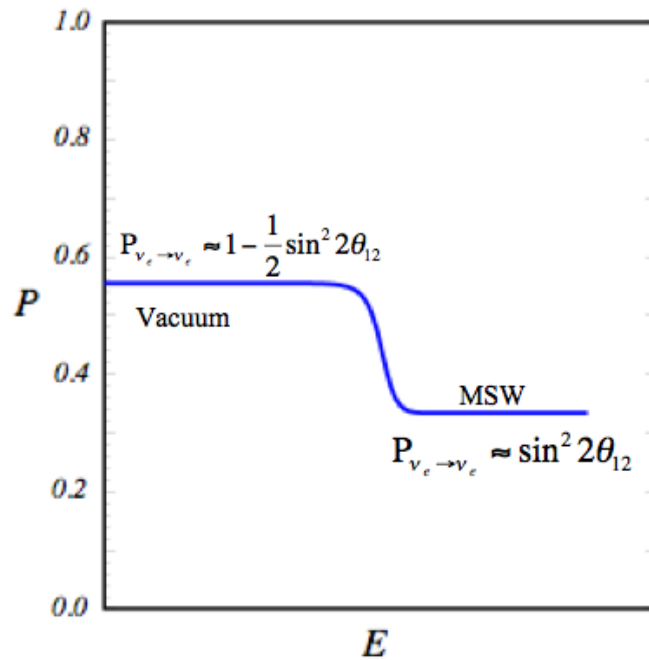


Figure 2.4: Electron neutrino survival probability as a function of energy for LMA oscillation solution. For small values of  $E$ , and in turn small  $\beta$  vacuum effects are dominant, and for large values of  $E$  and  $\beta > 1$  MSW matter oscillations are dominant. For solar neutrinos this transition occurs around 2 MeV. Adapted from [6, 9].

# Chapter 3

## SNO+ Introduction

SNO+ is the next generation of the Sudbury Neutrino Observatory (SNO) project, the name stands for SNO plus scintillator. The project will exist in two phases: solar neutrino phase and a neutrinoless double beta decay phase. Although originally the solar neutrino phase was going to head off the project, growing excitement about the double beta decay possibilities in the neutrino physics world have pushed this phase to the forefront of the project. It is important to note that although the currently double beta decay is a big topic in particle physics, the solar results will prove to be invaluable in improving the overall understanding of the Sun and in probing the details of neutrino oscillations.

### 3.1 Transition from SNO

November 28, 2006 marked the end of the data acquisition with heavy water for the Sudbury Neutrino Observatory, and it also marked the beginning of the transition phase from SNO to SNO+. The heavy water was drained out and the intermediate tasks have begun. One of the major advantages of the SNO+ project is that it will be able to take over the majority of the existing infrastructure already in place from SNO. This will not only save research dollars, but also save time on research and

development. SNO+ will be able to use much of the existing electronics, the acrylic vessel, the photomultiplier tubes (PMT) and PMT support structure (PSUP).

There are still some engineering problems that will have to be solved before the complete installation of the project, not the least of which is the change of buoyancy from the SNO set up. In SNO, the heavy water in the acrylic vessel was heavier than the light water it was suspended in so there were ropes designed to hold the acrylic vessel up. In SNO+ the acrylic vessel will be filled with the liquid scintillator which is lighter than the water surrounding it so a system to hold down the acrylic vessel will have to be engineered [49].

There are other intermediate tasks which need to be addressed, such as inspecting the acrylic vessel and determine whether or not any major structural changes were incurred during the running of SNO. One of the major concerns is the plating out (implanting) of  $^{222}\text{Rn}$  daughters on the acrylic vessel [50]. This can occur during the decay process when the daughters are implanted into the acrylic surface by the recoil force from the  $\alpha$  decays. The rate around the neck of the SNO detector has been measured as  $1.8 \pm 0.5$  decays/cm<sup>2</sup>/day below the D<sub>2</sub>O level and  $9.2 \pm 0.9$  decays/cm<sup>2</sup>/day above the D<sub>2</sub>O level [50]. Due to the very large surface area of the acrylic vessel this background rate could have a large effect on SNO+ measurements.

These implanted alphas were not a major concern for the SNO project; however, with SNO+ operating at lower energies these alphas will have to be considered and probably removed. In documents put out by the SNO+ group [50, 51, 52], much discussion on this topic and possible solutions have been addressed. The different possible ways for removing the radon daughters have been investigated, include washing with distilled water, washing with Alconox detergent and sanding [50]. The method that proved to be most effective in removing all of the daughters was sanding. The results show that sanding achieves better than 99.96% efficiency at 90% confidence [50, 52]. There are still many details to work out about how to implement the sanding

of the acrylic vessel, including doing the work in a radon-free environment to limit additional radon exposure. The sanding should be done wet so that dust does not resettle and further contaminate surfaces. It is estimated that it will take three people forty-five days to sand the entire acrylic vessel at a rate of  $10 \text{ m}^2/\text{shift}$ .

Other issues that will have to be considered are the use and processing of the liquid scintillator underground and clearing all safety regulations with INCO, the mine owners. As well an elaborate purification system for the liquid scintillator, potentially underground, will have to be designed and implemented. The scintillator will be discussed in Section 3.3.

## 3.2 The Science and Motivation

The addition of liquid scintillator to the SNO detector will allow for the study of many interesting areas of low energy neutrino physics. Lower energy solar neutrinos such as pep and CNO neutrinos are of particular interest. In addition to solar neutrinos, antineutrinos from nuclear reactors and geoneutrinos from the radioactive decays in the Earth's crust and mantle can also be studied. The other stage of SNO+ will be a neutrino-less double beta decay experiment, where an isotope, such as neodymium, will be added to the scintillator to provide a large number of potentially decaying nuclei.

Solar neutrino experiments at low energies can reveal new phenomena that were undetectable at higher energies, such as the transition from matter-induced oscillations to vacuum oscillations, the possibility to make a precise measurement of the vacuum mixing angle and a measurement of the  $\Delta m^2$  parameter. In addition, accurate measurements of neutrino fluxes will be made to test the solar models [6].

### 3.2.1 CNO and *pep* Neutrinos

As reviewed in Section 2.1, *pep* and CNO neutrinos are both part of the low energy solar neutrino spectrum. A measurement of the *pep*  $\nu - e$  scattering rate would give essentially the same information about solar neutrino fluxes and solar models as the same measurement for *pp* neutrinos [6]. So a measurement of the *pep* neutrino flux would improve knowledge about the solar neutrino luminosity. This information would make it possible to make a comparison between the photon luminosity and the solar neutrino luminosity could be interesting because it takes photons  $10^5 - 10^6$  years to diffuse out of the Sun and neutrinos only a few seconds. Another benefit of making a measurement of the *pep* neutrino flux is its low theoretical uncertainty ( $\pm 1.5\%$ ) from calculations of the standard model. For this reason, a *pep* measurement is an excellent way to test the standard solar model.

The CNO flux has never been experimentally measured and currently has very large uncertainties in the solar standard model. Any measurement of the CNO reaction would greatly improve understanding of solar models and the solar interior. A CNO measurement would greatly contribute to solar physics. In recent years there has been some discrepancy between predicted results from solar model calculations and helioseismology measurements, particularly pertaining to element abundances of carbon, nitrogen, oxygen, argon, and neon [53, 4, 54, 55]. Although currently the p-p chain reactions are thought to be responsible for almost 98.5% of the Sun's energy, a CNO measurement would improve understanding on element abundance and would result in further constraints to the solar model calculations [56].

### 3.2.2 Survival Probability

One more important measurement that can be made by SNO+ is the electron neutrino survival probability, which is the probability that an electron neutrino produced in the center of the sun is detected as an electron type neutrino on Earth. Recall from

Section 2.3 that the transition between vacuum and matter oscillations has never been measured at these neutrino energies. The *pep* is the perfect neutrino flux candidate to make this measurement because its energy is well defined by the SSM and it is located in the area of interest on the survival probability plot (Figure 3.1). This measurement would definitely open the door to “new physics.”

The low uncertainty on the *pep* flux in the standard solar model makes it a prime contender to investigate the matter-vacuum transition region for solar neutrino oscillations [57, 58]. In the low energy region between 1-3 MeV, according to the MSW-LMA oscillation solution, the transition between matter dominated and vacuum dominated oscillations is predicted to occur [59]. Previous neutrino experiments have been unable to probe the vacuum-matter transition region because they are not sensitive to neutrino energies in this range.

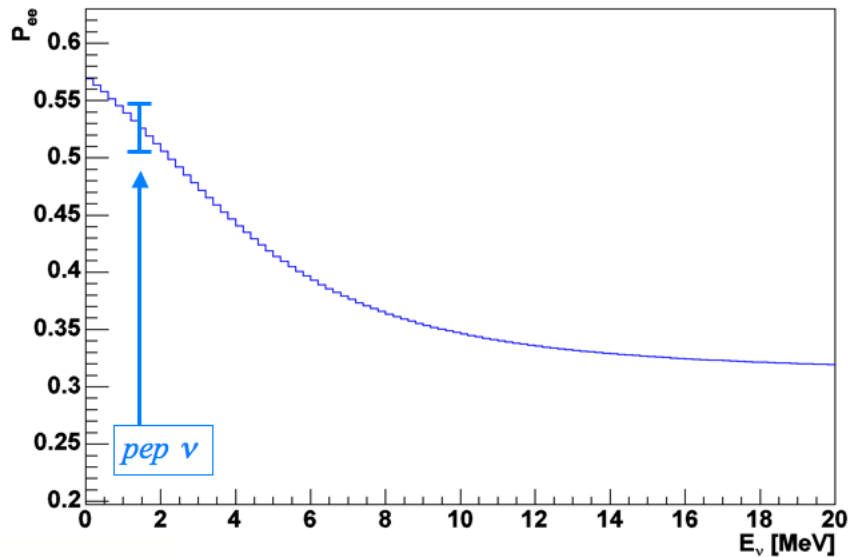


Figure 3.1: Electron neutrino survival probability plot adapted from [6]. The bar represents the energy a *pep* neutrino measurement would be made at and the error bar is an estimation from the current standard solar model, statistical and systematic uncertainties.

### 3.2.3 Neutrinoless Double Beta Decay

Neutrinoless double beta decay is currently a topic of great interest in particle physics, and SNO+ will be able to make an interesting contribution to this search. A measurement of neutrinoless double beta decay would allow for an absolute neutrino mass measurement to be made. A positive neutrinoless double beta decay signal would confirm that neutrinos are Majorana particles (particle that is its own antiparticle) which could have an impact on cosmology. SNO+ will add a double beta decay substance to the liquid scintillator; the material currently under development to be used is  $^{150}\text{Nd}$ . This material is a good candidate because of its large Q-value (3.37 MeV) and large nuclear matrix element. However, there is still some uncertainty in the calculation as the  $^{150}\text{Nd}$  nuclei is quite deformed and all calculations are done for spherical nuclei. Large Q-values and nuclear matrix elements are desirable for the target nuclei, so it is important that these calculations be as accurate as possible to confirm that it has the required qualities. If SNO+ was loaded with neodymium, then a 0.1% loading would correspond to 1000 kg of natural neodymium which is 56 kg of pure  $^{150}\text{Nd}$  [60]. There is the possibility that the collaboration will be able to acquire enriched  $^{150}\text{Nd}$  from the MENPHIS facility in France. It uses the Atomic Vapour Laser Isotope Separation (AVLIS) technique and has in the past enriched 200 kg of uranium in 2 weeks. If the facility could be used it would allow a much larger sample of  $^{150}\text{Nd}$  (compared to natural) to be used. The optical properties constrain the total mass of Nd that can be used. Enriching would allow a larger target mass to be used while maintaining necessary optical qualities. This would lead SNO+ to have a much more sensitive experiment for neutrino masses [60] than if it used natural neodymium.

### 3.2.4 Geo-neutrinos

Geo-neutrinos are antineutrinos produced in the nuclear decay of  $^{232}\text{Th}$ ,  $^{238}\text{U}$ , and  $^{40}\text{K}$ . The measurement of geo-neutrinos can constrain the amount of energy released

from the nuclear decays in the Earth. The current constraints are that radioactivity accounts for 40% to 100% of Earth's total heat flow [61] so a measurement would be helpful to geophysicists. A measurement can help to study the processes inside the Earth and make a direct measurement of the total amount of uranium and thorium in the Earth's crust and mantle. A direct measurement will provide much needed data for geophysical and geochemical models of the Earth and the Earth's thermal history [62].

KamLAND made the first geo-neutrino measurement [47], but the measurement was not precise enough to set useful limits on the radiogenic heat flux in the Earth. SNO+ will be able to make a more precise measurement because it has a much lower reactor neutrino background than KamLAND and the surrounding geology, the Canadian Shield, is very well known which makes interpreting the measurement easier and lowers the uncertainty on the measurement. SNO+ should have a higher signal rate and expects to see 49 geo-neutrino events/ $10^{32}$ proton-years on a background of 44 reactor events/ $10^{32}$ proton-years [63]. SNO+ will be able to make a geo-neutrino measurement without altering the detector.

### 3.3 The Liquid Scintillator

There are many liquid scintillators available for use in large scale projects. A liquid scintillator is any liquid that produces light when a charged particle passes through it. Organic scintillators usually contain a benzene ring. For SNO+ the characteristics of the liquid scintillator that are important are:

1. A high light yield, which means absorbed energy is efficiently converted to light output
2. An emission spectrum that overlaps with the response of the PMTs that will be used in SNO+

3. A high flash point (lowest temperature at which a flammable liquid can form a ignitable mixture in air) and low toxicity for safety
4. High transparency to enable the light signal to efficiently reach the PMTs
5. Compatibility with materials it will be in contact with, such as acrylic
6. Low cost as many tons will be used.
7. Able to be purified

### 3.3.1 Linear Alkylbenzene

The organic liquid scintillator that SNO+ has decided to use is Linear Alkyl Benzene (LAB). All the above mentioned criteria are met with LAB: it has a high flash point at 130°C and has low toxicity. LAB is the precursor to linear alkylbenzene sulfonate which is a key ingredient in many household and industrial detergents, and has been industrially produced since the 1950s. Conveniently there is a plant in Quebec, Petresa Canada, that produces high purity LAB (approximately 120 kton/year), which means that the LAB will be able to be obtained at a relatively low price without extravagant shipping costs. Its purity is high directly from the manufacturer and has demonstrated without any purification to have a light attenuation length of 20 m at 420 nm.

The Petresa Canada company describes how LAB is made in Reference [64]. The process begins with paraffin, a common group of alkane hydrocarbons having the chemical formula  $C_nH_{2n+2}$ . Paraffin molecules come in different carbon string lengths from methane,  $CH_4$ , which is the simplest form to much larger structures with over forty carbons. The first step at the Petresa plant is to take the raw paraffin and transform it into olefin by the process of dehydrogenation. Olefins have one or more unsaturated hydrocarbon: they contain at least one carbon-carbon double bond.

The simplest form, with only one double bond has the general formula  $C_nH_{2n}$ . The dehydrogenation takes place in a vapour phase reaction over a highly selective and active catalyst. Next, there are two purification processes to treat the olefins; this is important to SNO+ and can perhaps be altered or the number of purification steps increased to ensure the highest purity possible. In the next step, the olefins and benzene react and combine to form linear alkylbenzene. The LAB is then distilled to collect, remove, and reuse the leftover paraffin and benzene. The final stage involves a final purification where the heaviest chains are removed from the LAB sample and are used in other commercial areas. The LAB that SNO+ will receive from Petresa Canada will contain linear alkyl benzene molecules with different length of alkyl chains. The chains will vary in length between ten to sixteen carbons in the alkyl chain.

Even with purification steps completed by the company during the fabrication of LAB, other purification needs to be done in order to reach the required low background levels. There are many inherent backgrounds that will require purification to remove so as not to interfere with the signals and there are also optical purification goals that need to be achieved. The purification goals will be discussed in Chapters 4 and 5.

### 3.4 Neutrino Signal in SNO+

The neutrino signal in SNO+ will be detected through the neutrino-elastic scattering interaction:

$$\nu_x + e^- \rightarrow \nu_x + e^- \quad (3.1)$$

Although elastic scattering is able to detect all flavours of neutrinos, this interaction is most sensitive to electron flavour neutrinos. In elastic scattering, the kinetic energy of the scattered electron can be any energy up to the kinematic maximum energy

following the collision of the neutrino. Due to this range of energies, the differential scattering cross section must be known in detail in order to extract the neutrino energy spectrum from the recoil electron energy spectrum. In SNO+, scintillation light is produced by recoil electrons, the target electrons are those in the liquid scintillator molecules. This isotropic scintillation light is detected by the PMTs. By counting the PMT charge and the total number of hits the energy of the recoil electron can be found. The electron recoil spectrum in SNO+ has been simulated using a standalone code that generates data sets using energy shapes that have been calculated using SNOMAN (the code from the SNO experiment which includes information about the SNO geometry) for both signals and backgrounds. The signals and backgrounds are smeared using a gaussian energy resolution and then the data are fit using the original shapes. Figure 3.2 shows the simulated spectrum; the key feature is the *pep* signal, which exists in the spectrum between 1 MeV and 1.3 MeV [49]. As well there is a slight upturn around 0.7 MeV that is a result of the predicted CNO signal.

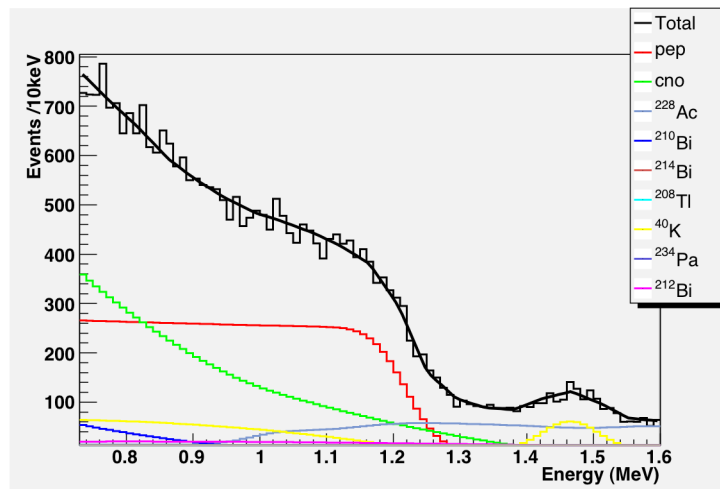


Figure 3.2: Low energy solar neutrino recoil electron spectrum in SNO+.

## 3.5 The Backgrounds in SNO+

In SNO+, as in most neutrino experiments, a quality physics measurement can only be made if the backgrounds are well understood and minimized. This is especially important in a scintillator experiment that deals with low energy events in an extremely energy sensitive medium such as organic liquid scintillator. Scintillators detect events from charged particles depositing energy as they pass through the medium. Ideally this would be the neutrino signal, but other particles can deposit energy in the scintillator as well. Some of these classes of backgrounds have energy spectra that match the energy spectrum of the physics of interest so closely that it is imperative that they are understood and constrained as well as possible, and/or removed by purification.

There are two categories that the background events can be divided into: internal and external backgrounds. Internal backgrounds are those that originate inside the detector and are a result of radioactive contamination from materials in the detector. External backgrounds are those that are produced outside the detector, but subsequently propagate into the detector [65].

### 3.5.1 Internal Backgrounds

The internal backgrounds are those which originate inside the detector, from the impurities in the liquid scintillator and from materials used to build the detector. It is fortunate for SNO+ that the preceding project, SNO, took much care in making sure everything was built from materials with the lowest radioactive impurities available. If SNO had not used such low radioactive materials it would make using the existing infrastructure much more difficult for SNO+.

There are still many precautions that are necessary as the transition phase continues. There are a few groups of contaminants that are particularly dangerous to SNO+. These are listed in Table 3.1 and represent individual or groups of isotopes

that must be kept out of the vicinity of the detector. To get an idea of the purity levels required, the amount of each isotope that is targeted in the KamLAND experiment is also listed.

One of the main contaminants for SNO+ is radon, in particular  $^{222}\text{Rn}$  which is a product of the  $^{238}\text{U}$  decay chain (Figure 3.3(a)). Radon is naturally occurring in air, and in elevated levels in the mine air, so it is quite difficult to keep the detector and its surroundings free from contamination. It is not only the  $^{222}\text{Rn}$  which poses a risk to the experiment; radon daughters,  $^{210}\text{Bi}$ ,  $^{210}\text{Pb}$  and  $^{210}\text{Po}$  can also cause a problem. Looking at Table 3.2, it can be seen that KamLAND's detector has been exposed to a considerable amount of radon and now has elevated levels of  $^{210}\text{Bi}$ ,  $^{210}\text{Pb}$  and  $^{210}\text{Po}$ . With re-purification they aim to bring the level down and if SNO+ is careful with radon exposure, levels even lower than KamLAND's re-purification value should be achievable (Table 3.1).

Isotope	Concentration (g/g)
$^{238}\text{U}$ Chain	$3.5 \times 10^{-18}$ [46]
$^{232}\text{Th}$ Chain	$1.4 \times 10^{-17}$ [46]
$^{40}\text{K}$	$3 \times 10^{-18}$ [66]
$^{39}\text{Ar}$	$2.03 \times 10^{-19}$ [66]
$^{85}\text{Kr}$	$4.1 \times 10^{-20}$ [66]
$^{210}\text{Bi}$ and $^{210}\text{Po}$	$5 \times 10^{-25}$ [66]

Table 3.1: KamLAND's repurification goals to remove radioisotopes

As mentioned previously, another problem that stems from air exposure is radon and radon daughters. Since SNO was not as sensitive to the radon as SNO+ will be, it was not a necessity to use exclusively radon-free air. Due to the radon exposure during the construction of the acrylic vessel, the radon daughters have attached to the inside of the acrylic vessel and could pose a serious problem to the SNO+ experiment. Radon levels naturally occur at about  $20 \text{ Bq/m}^3$  in normal air and  $40 - 100 \text{ Bq/m}^3$  in underground air, which means it is very important that the detector not be exposed

Isotope	Energy Endpoint	Decay	No. Events (Optimal)	No. Events (Current)
Uranium Chain				
$^{238}\text{U}^*$	$\sim 220$ keV	$\beta$	393	1572
$^{234}\text{Th}^*$	109 keV	$\beta$	393	1572
$^{234}\text{Pa}$	2290 keV	$\beta$	393	1572
$^{234}\text{U}$	$\sim 240$ keV	$\alpha$	393	1572
$^{230}\text{Th}$	$\sim 235$ keV	$\alpha$	393	1572
$^{226}\text{Ra}$	$\sim 235$ keV	$\alpha$	393	1572
$^{222}\text{Rn}$	$\sim 275$ keV	$\alpha$	393	1572
$^{218}\text{Po}$	$\sim 300$ keV	$\alpha$	393	1572
$^{214}\text{Pb}$	720 keV	$\beta$	393	1572
$^{214}\text{Bi}$	1510 keV	$\beta$	393	1572
$^{210}\text{Tl}$	4389 keV	$\beta$	393	1572
$^{214}\text{Po}$	$\sim 2385$ keV	$\alpha$	393	1572
$^{210}\text{Pb}^*$	150 keV	$\beta$	$393 + 4.4 \times 10^4$	$1572 + 8.9 \times 10^8$
$^{210}\text{Bi}$	1170 keV	$\beta$	$393 + 4.4 \times 10^4$	$1572 + 8.9 \times 10^8$
$^{210}\text{Po}$	$\sim 265$ keV	$\alpha$	$393 + 4.4 \times 10^4$	$1572 + 8.9 \times 10^8$
** From $^{210}\text{Pb}$ not in equilibrium				
Thorium Chain				
$^{232}\text{Th}^*$	$\sim 200$ keV	$\alpha$	1232	7390
$^{228}\text{Ra}^*$	53 keV	$\beta$	1232	7390
$^{228}\text{Ac}$	1100 keV	$\beta$	1232	7390
$^{228}\text{Th}$	$\sim 270$ keV	$\alpha$	1232	7390
$^{224}\text{Ra}$	$\sim 285$ keV	$\alpha$	1232	7390
$^{220}\text{Rn}$	$\sim 315$ keV	$\alpha$	1232	7390
$^{216}\text{Po}$	$\sim 340$ keV	$\alpha$	1232	7390
$^{212}\text{Pb}$	330 keV	$\alpha$	1232	7390
$^{212}\text{Bi}$	2250 keV	$\beta$ (36%)	1232	7390
	302 keV	$\alpha$ (64%)	1232	7390
$^{212}\text{Po}$	$\sim 440$ keV	$\alpha$	788	4730
$^{208}\text{Tl}$	1800 keV	$\beta$	444	2660
Potassium and Noble Gases				
$^{40}\text{K}$	1504 keV	$\beta$	$8.1 \times 10^4$	$2.2 \times 10^6$
$^{85}\text{Kr}$	687 keV	$\beta$	$1.7 \times 10^{10}$	$3.7 \times 10^4$
$^{39}\text{Ar}$	565 keV	$\beta$	$\sim 10^3$	$7.4 \times 10^9$

Table 3.2: Table of known internal backgrounds that affect SNO+. The values are based on KamLAND's current values and their optimal values after repurification.

to surrounding air unnecessarily and that a cover gas with a low radon content is used to prevent radon contamination.

Another concern for the SNO+ experiment is  $^{40}\text{K}$ , and like radon SNO+ is more sensitive to potassium contamination than SNO was. Like  $^{238}\text{U}$  and  $^{232}\text{Th}$ ,  $^{40}\text{K}$  is a naturally occurring radioactive isotope of natural potassium, making up only 0.012% of all potassium with a half-life of  $1.3 \times 10^9$  year. One of the main sources of potassium is mine dust and materials used in construction. SNO+ will use low potassium materials and replace existing materials, such as ropes, that contain higher than acceptable levels of potassium.

Radioactive argon and krypton are the last of the internal backgrounds. They occur in the air naturally. Exposing the liquid scintillator to air is one way this background could be introduced. If significant care is used while filling the detector it is possible to minimize the air exposure and nitrogen stripping can also be used to remove residual radioactive gas contaminants.

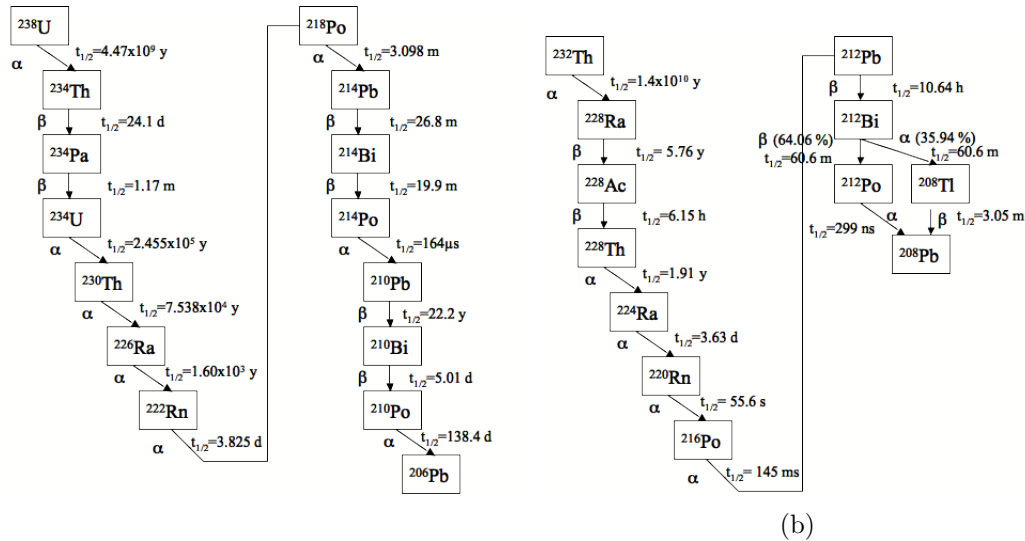


Figure 3.3: (a) Uranium chain (b) Thorium chain.

Cosmogenic activity is another background that can affect the SNO+ detector. Cosmogenic activity occurs when high-energy cosmic rays hit the Earth's atmosphere and produce muons which then pass through matter. As the muons are passing

through the Earth they occasionally interact with surrounding nuclei and produce *spallation products*. Most of these spallation products have a short half-life so they decay or are absorbed and do not pose a problem to the detector as they can be easily vetoed in software by ignoring events that happen a few seconds after the muon is observed. However, some spallation products have longer half-lives that cannot be easily vetoed and can remain in the detector [67].

One of the most common cosmogenic nuclides produced as a by-product of muon-induced cascades for many underground laboratories with organic targets ( $^{12}\text{C}$  and  $^1\text{H}$ ) is  $^{11}\text{C}$ . In SNOLAB, SNO+ is deep enough that, unlike BOREXINO and KamLAND, it will be able to observe pep and CNO neutrinos without significant  $^{11}\text{C}$  data cuts [57]. Both BOREXINO and KamLAND have significant  $^{11}\text{C}$  backgrounds which will impede their detection of *pep* and CNO neutrino signals [68].

### 3.5.2 External Backgrounds

External backgrounds are those that undergo a reaction outside the detector, but ultimately their products end up inside the detector. Examples of possible sources of external backgrounds are the wall underground near the detector, the ropes used to hold down the acrylic vessel, possible events from the acrylic vessel itself, the PMTs and events from the light water shield. Usually external backgrounds show up inside the detector as neutron or gamma events. Table 3.3 shows the expected levels of external backgrounds [69].

The light water shield (7000 tonnes) was designed to protect the detector from the activity of the cavity walls. Even though extreme care was taken in choosing materials for the detector components surrounding the acrylic vessel, the PMTs and the structure that supports them (the PSUP), it was not possible to rid them entirely of radioactivity. The shield easily stops lower energy gammas and neutrons from the surrounding rock. Another external background is neutrons caused by incoming muon

showers in the light water or heavy element spontaneous fission. The water shield is useful against neutrons since they readily capture on protons.

Source	Mass	Contaminant	Level
Ropes	210 kg	$^{232}\text{Th}$	178 ppt
		$^{238}\text{U}$	4 ppt
		natural K	1 ppm
Acrylic Vessel	30 tons	$^{232}\text{Th}$	1 ppt
		$^{238}\text{U}$	1 ppt
		natural K	1 ppb
$\text{H}_2\text{O}$	1555 tons	$^{232}\text{Th}$	0.052 ppt
		$^{238}\text{U}$	0.206 ppt

Table 3.3: Amount of external radioactivity in major components of SNO+ [69]

# Chapter 4

## Radiopurification Results and Analysis

As described in the previous Section 3, there are many sources of contamination that could cause backgrounds in SNO+. The presence of large backgrounds results in larger uncertainties in the signal leading to reduced precision in testing physics models. The removal of radioactive isotopes is called *radiopurification*, and there are a variety of different techniques that can be used to achieve high radiopurity. In this chapter, the focus of the radiopurification will be on the uranium and thorium chain isotopes as backgrounds in SNO+. In particular, the studies will focus on removing  $^{212}\text{Pb}$  as an analogy of  $^{210}\text{Pb}$  from the scintillator.

It is not known in what chemical state the lead impurities exist in the LAB. The state could be ionic, metallic, organic, or a combination of all three. Depending on the chemical state of the lead, there are different purification techniques that are used. Water extraction can be used if the lead is in ionic state, acid extraction is used if the lead is in an ionic or metallic state, and either adsorption or vacuum distillation can be used if the lead is in ionic, metallic or organic state. The latter two methods can remove all species of lead, however the first two can be implemented more simply and

less expensively so it is necessary to do a complete study to determine which method is most appropriate for purification. It is well documented in the literature that “it is very difficult to derive conclusive answers on the bonding and structure of lead ion complexes” [70].

In order to study the purification of the liquid scintillator a small scale test has been set up. The levels of impurities in raw LAB are too low to be measured by any lab equipment and can only really be measured in a low background large scale experiment like SNO+. In order to study the impurities, in this case  $^{212}\text{Pb}$ , a larger amount of the isotope must be added to the LAB. The elevated levels can then be used to test different purification methods in order to determine the best method of removing it. For each test at least two samples are used: a feed sample and a permeated sample. The feed sample is a sample of the spiked LAB and it determines the activity level of the sample before purification and the permeated sample is a sample of the LAB taken after purification. Depending on the test, there may be more than one permeated sample taken.

## 4.1 Spike Setup

The process of increasing the level of desired isotope is referred to as *spiking*. The general method of spiking in these experiments uses a thorium source that can be used to add  $^{220}\text{Rn}$  to a sample.  $^{220}\text{Rn}$  has a short half-life (55.6 seconds) and it decays to  $^{212}\text{Pb}$  which is the desired isotope for spiking in these experiments. The general setup (Figure 4.1) that is used in these spike tests involves coating a small column of silica gel or a small filter with a liquid thorium source. The liquid thorium sticks to the surface of the material in the column or filter. The column or filter is then attached to plastic tubing that is connected to a small container holding the liquid to be spiked, usually LAB. Air is then passed through the spiked column surface and

radon (decay daughter of thorium) is bubbled into the liquid. After the spiking, the liquid is set aside to allow the radon to decay into lead and then the purification procedures can begin.

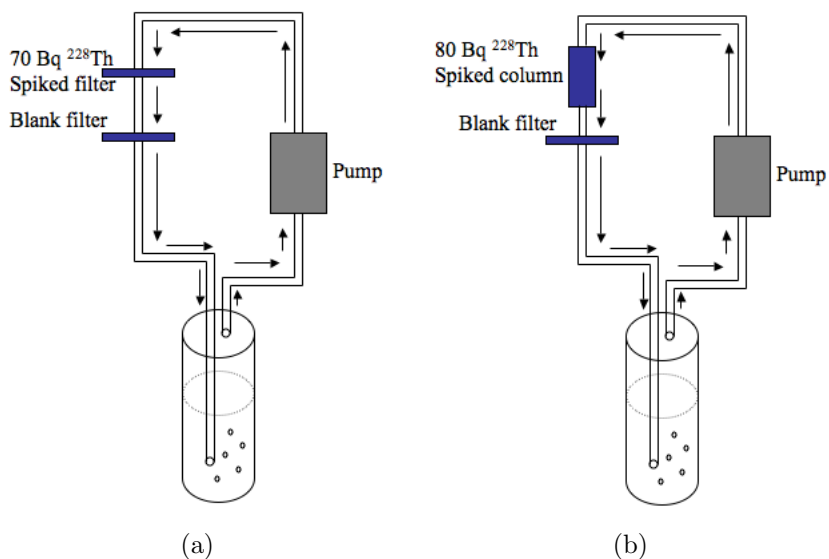


Figure 4.1: (a) Preliminary spike setup using a  $^{228}\text{Th}$  spiked filter. (b) Second spike setup using a  $^{228}\text{Th}$  column.

At the start of the preliminary testing process the spike setup, Figure 4.1(a), was very simple. A syringe filter was coated with liquid thorium-228 to make the spike. A peristaltic pump was connected to the spiked filter which was connected to a blank filter as a safety measure to prevent the solvent (LAB) from going backwards into the filter. The pump, spiked filter, and blank filter were all connected together with plastic tubing that connected to a small plastic container to hold the liquid (often referred to here as the centrifuge tube). Another tube was connected to the lid of the centrifuge tube and connected to the peristaltic pump. The setup made a loop that used the pump to pass air through the spiked filter to bubble radon into the liquid (usually LAB) in the centrifuge tube. The spiking process run time can be varied, but was usually run for at least 2 hours. For the first tests the activities of the feed samples were low (Table 4.1) and after a few trials the activity level became lower. The safety filter (preventing solvent from getting in the spiked filter) had to

be replaced each time. In the following documentation, the experiments using this spike setup have an experiment ID with *PbSp* in the name.

Experiment ID	Activity (Bq)
PbSp1	$0.82 \pm 0.04$
PbSp2	$0.71 \pm 0.04$
PbSp3	$0.82 \pm 0.04$
PbSp4	$0.20 \pm 0.01$
PbSp5	$0.53 \pm 0.03$
PbSp6	$0.09 \pm 0.01$

Table 4.1: Activities from first small spike.

The results for the tests using the first spike setups are described below (Sections 4.3 and 4.4) and the results were used as preliminary tests to provide information about the state of the lead in the LAB. These tests provided information about where to focus the purification efforts, but for more conclusive and definitive results it was necessary to make a new spike setup. This spike setup, Figure 4.1(b), utilizes a small column instead of simply a small filter. The column was 5 cm long compared to the less than 1 cm thickness of the filter. This increase in size allows for more surface area to be covered with the spike; and thus to load more of the spike into the sample as air is passed through.

The column was composed of 0.3 g of HZrO-loaded silica gel column that was spiked with 15.02 g (15 mL) of thorium-228, the same spike source used previously, but with this setup more could be loaded onto the increased surface area. The solution was then passed through the small column of HZrO-loaded silica gel at a rate of less than 0.5 mL/minute. This slow rate ensures that a large amount of surface coverage by the spike is achieved. To maximize the coverage on the column, the excess solution from the first pass was passed through the column a second time.

The setup flow is essentially the same as the previous setup, with air flowing through the spiked column and then bubbled into the liquid in the centrifuge tube.

The second piece of tubing connected to the centrifuge tube continues the loop of air to the peristaltic pump through the column. Similar to the previous setup, there is some danger of the solvent flowing backwards into the column. To avoid this occurrence, a safety filter is placed between the column and the centrifuge tube connection. The experiments using this spike setup have an experiment ID with *ThRaSp* or *PbDS* in the name. Using this new setup the spike was allowed to run for three to five hours. The increased spiking time increased the radon activity transferred to the scintillator samples and it also gave more consistent count numbers between trials (Table 4.2). In Figure 4.2 the actual setup is shown. The 50 mL centrifuge tube can be seen as an indication of the scale of the setup.

Experiment ID	Activity (Bq)
ThRaSp3	$2.5 \pm 0.1$
ThRaSp4	$2.0 \pm 0.1$
ThRaSp5	$3.5 \pm 0.2$
ThRaSp6	$2.3 \pm 0.1$
ThRaSp7	$3.1 \pm 0.2$
ThRaSp8	$3.5 \pm 0.2$

Table 4.2: Activities from small spike

The spike is made from a 80 Bq  $^{228}\text{Th}$  liquid source and uses air passing through the column and bubbling  $^{220}\text{Rn}$  into the solvent to spike. The  $^{220}\text{Rn}$  has a half-life of 55.6 seconds, the spiked liquid is always left to stand for ten to fifteen minutes to allow the  $^{220}\text{Rn}$  to decay into  $^{212}\text{Pb}$ . The half-life of  $^{212}\text{Pb}$  is 10.64 hours which is long enough for the tests to be completed without significant decay of the isotope affecting results. In SNO+, the problematic radioisotope is  $^{210}\text{Pb}$ , however, it would be very difficult to make a spike of  $^{210}\text{Pb}$  because the half-life is 22.2 years so it would be much more difficult to measure the activity of the samples. However, as lead isotopes are chemically indistinguishable, the isotope  $^{210}\text{Pb}$  can be approximated by  $^{212}\text{Pb}$ . The properties of  $^{212}\text{Pb}$  in the LAB should be the same as any potential contamination of

$^{210}\text{Pb}$ .

For all the tests one of the measures of success of the experiment is extraction efficiency. The extraction efficiency is calculated in Equation 4.1:

$$efficiency = \frac{\left(1 - \frac{C_S}{M_{LAB}}\right)}{\left(\frac{C_F}{M_F}\right)} * 100\% \quad (4.1)$$

where  $C_F$  is the feed count rate,  $C_S$  is the purified sample count rate,  $M_{LAB}$  is the mass of the spiked LAB and  $M_F$  is the mass of the feed sample. It is a measure of the fraction of impurity removed from the spiked sample. The extraction efficiency allows for easy comparison between different purification tests and methods.

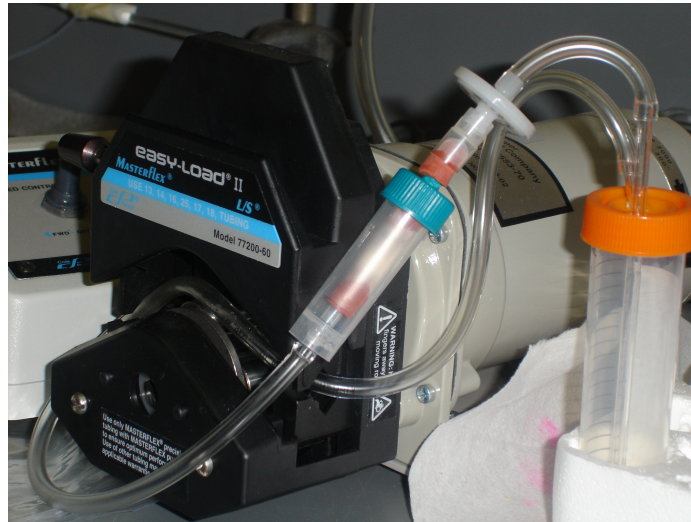


Figure 4.2: Photograph of Pb spike setup with 50mL centrifuge tube on the right side for scale size. Maximum amount of spiked liquid at a time is 50mL.

## 4.2 $\beta$ - $\alpha$ Counting Technique

In order to determine the success of the experiment there must be some way to count the activity in a sample before and after purification. The method used to determine these activities is often referred to as the counting technique, where the number of counts is related to the total activity in a sample. The counting technique that was used to determine the amount of contaminant in the liquid scintillator purification tests is  $\beta$ - $\alpha$  coincidence counting. In  $\beta$ - $\alpha$  coincidence counting a  $\beta$  decay event and an  $\alpha$  decay event that occur in a short, well-defined time window are said to be in coincidence with each other and are characteristic of a particular decay event. Each coincidence is referred to as a *count* and the process of measuring the activity of the sample via this method is referred to as *counting*.

There are two beta-alpha coincidences that are used in this counting technique. From the thorium-232 decay chain, there is the beta decay of  $^{212}\text{Bi}$  decays with a 60.6 minute half-life to  $^{212}\text{Po}$ . The  $^{212}\text{Po}$  then undergoes alpha decay with a half-life of 299 nanoseconds to stable  $^{208}\text{Pb}$ . The Q-value of the beta decay is 2.25 MeV and the Q-value of the alpha decay is 8.95 MeV. In the uranium chain, the beta-alpha coincidence involves  $^{214}\text{Bi}$  beta decaying with a half-life of 19.9 minutes to  $^{214}\text{Po}$ . The  $^{214}\text{Po}$  alpha decays to  $^{210}\text{Pb}$  with a half-life of 164 microseconds. For this coincidence, the Q value of the beta decay is 3.27 MeV and the alpha decay is 7.83 MeV. Figures 4.3(a) and 4.3(b) show the relevant parts of the decay chains where these coincidences occur.

A beta-alpha coincidence counting system was developed in Oxford for the SNO project [71]. The detector used in the counting setup consists of a photomultiplier tube (PMT) surrounded by Oxygen-Free High Conductivity (OFHC) copper that is 2.5 cm thick to shield the detectors from gamma particles (Figure 4.4(b)). The detector is sealed to prevent any light from entering. For this setup a sample of up to 12 mL can be counted. In order to improve counting efficiency the samples are

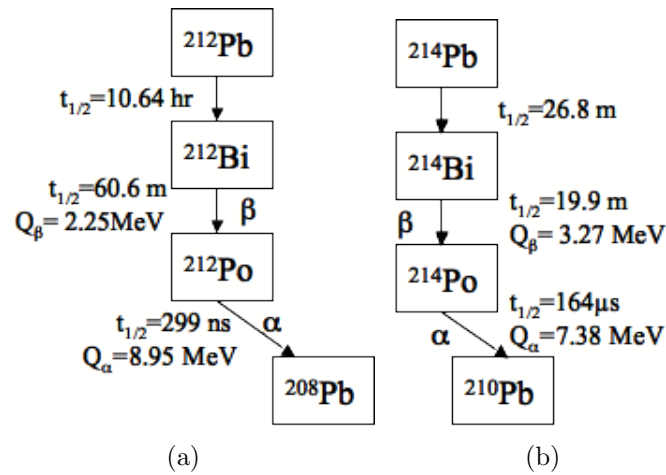


Figure 4.3: (a) Th chain  $\beta - \alpha$  coincidence. (b) U chain  $\beta - \alpha$  coincidence.

mixed with approximately 42 mL of Optiphase HiSafe 3 liquid scintillator cocktail as the fluor. The sample and the Optiphase are both put into the counting pot (Figure 4.4(a)) and counted for three days to a week. The counter is run by Computer Automated Measurement And Control (CAMAC) electronics integrated onto a small electronics board and attach to a high voltage supply. A schematic of the counter connected to the electronics and the high voltage supply is shown in Figure 4.5.

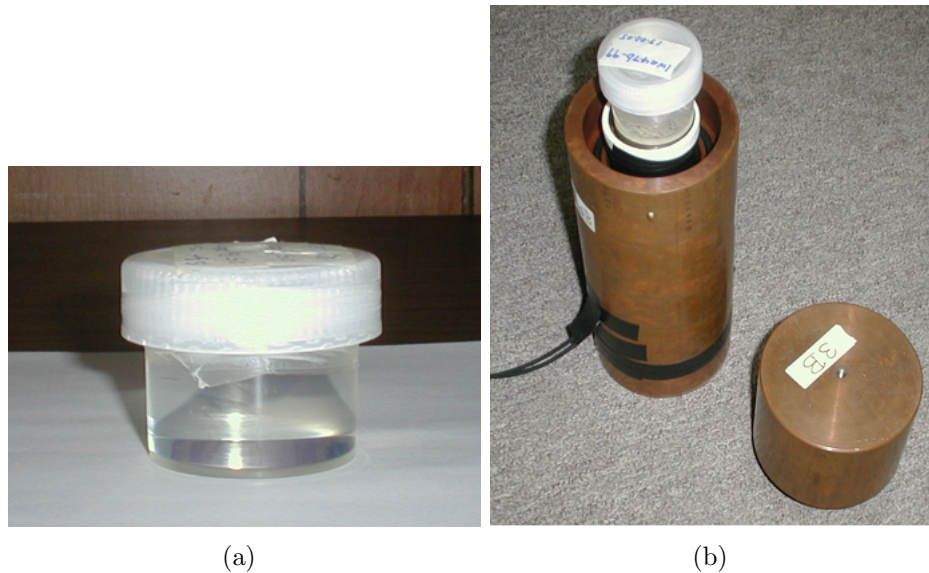


Figure 4.4: (a) counting pot. (b)  $\beta$ - $\alpha$  coincidence detector.

Figure 4.6 shows a schematic of the electronics. The actual electronic circuit used

in the counters for this experiment is similar to Figure 4.6, where the pulse shape of the alphas and betas are used to register the coincidence [72]. Advantages of a  $\beta$ - $\alpha$  delayed coincidence counting system include its high counting efficiencies for the thorium and uranium chains, 45% and 60% respectively. The use of coincidences gives the counting system a low background without any special shielding. The background counts for the thorium chain are less than one count per day and the uranium chain only has two to three counts per day. The counters are easy to maintain at a low

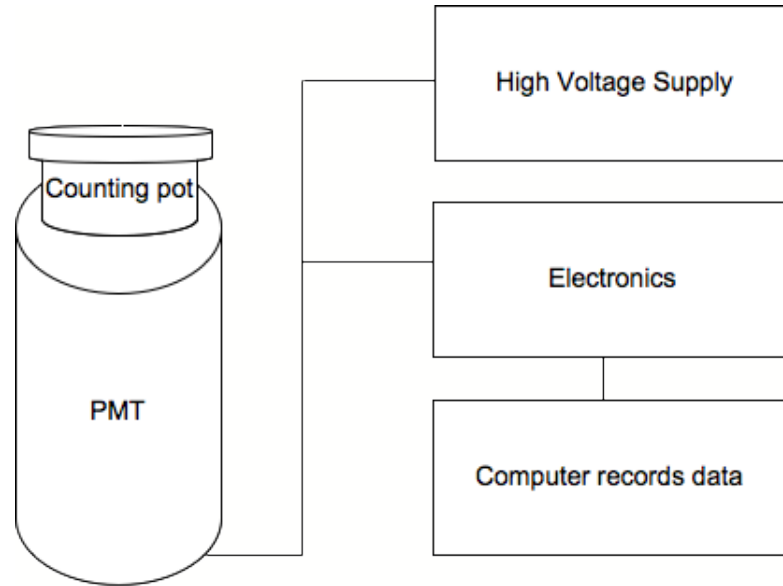


Figure 4.5: Schematic of the  $\beta - \alpha$  counting system.

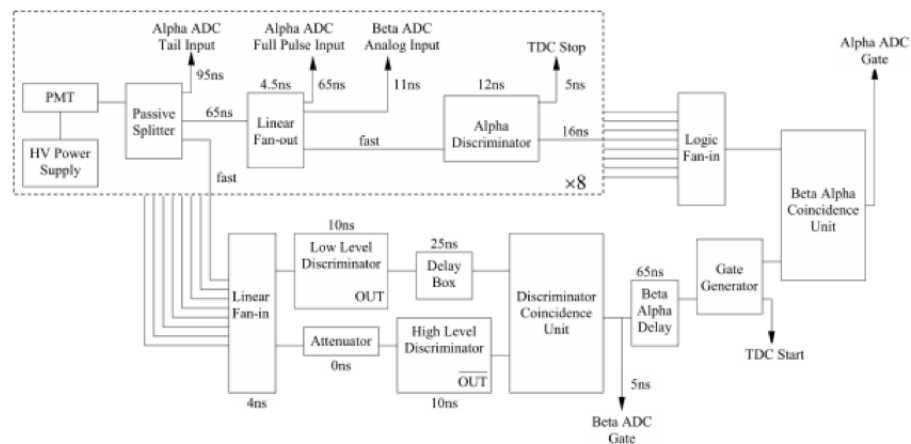


Figure 4.6: Electronics block diagram of the  $\beta - \alpha$  counters [72].

cost. In all the calculations in this section a 5% uncertainty is used to reflect the systematic uncertainty of the counting system. This uncertainty accounts for sample variations, air exposure during preparation of the samples and fake coincidences in counting.

### 4.3 Water and Acid Extraction

Both water extraction and acid extraction are classified as *liquid-liquid extraction*. The basic principle of liquid-liquid extraction is that two immiscible liquids are mixed together, so that an impurity that is more soluble in one liquid than the other can be transferred to its “preferred host,” in an attempt to extract an impurity from one of the liquids into the other. Figure 4.7 shows the three steps involved in liquid-liquid extraction: (4.7(a)) the two liquids are added together, (4.7(b)) the mixture is shaken, and 4.7(c) the two phases are allowed a period of quiescence to settle.

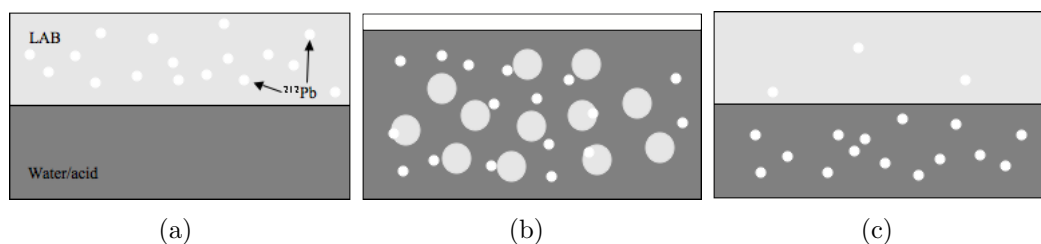


Figure 4.7: (a) step one: two immiscible liquids, one with an impurity (b) step two: the two liquids are mixed together (c) step three: the impurity from one liquid is transferred into the other liquid.

The first purification test was water extraction. This method is the simplest of all methods that was used. The basic procedure for this test was to spike the LAB with the spike setup shown in Figure 4.1(a) for thirty minutes to two hours (spiked for longer to try to increase activity). After the spiking time, the sample was allowed to sit for ten minutes to allow the radon to decay. For every trial a *feed sample* was always taken first. This involved measuring 10 mL of the spiked LAB into a counting pot, adding the Optiphase HiSafe 3 and setting it aside for counting. The water extraction was done by adding equal parts spiked LAB to ultra pure water (UPW). This combination was shaken vigorously by hand for about ten minutes until the sample was completely mixed. It was then allowed to settle into the two phases: water and solvent (LAB). After separation, a sample was taken from each phase. When the sample separates into two phases, the LAB is the top layer due to its lower density

than water. Approximately 10 mL of the LAB phase was pipetted into a counting pot for counting. The remaining LAB was pipetted off and a sample of the water phase pipetted into a second counting pot. The Optiphase HiSafe cocktail was added to both samples and all three samples were counted for three days.

For tests with experiment ID *PbSp2 – PbSp5* an additional calculation was used to determine a more accurate feed count, because often the feed count rate was lower than the purified count rate. Equation 4.2 shows how the feed counting rate was calculated and Equations 4.3 and 4.4 show how this adjusted feed counting rate is used to calculate the extraction efficiency for these tests. There are two different efficiency calculations (Equations 4.3 and 4.4), the first for UPW extraction from spiked LAB and the second for LAB extraction from spiked UPW.

$$C_F = C_L * \frac{M_{LT}}{M_{LS}} + C_W * \frac{M_{WT}}{M_{WS}} \quad (4.2)$$

$$Efficiency = \left( \frac{C_W * \frac{M_{WT}}{M_{WS}}}{C_L * \frac{M_{LT}}{M_{LS}} + C_W * \frac{M_{WT}}{M_{WS}}} \right) * 100\% \quad (4.3)$$

$$Efficiency = \left( 1 - \frac{C_W * \frac{M_{WT}}{M_{WS}}}{C_L * \frac{M_{LT}}{M_{LS}} + C_W * \frac{M_{WT}}{M_{WS}}} \right) * 100\% \quad (4.4)$$

In Equations 4.2 - 4.4,  $C_F$  is the counts from the feed sample,  $C_L$  is the counts from the LAB sample,  $C_W$  is the counts from the UPW sample,  $M_{LT}$  is the mass of total LAB spiked,  $M_{LS}$  is the mass of the sample of LAB counted,  $M_{WT}$  is the mass of the total UPW used for extraction,  $M_{WS}$  is the mass of the sample of UPW counted and  $C_W$  is the counts from the UPW sample. Table 4.3 gives the raw data used to calculate the extraction efficiencies. The extraction efficiencies can be seen in Table 4.4. The extraction efficiency is given as a upper limit because the initial spike setup did not produce a large activity and was not consistent between tests. However, as

these are preliminary tests the limit is sufficient.

Exp-ID	Spike Time	Counts Feed, Mass (counts/hour)	Counts Purified, Mass (counts/hour)	Count Time
PbSp2	30 minutes	1540 $\pm$ 56, 19.6 g	147 $\pm$ 5, 10.1 g	72 hours
PbSp3	30 minutes	1293 $\pm$ 138, 17.7 g	538 $\pm$ 10.8, 8.5 g	90 hours

Table 4.3: Raw data from LAB extraction from spiked UPW

Exp-ID	Spiked in	Extracted by	Extraction Efficiency
PbSp2	24.6g LAB	19.6g UPW	< 18.5 %
PbSp3	20.2g LAB	17.7g UPW	< 1.4 %

Table 4.4: Results from water extraction from spiked LAB

As can be seen from the results in Table 4.4 the extraction efficiency was very low, recall that tests with experiment ID *PbSp* refer to the initial spike setup. In order to further probe the properties of this extraction method, the experiment was done in reverse. This time the water was spiked for thirty minutes and again allowed to decay for ten minutes. Again a feed sample was taken, and set aside for counting. This time the nonspiked LAB was added to the spiked water and shaken and then samples pipetted into counting pots. All three samples were counted and the raw data used to calculate the extraction efficiencies is shown in Table 4.5 and the results are displayed in Table 4.6.

Exp-ID	Spike Time	Counts Feed, Mass (counts/hour)	Counts Purified, Mass (counts/hour)	Count Time
PbSp4	30 minutes	1307 $\pm$ 169, 20.5g	297 $\pm$ 8, 4.7 g	72 hours
PbSp5	30 minutes	860 $\pm$ 56, 10 g	302 $\pm$ 6, 9.1 g	90 hours

Table 4.5: Raw data from LAB extraction from spiked UPW

Similarly, the reverse experiment yielded very low extraction efficiencies; and so one final method of water extraction was attempted. Instead of room temperature

Exp-ID	Spiked in	Extracted by	Extraction Efficiency
PbSp4	20.5g UPW	8.1g LAB	< 0.5%
PbSp5	24.2g UPW	12.0g LAB	< 6.7%

Table 4.6: Results from LAB extraction from spiked UPW

water, hot water (80 – 90°C) was used. It is possible that some impurities are more likely to be removed by hot water than by room temperature water. The raw data from this experiment is shown in Table 4.7 and the extraction efficiency in Table 4.8. The hot water extraction did not work at all, the feed counts were lower than the purified counts. The water extraction tests showed no consistent results and all with very low extraction efficiencies. From these results it was determined that water extraction was not appropriate for this purification task.

Exp-ID	Spike Time	Counts Feed, Mass (counts/hour)	Counts Purified, Mass (counts/hour)	Count Time
PbSp6-1	2 hours	16.6 ± 1.2, 7.7 g	23.5 ± 1.9, 7.4 g	47 hours

Table 4.7: Raw data from hot water extraction test

Exp-ID	Spiked in	Extracted by	Extraction Efficiency
PbSp6-1	7.4g LAB	~10g UPW 90C	No Extraction

Table 4.8: Results from hot water extraction from spiked LAB

The next method tested was acid extraction. The methodology of acid extraction is very similar to water extraction. The LAB was spiked for two hours and set to decay for ten minutes. A sample of the spiked LAB was set aside for counting. Then 10 mL of 0.1 M nitric acid (HNO<sub>3</sub>) was added to 10 mL of LAB. The combination was shaken for ten minutes by hand. The two phases were allowed to completely settle and then the top layer, the LAB, was pipetted into the counting pot. A sample of the acid layer was then pipetted into a counting pot.

Exp-ID	Spike Time	Counts Feed, Mass (counts/hour)	Counts Purified, Mass (counts/hour)	Count Time
PbSp6-3	2 hours	$16.6 \pm 1.2$ , 7.7 g	$14.3 \pm 1.2$ , 7.0 g	47 hours

Table 4.9: Raw data from acid extraction test

Experiment ID	Spiked in	Extracted by	Extraction Efficiency
PbSp6-3	15.1 LAB	10g 0.1M HNO <sub>3</sub>	< 15.5 %

Table 4.10: Results from acid extraction from spiked LAB

The raw data from the acid extraction is shown in Table 4.9 and the extraction efficiency results (Table 4.10) show the acid extraction also yielded a low extraction efficiency.

Based on the results from Tables 4.4-4.10, the water and acid extraction tests were not successful in reducing the <sup>212</sup>Pb levels in the samples as shown by the extraction efficiencies lower than 20%. The inability for water or acid extraction to remove the <sup>212</sup>Pb from the LAB suggests that the majority of the <sup>212</sup>Pb contaminant is not in an ionic or metallic chemical state and is therefore most likely in an organic state.

## 4.4 Adsorption

Since the simple methods of extraction were not effective, it was necessary to try more complicated methods, the first being *adsorption*. Adsorption is simply defined as a process wherein a liquid (or gas) with impurities passes through a solid and the impurities adhere (or are adsorbed) to the surface area of the solid [73]. Characteristics of the solid, or the adsorbent, used to remove the impurities are a large surface area and porosity. Both these features allow for the most possible impurities to be adsorbed onto the surface area. Figure 4.8 shows pictorially how the impurities are adsorbed onto the surface of the adsorbent.

There are many advantages to the adsorption extraction method, including the ability to do specific separations based on high selectivity of adsorbents. It is also possible to pass large amounts of bulk liquid through the adsorbent continuously purifying. There are a few drawbacks, including the need to periodically regenerate the adsorbent, as well as the possibility of breakthrough if not properly monitored [73]. Breakthrough is a phenomenon that occurs when the adsorbent has adsorbed a maximum amount of impurities, becomes ineffective at purifying further and can re-contaminate the liquid that has already been purified (in the case of continuous purification). This is especially crucial in a continuous purification process of large amounts of liquid because it can re-contaminate the entire bulk solution, not just a small amount as in a batch method.

Unlike the previous tests, adsorption has another quantity that can be measured to help determine the success of the experiment: the *distribution coefficient*,  $K_d$ . In most situations the distribution coefficient is calculated by Equation 4.5:

$$K_d = \left( \frac{C_F - C_S}{C_S} \right) \left( \frac{M_A}{M_{LAB}} \right) \quad (4.5)$$

where  $M_A$  is the mass of the adsorbent,  $C_F$  is the feed counts,  $C_S$  is the purified

sample counts, and  $M_{LAB}$  is the mass of the LAB. The distribution coefficient is used as an indicator of the sorption behavior of a material. When an experiment is set up such that new masses of spiked solvent are being added to the same adsorbent, a more complicated calculation of  $K_d$  is needed:

$$K_{d_1} = \left( \frac{C_F - C_{S_1}}{C_{S_1}} \right) \left( \frac{M_A}{M_{LAB_1}} \right) \quad (4.6)$$

$$K_{d_2} = \left( \frac{(C_F - C_{S_1}) + (C_F - C_{S_2})}{C_{S_2}} \right) \left( \frac{M_A}{M_{LAB_2}} \right) \quad (4.7)$$

$$K_{d_3} = \left( \frac{(C_F - C_{S_1}) + (C_F - C_{S_2}) + (C_F - C_{S_3})}{C_{S_3}} \right) \left( \frac{M_A}{M_{LAB_3}} \right) \quad (4.8)$$

where  $C_{S_i}$  ( $i=1,2,3$ ) is the purified sample counts. Equations 4.6-4.8 show the distribution coefficient for three steps, but the process and equations could be extended to as many steps as necessary. The distribution coefficient is calculated for the adsorption tests that follow.

Three different adsorbants were used in the purification tests: silica gel, HZrO

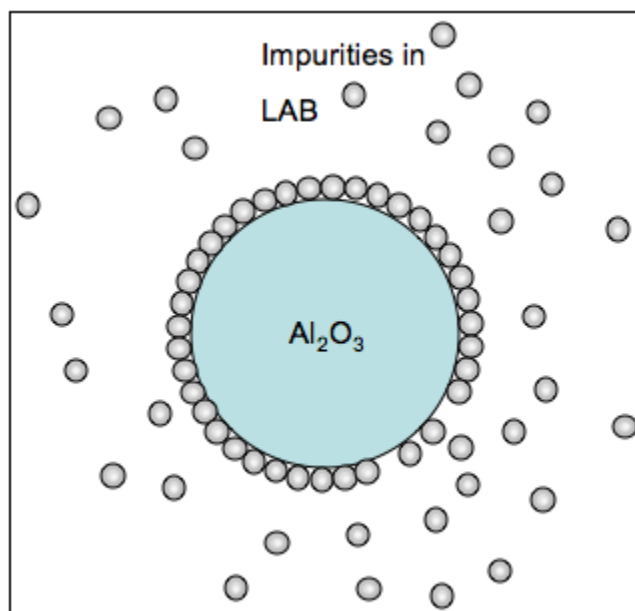


Figure 4.8: Depiction of impurities being adsorbed onto a bead of  $Al_2O_3$

loaded silica gel, and aluminium oxide (also referred to as alumina, or by its chemical formula  $\text{Al}_2\text{O}_3$ ). In the first test a HZrO coated filter was prepared using methanol to wet a clean syringe filter and then 0.5 mL of 1% HZrO solution was slowly passed through the filter with 4.0  $\text{cm}^2$  of surface area. It was then rinsed with 10 mL of ultra pure water (UPW), then 5 mL of methanol, and then let to dry for thirty minutes. The result was a HZrO coverage of 12.5  $\text{g}/\text{m}^2$  and a 0.45  $\mu\text{m}$  pore size. The LAB was spiked for thirty minutes and then allowed to sit for ten minutes for the radon to decay. A feed sample of 10 mL was set aside for counting and then 10 mL of the spiked LAB was passed through the coated filter at a rate of about 1 mL/min. The LAB passed through the filter was collected into a counting pot. Both samples were mixed with Optiphase HiSafe and counted.

In the remainder of the tests in Table 4.11, the LAB was spiked for two hours, allowed to decay for ten minutes and a feed sample set aside for counting. The extraction agents were added to the LAB and each combination was shaken for ten minutes and then the particulate was allowed to settle into two phases. When completely settled a 10 mL sample was taken of each test for counting. The raw data from the preliminary adsorption tests is shown in Table 4.11 and the extraction efficiencies are shown in Table 4.12.

Exp-ID	Spike Time	Counts Feed, Mass (counts/hour)	Counts Purified, Mass (counts/hour)	Count Time
PbSp1	30 minutes	530 $\pm$ 11, 8.2 g	514 $\pm$ 10, 8.3 g	92 hours
PbSp6-2	2 hours	16.6 $\pm$ 1.2, 7.7 g	4.8 $\pm$ 0.8, 7.3 g	47 hours
PbSp6-5	2 hours	16.6 $\pm$ 1.2, 7.7 g	2.8 $\pm$ 0.7, 7.7 g	47 hours
PbSp6-4	2 hours	16.6 $\pm$ 1.2, 7.7 g	3.3 $\pm$ 0.8, 6.1 g	47 hours
PbSp7	1 hour	17.1 $\pm$ 1.6, 8.3 g	4.3 $\pm$ 0.6, 6.4 g	64 hours

Table 4.11: Raw data from preliminary results for adsorption tests

The preliminary adsorption tests showed promising extraction efficiency, in contrast to the low extraction efficiencies of the water and acid extractions. However,

Exp-ID	Spiked in	Extracted by	Extraction Efficiency
PbSp1	10mL LAB	HZrO filter (10mg Zr)	< 4.3 %
PbSp6-2	10mL LAB	1.0g silica gel	> 63 %
PbSp6-5	10mL LAB	1.0g HZrO-silica gel	> 67%
PbSp6-4	10mL LAB	1.0g Al <sub>2</sub> O <sub>3</sub>	> 77 %
PbSp7	10mL LAB	0.24g Al <sub>2</sub> O <sub>3</sub>	> 61%

Table 4.12: Preliminary results from adsorption tests.

in order to achieve more conclusive results, it was decided that a new spike (Figure 4.1(b)) would be constructed to do further adsorption tests. With this new setup the LAB was spiked for three (ThRaSp3/4) to four (ThRaSp5) hours and settle for ten minutes as seen in Table 4.13. Each time a feed sample was set aside for counting. In all tests approximately 1 g of adsorbent was added to various amounts of spiked LAB as seen in Table 4.14. For these tests not only was the extraction efficiency calculated, but also the distribution coefficient,  $K_d$ . A larger distribution coefficient,  $K_d$ , indicates a larger amount of impurity adsorbed onto the surface of the adsorbent.

Exp-ID	Spike Time	Counts Feed, Mass (counts/hour)	Counts Purified, Mass (counts/hour)	Count Time
ThRaSp3	3 hours	1011 ± 10, 8.2 g	365 ± 7, 8.2 g	180 hours
ThRaSp4-1	3 hours	705 ± 14, 8.3 g	79 ± 0.8, 8.3 g	23 hours
ThRaSp4-2	3 hours	705 ± 14, 8.3 g	404 ± 4.0, 8.46 g	23 hours
ThRaSp5-1	4 hours	1250 ± 13, 8.2 g	317 ± 6.3, 7.76 g	72 hours
ThRaSp5-2	4 hours	1250 ± 13, 8.2 g	113 ± 3.4, 8.3 g	72 hours
ThRaSp5-3	4 hours	1250 ± 13, 8.2 g	55.8 ± 2.8, 7.2g	72 hours

Table 4.13: Raw data from secondary adsorption tests

The most promising results overall were from the alumina especially from the experiment ThRaSp5 when the longer spike time was used achieving a larger activity. The results from the HZrO loaded silica gel tests were inconsistent, possibly due to desorption, and silica gel produced more consistent results. It was decided that further tests would be done with the adsorbent alumina and silica gel.

Exp-ID	Spiked in	Extracted by	Extraction Efficiency	$K_d$
ThRaSp3	24.12g LAB	0.1g Al <sub>2</sub> O <sub>3</sub>	64.0 ± 4.1%	427 ± 50
ThRaSp4-1	14.5g LAB	0.11g silica gel	88.8 ± 1.2 %	1040 ± 111
ThRaSp4-2	14.7g LAB	0.1g HZrO-silica gel	43.8 ± 6.4%	110 ± 13
ThRaSp5-1	11.47g LAB	0.12g silica gel	74.8 ± 2.5%	282 ± 28
ThRaSp5-2	11.97g LAB	0.10g HZrO silica gel	90.4 ± 1.2%	1160 ± 135
ThRaSp5-3	11.44g LAB	0.12g Al <sub>2</sub> O <sub>3</sub>	94.9 ± 0.6%	2038 ± 226

Table 4.14: Results from secondary adsorption tests

The further tests were designed to test equilibrium times, desorption and exhaustion time. Desorption is when the impurities are released from the surface of the adsorbent. Exhaustion is when the adsorbent can hold no more impurities. Table 4.15 gives the raw data for the equilibrium tests and Table 4.16 shows the calculated results of the equilibrium/desorption tests. For these experiments the LAB was spiked for five hours and then allowed to sit for ten minutes for the radon to decay. A feed sample was set aside for counting. In three separate centrifuge tubes 15 mL of the spiked LAB was pipetted in, and approximately 0.1 g of adsorbent added. The test tubes were mixed with an electric stirrer for three different amounts of time: half an hour, one hour and two hours. After each amount of time the sample was allowed to settle and then a 10 mL sample was taken for counting. Optiphase HiSafe was added to all samples before counting.

The results from the different stirring times were compared. These tests were done to determine if the extraction efficiency would reduce over time and if the  $K_d$  decreases over time. Also both measurements indicate when equilibrium has occurred. The results for these tests are shown in Table 4.16. For the aluminum oxide the efficiency continued to increase as the stirring time increased and the  $K_d$  stabilized after an hour of stirring. The  $K_d$  results for one and two hours are within the range of uncertainty and that indicates that desorption is not occurring. The same test for the silica gel show that there is a larger extraction efficiency jump from a half hour

to an hour time and that the  $K_d$  decreased significantly at the two hour mark. This reduction in  $K_d$  for the silica gel indicated that some of the impurities, namely  $^{212}\text{Pb}$ , are desorbing back into the LAB. This is an undesired effect because it suggests that if the adsorbent is continually circulated through the LAB some of the impurities will go back into the LAB. The results from Table 4.16 indicate that the aluminum oxide is much more stable as far as maintaining steady extraction efficiency and a much lower tendency of desorption.

Exp-ID	Spike Time	Counts Feed, Mass (counts/hour)	Counts Purified, Mass (counts/hour)	Count Time
ThRaSp6-1	4 hours	$841 \pm 8.4$ , 8.34 g	$37.8 \pm 1.9$ , 8.3 g	50 hours
ThRaSp6-2	4 hours	$841 \pm 8.4$ , 8.34 g	$21.8 \pm 1.6$ , 8.3 g	50 hours
ThRaSp6-3	4 hours	$841 \pm 8.4$ , 8.34 g	$18.4 \pm 1.9$ , 8.4 g	50 hours
ThRaSp7-1	4 hours	$1108 \pm 11$ , 8.48 g	$203.9 \pm 4.1$ , 8.6 g	72 hours
ThRaSp7-2	4 hours	$1108 \pm 11$ , 8.48 g	$22.7 \pm 1.4$ , 8.6 g	72 hours
ThRaSp7-3	4 hours	$1108 \pm 11$ , 8.48 g	$55.6 \pm 2.8$ , 8.5 g	72 hours

Table 4.15: Raw data from equilibrium and desorption tests

Exp-ID	Spiked in	Extracted by	Extraction Efficiency	$K_d$
ThRaSp6-1	11.47g LAB	0.11g $\text{Al}_2\text{O}_3$ , 0.5hr	$95.5 \pm 0.5\%$	$2218 \pm 260$
ThRaSp6-2	12.08g LAB	0.10g $\text{Al}_2\text{O}_3$ , 1hr	$97.4 \pm 0.3\%$	$4536 \pm 610$
ThRaSp6-3	11.83g LAB	0.12 g $\text{Al}_2\text{O}_3$ , 2hr	$97.8 \pm 0.3\%$	$4412 \pm 639$
ThRaSp7-1	11.51g LAB	0.11g silica, 0.5hr	$81.9 \pm 1.9\%$	$464 \pm 50$
ThRaSp7-2	11.88g LAB	0.10g silica 1hr	$98.0 \pm 0.3\%$	$5674 \pm 729$
ThRaSp7-3	11.46g LAB	0.10g silica 2hr	$95.1 \pm 0.6\%$	$2211 \pm 275$

Table 4.16: Results from equilibrium and desorption tests. Tests are completed for different stirring times.

The final test will determine if the alumina can be exhausted quickly. In this test the LAB was spiked for five hours and then let to decay for 30 minutes. As before, a feed sample was set aside for counting. The remaining LAB was divided into three centrifuge tubes, approximately 15 mL each. To one of the tubes of spiked LAB 0.3

g of  $\text{Al}_2\text{O}_3$  was added and electrically stirred for an hour. It was then allowed to settle completely and a sample taken for counting. The remaining LAB was pipetted off until just the  $\text{Al}_2\text{O}_3$  remained. To the  $\text{Al}_2\text{O}_3$ , the second amount of spiked LAB was added, stirred for an hour and then a sample taken for counting. Once again the remaining LAB was pipetted off and the last round of spiked LAB added. The same procedure was followed for this last round of spiked LAB.

The raw data from the exhaustion tests can be seen in Table 4.17 and the extraction efficiency and  $K_d$  of this last test can be seen in Table 4.18. The important result from this test is that the extraction efficiency maintained a steady value throughout all three trials. As well, the  $K_d$  continued to increase showing that it continued to be able to adsorb larger amounts of impurities onto the surface. Both these results indicate that the aluminum oxide cannot be quickly exhausted.

Exp-ID	Spike Time	Counts Feed, Mass (counts/hour)	Counts Purified, Mass (counts/hour)	Count Time
ThRaSp8-1	4 hours	$1256 \pm 12.6$ , 8.34 g	$20.3 \pm 1.7$ , 9.3 g	72 hours
ThRaSp8-2	4 hours	$1256 \pm 12.6$ , 8.34 g	$29.8 \pm 1.8$ , 8.0g	72 hours
ThRaSp8-3	4 hours	$1256 \pm 12.6$ , 8.34 g	$33.4 \pm 1.7$ , 8.66 g	72 hours

Table 4.17: Raw data from  $\text{Al}_2\text{O}_3$  exhaustion tests

Exp-ID	Spiked in	Extracted by	Extraction Efficiency	$K_d$
ThRaSp8-1	11.95g LAB	0.3g $\text{Al}_2\text{O}_3$ , 1hr	$98.6 \pm 0.14\%$	$2427 \pm 252$
ThRaSp8-2	12.04g LAB	0.3g $\text{Al}_2\text{O}_3$ , 1hr	$97.5 \pm 0.2\%$	$3312 \pm 225$
ThRaSp8-3	13.09g LAB	0.3g $\text{Al}_2\text{O}_3$ , 1hr	$97.4 \pm 0.2\%$	$5012 \pm 314$

Table 4.18: Results to determine if  $\text{Al}_2\text{O}_3$  can be quickly exhausted.

## 4.5 Vacuum Distillation

The final purification method used was *vacuum distillation*, which is a very successful method used in many purification situations. Chunlin Lan, a former M.Sc. student working with SNO+, was successful with preliminary vacuum distillation of LAB for SNO+. His results will be discussed and then compared to a second round of vacuum distillation with improvements to the spike setup [63].

As in previous experiments, the extraction efficiency is used as a method of comparing the success of different distillation trials. Another measure of the success of distillation is called the reduction factor.

$$\text{Reduction Factor} = \frac{(C_F/W_F)}{(C_S/W_S)} \quad (4.9)$$

Where  $C_F$  is feed counts,  $W_F$  is feed weight,  $C_S$  is the counts of the purified sample, and  $W_S$  is weight of the purified sample. The ideal reduction factor for SNO+ would be between  $10^5 - 10^6$ .

Vacuum distillation is simply normal distillation performed under vacuum. The basic principle of distillation is that a liquid mixture is brought to a boil. The different components of the liquid (LAB and impurities) have different volatilities and have different vapour pressures. It is this difference that allows separation of impurities from the bulk of the liquid as they remain behind after distillation. This process can be done multiple times on the same sample to achieve improved purification. Figure 4.9 shows the vacuum distillation setup used for these experiments.

When distilling the LAB, the vacuum setup is necessary because the boiling point of LAB is at high temperature. LAB boils in the range of  $278 - 314^\circ\text{C}$  at 1 atm; with a 40-70 mTorr vacuum, the boiling point is between  $70 - 90^\circ\text{C}$ . To achieve this vacuum level it is necessary to create a seal at every joint in the glassware setup. This is done with careful construction and vacuum grease to minimize air leaks. To

achieve the low pressures, a two stage high vacuum pump with a Leeson 0.5 horse power motor was used.

The raw data from vacuum distillations performed by Chunlin Lan are shown in Table 4.19. As can be seen from the results in Table 4.19, the extraction efficiencies and reduction factors are only stated as lower limits. The counts for the purified sample were at the level of the background counting rate, which is approximately  $2 \pm 2$  counts per hour. The background counts originate from  $^{212}\text{Pb}$  in the air and the samples can be exposed to air during the preparation. Since the background counts are at the same level as the purified sample counts, a much stronger spike was needed in order to achieve higher activity and yield results that are not simply a lower limit.

Exp-ID	Spike Time	Counts Feed (counts/hour)	Counts Purified (counts/hour)	Count Time
PbDs1	3 hours	$645.6 \pm 12.9$	$3.01 \pm 0.59$	70 hours
PbDs2	2 hours	$102.4 \pm 3.04$	$6.825 \pm 0.625$	100 hours
PbDs3	4 hours	$1440.1 \pm 14.4$	$1.651 \pm 0.284$	140 hours

Table 4.19: Raw data from initial vacuum distillation tests [63]

The new spike was much larger in strength than the other two previous spike setups. The procedure for making this spike was similar to the previous spike setup, however there were improvements made to ensure the radioactivity was safely con-



Figure 4.9: Vacuum distillation setup.

Experiment ID	Extraction Efficiency	Reduction Factor
PbDS1	> 99.47%	> 187
PbDS2	> 93.4%	> 15
PbDS3	> 99.85%	> 650

Table 4.20: Vacuum distillation results [63]

tained in the column. The spike is loaded on a mixture of silica gel (as before) and of Dowex 50WX8 cation resin. The resin helps the spike stay in the column and reduces leakage. The silica gel/resin combination is contained in a column made of cast acrylic that is 10 cm in length, 2.5 cm in outer diameter and 1.0 cm inner diameter. For the loading of the  $^{228}\text{Th}$ , the bottom of the column has a polypropylene luer-lock adaptor with three layers of nylon membrane and is threaded to snugly lock. To load the spike, 1  $\mu\text{Ci}$  of the  $^{228}\text{Th}$  is mixed with 10 mL of 0.5 M HCl and slowly passed through the resin/silica column. The excess is collected and passed through two more times to ensure maximum coverage. Then UPW is passed through the column, followed by air to dry the resin. When completely dried the luer-lock adaptor is securely attached to the top of the column. The entire column is encased by copper shielding to protect the surroundings from contamination. The spike is not so strong that it is of danger to the experimenter, but it is strong enough to contaminate surrounding experiments, so great care was needed in preparing the spike and handle all equipment to avoid cross contamination. The finished setup can be seen in Figure 4.10.

The new spike provides a larger activity than with the previous spikes. Table 4.2 shows the activities achieved in the tests used in the second round of testing and Table 4.21 shows the activities achieved in the tests with the larger spike setup. As can be seen from the two tables, the activities of the new spike setup are consistently almost 1000 Bq or higher. Another requirement of this new spike was that it be primarily  $^{212}\text{Pb}$  and be low in  $^{228}\text{Th}$ . Figure 4.11 is data taken from the first test of the new spike. For the first test of the spike, two samples were made: the first was

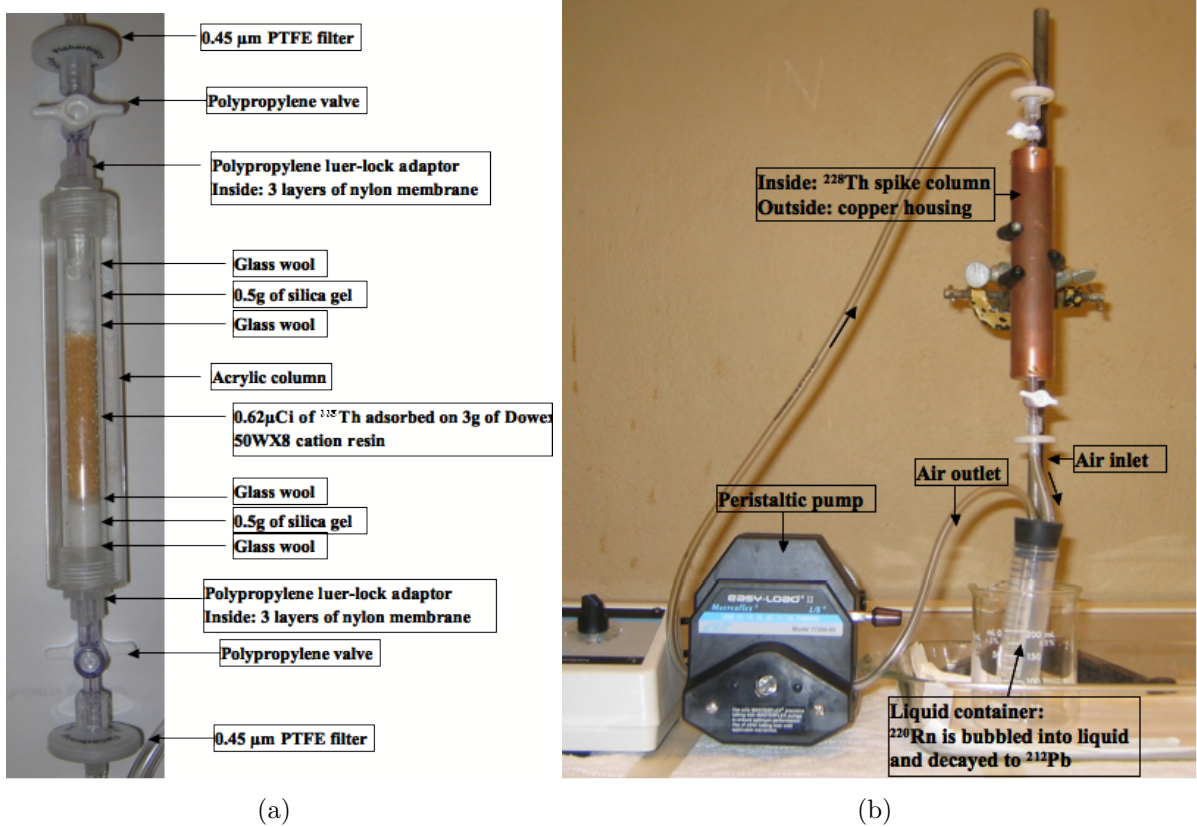


Figure 4.10: (a) The spike column (b) The spike setup.

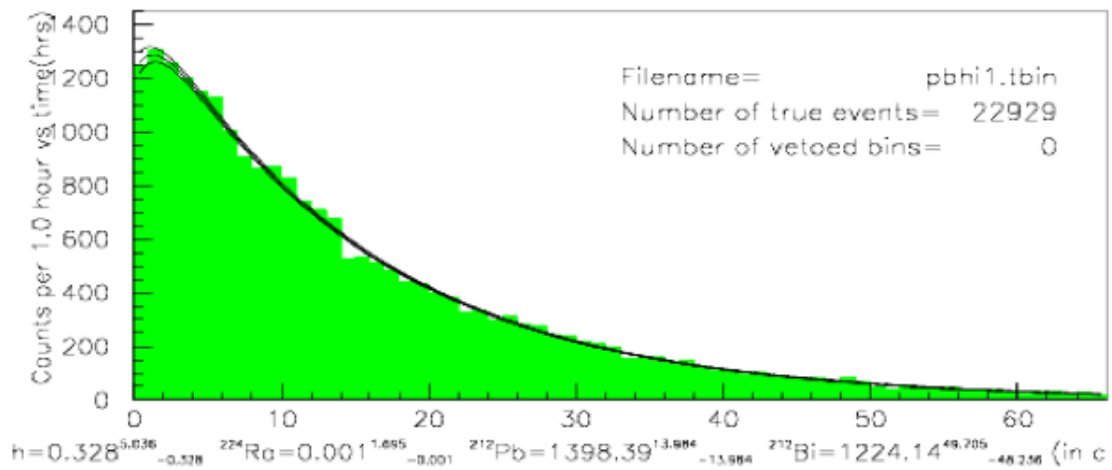
20  $\mu\text{L}$  of the spiked LAB mixed with Optiphase HiSafe for counting and the second was 10 mL of the spiked LAB mixed with Optiphase HiSafe. Figure 4.11(a) shows the first sample counted immediately after spiking and Figure 4.11(b) shows the second sample one week later. The reduction factor of  $7.0 \times 10^8$  after one week of counting shows that there is no long lived thorium getting through the spike setup.

Experiment ID	Activity (Bq)
PbHi2	$1190 \pm 61$
PbHi3	$960 \pm 49$
PbHi4	$1660 \pm 84$
PbHi5	$1590 \pm 81$
PbHi6	$2409 \pm 123$
PbHi7	$2853 \pm 146$
PbHi8	$4683 \pm 239$
PbHi9	$2764 \pm 141$

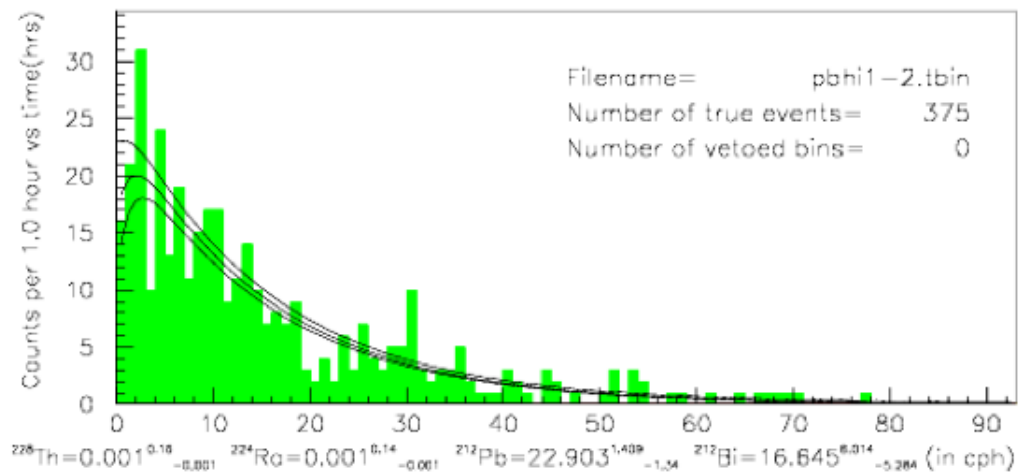
Table 4.21: Activities from new, larger spike.

With the activity significantly higher and thorium-free, the spike was ready to be used for vacuum distillation purification tests. The goal for the reduction factor for these tests was  $10^5 - 10^6$ . For the first test, PbHi2, 20 mL of LAB was spiked for 4 hours and then allowed to decay for an hour. A 20  $\mu\text{L}$  sample was taken and combined with Optiphase HiSafe and set aside for counting. The remaining spiked LAB was distilled under a vacuum of 50–70 mTorr and at a temperature of 70–80°C. The results for all the new spike tests are shown in Table 4.23. The result for PbHi2 gave a reduction factor of  $300 \pm 16$  which is less than the previous small scale tests achieved and much less than the desired goal. There are a few possibilities for the cause of this decrease in impurity reduction. It is possible that during the distillation some of the Pb splashed into the clean side of the apparatus due to distilling too quickly or that near the end of the distillation some of the contaminants were able to vapourize and condense on the purified side, or some combination of the two.

In order to achieve a better reduction factor, for the second test, PbHi3, 30 mL



(a)



(b)

Figure 4.11: (a) A plot of the activity of a 20  $\mu\text{L}$  sample of the spiked LAB taken the day of spiking (b) A plot of the activity of a 10 mL sample of spiked LAB taken one week after spiking.

of LAB was spiked for 4 hours and then allowed to decay, and a 20  $\mu\text{L}$  sample of the spiked LAB was added to Optiphase and set aside for counting. The remaining 30 mL was distilled, this time taking a sample for counting after 15 mL had been distilled and then another after all remaining LAB was distilled. The results are shown in Table 4.23, labelled PbHi3-1 for the first sample and PbHi3-2 for the second sample. The double sampling yielded no significant change in reduction factor, indicating the contamination was occurring throughout and not near the end. The next idea to improve the apparatus was to add a long glass connector at the beginning of the apparatus to increase the distance that the vapour has to travel. The results of this test are shown in Table 4.23 as PbHi4. This additional piece of glass produced an increased reduction factor of 3-4 times the previous value.

The reduction factor was still not as high as desired, so for the PbHi5 test a combination of adsorption and distillation was used. For the test 40 mL of LAB was spiked for 4 hours, and then allowed to decay for an hour. A 20  $\mu\text{L}$  sample was added to Optiphase and set aside for counting. To the remaining 40 mL, 0.1g of  $\text{Al}_2\text{O}_3$  was added. The distillation was done as usual under 50-70 mTorr and between 70 – 80°C and alumina remained in the LAB during the distillation. The results in Table 4.23 show a greatly improved reduction factor of  $7284 \pm 430$ . The test was repeated in exactly the same fashion in order to determine if the results were repeatable. The result of the repeated experiment, PbHi6 are shown in Table 4.23. It can be seen that the reduction factor is  $9480 \pm 560$ , which is larger than the previous trial and shows that using alumina adsorption in addition to distillation is successful in removing a large portion of the lead.

The last purification test that was used is double distillation, which is when the spiked LAB is distilled twice. In order to perform a successful double distillation it is important to reduce cross contamination to a minimum. This requires using two different sets of glassware for each distillation and to avoid any contact between

the spiked LAB and the second distillation. As with the other tests, 40 mL of LAB was spiked for 4.5 hours and then allowed to decay for an hour. Both distillations were done under a vacuum of 50-60 mTorr and temperature of 65 – 80°C. The first distillation is essentially the same as experiment PbHi4 and gave a reduction factor of  $1153 \pm 63$ . The second distillation had the same setup as PbHi2 and PbHi3 with no glassware extension. The reduction factor after both distillation were complete was  $3370 \pm 170$ . It was expected that the results of the double distillation would be at least as good as the alumina plus distillation results.

The experimental setup was evaluated to determine where, if any, cross contamination had occurred. One possibility was that the preparation of the sample may have contributed to some contamination as the same pipette bulb was used, even though a different glass pipette was in direct contact with the sample. The same thermometer was also used for both experiments, and although it was rinsed between distillations it is possible that contamination remained.

The double distillation was redone twice, the raw data is shown in Table 4.22. The results are indicated by PbHi8-1,2 and PbHi9-1,2 in Table 4.23. Both experiments were done without a thermometer to remove the chance of contamination from the first distillation to the second distillation. This proved more difficult than anticipated to control the temperature during the experiment and as an effect, the boiling speed. As well, in PbHi8-2 there was a stir bar malfunction that resulted in possible contamination. The results from PbHi8 indicate that the second distillation was not as successful as in PbHi7, so the experiment was repeated due to the circumstances that may have led to contamination. For PbHi9 every step was done as carefully as possible using everything that was learned about cross contamination from the previous trials. The distillation was again done without a thermometer, however extreme caution was taken to heat slowly and maintain control over the boiling of the liquid. As well the stir bar worked effectively in this trial. The results of PbHi9 were the

best of the double distillation, indicating that minimizing the contamination between distillations can increase the reduction factor.

Exp-ID	Spike Time	Counts Feed, Mass (counts/hour)	Counts Purified, Mass (counts/hour)	Count Time
PbHi2	3.5 hours	1930 $\pm$ 19.3, 0.0172 g	3237 $\pm$ 32.4, 8.66 g	140 hours
PbHi3-1	3.5 hours	1038 $\pm$ 10.4, 0.0172 g	1535 $\pm$ 15.3, 9.2 g	180 hours
PbHi3-2	3.5 hours	1038 $\pm$ 10.4, 0.0172 g	1353 $\pm$ 13.5, 9.2 g	180 hours
PbHi4	4 hours	2682 $\pm$ 26.8, 0.0172 g	1164 $\pm$ 11.6, 9.44 g	90 hours
PbHi5	4 hours	1284 $\pm$ 12.8, 0.0172 g	96.7 $\pm$ 2.9, 9.44 g	40 hours
PbHi6	4 hours	1951 $\pm$ 19.5, 0.0172 g	107 $\pm$ 3.2, 8.94 g	160 hours
PbHi7-1	4 hours	2311 $\pm$ 23.1, 0.0172 g	1051 $\pm$ 21, 9.02 g	35 hours
PbHi7-2	4 hours	2311 $\pm$ 23.1, 0.0172 g	303 $\pm$ 6.1, 7.6 g	35 hours
PbHi8-1	4.5 hours	3372 $\pm$ 33.7, 0.0172 g	1111 $\pm$ 11.1, 8.35 g	72 hours
PbHi8-2	4.5 hours	3372 $\pm$ 33.7, 0.0172 g	759.7 $\pm$ 15.3, 8.53 g	72 hours
PbHi9-1	3 hours	1990 $\pm$ 19.9, 0.0172 g	355 $\pm$ 2.14, 7.65 g	90 hours
PbHi9-2	3 hours	1990 $\pm$ 19.9, 0.0172 g	188 $\pm$ 5.71, 7.76 g	90 hours

Table 4.22: Raw data from vacuum distillation tests

Exp-ID	Reduction Factor	Efficiency
PbHi2	300 $\pm$ 16	(99.7 $\pm$ 0.017)%
PbHi3-1	360 $\pm$ 18	(99.7 $\pm$ 0.014)%
PbHi3-2	410 $\pm$ 21	(99.8 $\pm$ 0.012)%
PbHi4	1237 $\pm$ 64	(99.9 $\pm$ 0.004)%
PbHi5	7284 $\pm$ 432	(99.99 $\pm$ 0.001)%
PbHi6	9480 $\pm$ 560	(99.99 $\pm$ 0.001)%
PbHi7-1	1152 $\pm$ 63	(99.91 $\pm$ 0.005)%
PbHi7-2	3370 $\pm$ 170	(99.97 $\pm$ 0.002)%
PbHi8-1	1475 $\pm$ 77	(99.93 $\pm$ 0.004)%
PbHi8-2	2220 $\pm$ 113	(99.95 $\pm$ 0.002)%
PbHi9-1	2479 $\pm$ 136	(99.96 $\pm$ 0.002)%
PbHi9-2	4489 $\pm$ 319	(99.98 $\pm$ 0.001)%

Table 4.23: Results from purification tests using the larger spike setup. Results included are from tests using distillation, distillation plus alumina adsorption and double distillation.

## 4.6 Conclusions from Purification Tests

Looking at the results from Tables 4.4, 4.6, 4.8, and 4.10 one sees that the extraction efficiencies are very low for all tests. This led to the conclusion that the lead is not in ionic or metallic form in the LAB. The failure of these two methods to remove the Pb from the LAB meant that more complicated methods were needed to extract the lead.

The adsorption purification tests were successful, yielding extraction efficiencies of over 60 % even in the preliminary testing stages. Using the second spike setup and with a stronger, more consistently spiked LAB samples, the adsorption method yielded even better extraction efficiencies. Three adsorbents were tested: silica gel, HZrO loaded silica gel and aluminum oxide. Based on the results from Tables 4.14 and 4.16 and on consultation with SNO+ radio-chemist Xin Dai, aluminum oxide was chosen as the best adsorbent candidate material. The tests show that aluminum oxide has a high extraction efficiency, greater than 95%, and excellent  $K_d$  values. The tests also show that it reaches equilibrium quickly, maintains its adsorption qualities and the aluminum oxide does not start to desorb quickly, or become exhausted. Overall, the adsorption tests produced promising results and showed that the Pb was most likely in an organic form in the LAB.

The last set of tests are the vacuum distillation tests which gave the best extraction efficiencies of all the methods tried. The extraction efficiencies were so high that they pushed the limits of the original spike's capability and required a stronger spike to achieve more accurate results. Tables 4.20 and 4.23 show the results from all distillation tests. The results from Table 4.20 are only lower limits, and the results from Table 4.23 improve on these results by using a higher concentration spike.

If the lead contamination is in an organic form in the LAB, as supposed, then vacuum distillation works to remove the lead. The main downfall to distillation is that it is expensive to run, with a lot of power needed to boil many tons of LAB and more

power needed to maintain vacuum during the boiling. As a benefit, the distillation method has less intrinsic contamination compared to alumina because all parts can be made with low radioactivity glass, plastic or metal. These bench top purification measurements provide a good indication that the Pb can be effectively removed from the LAB. An even higher reduction factor should be able to be achieved with a large scale set up. The large scale set up will allow for longer heating times to break the organic-Pb bond and should be more effective. Based on the results from these small scale purification tests it is clear that the adsorption and distillation methods yield the most promising results. The method of purification that is most well suited to the SNO+ project is distillation as it yields higher efficiencies and there is no worry about breakthrough or desorption. However, the maximum purification results can be achieved using a combination of distillation and alumina adsorption. This could involve using alumina columns to pre-filter the LAB before distillation. Another idea is adding alumina to the distillation tower and complete both purification methods at the same time. This may not be feasible from an engineering standpoint, but all options should be considered and evaluated to develop the large scale purification scheme for SNO+.

# Chapter 5

## Optical Purity

One of the main requirements of the liquid scintillator is that it must be optically pure in order for the scintillation light to travel uninhibited to the detectors. Extensive radiopurification methods have been investigated and now the most successful methods, adsorption and vacuum distillation need to be studied to determine their affect on the optical purity of the LAB.

Optical measurements were made on a Perkin Elmer Lambda 35 Ultraviolet-visible (UV/VIS) spectrometer. The instrument measures the intensity of the light passing through the sample and determines the absorption of the sample. Samples were placed in 10 cm, 5 cm, and 1 cm cuvettes and measurements were taken of all three lengths. The cuvettes are made of synthetic quartz. The sample is placed in the UV/VIS spectrometer and the spectrometer scans through all wavelengths making measurements in the ultraviolet spectrum from 200 to 400 nm and in the visible spectrum from the 400 to 800 nm. The resulting data is given as an absorbance value for every wavelength value.

The goal of optical purification is to lower the optical absorbance of the liquid so that more light is able to pass freely though and not be obstructed on its way to the detectors. It is especially important that the absorbance be low in the wavelength

region that the detectors are most sensitive.

## 5.1 Adsorption Column

Based on the results of the radiopurification tests, it was determined that the adsorbent which should be tested for optical purification is the aluminum oxide ( $\text{Al}_2\text{O}_3$ ). For the optical purification test, the set up is very different than the radiopurification test. For these tests a small glass column with teflon fittings at the top and bottom is filled with aluminum oxide. For the optical measurements it is important that the column be made of glass and the fittings of glass or teflon to minimize the risk of leaching optical impurities.

The small column can be loaded two possible ways: wet or dry. In dry loading alumina, in its original dry form, is gently poured into the column and wetted with the LAB after the column is loaded. This method proved incredibly time consuming as the LAB was very slow to pass through the dry alumina. In wet loading, the alumina is mixed with LAB prior to loading in the column. Once the alumina is sufficiently wet it is carefully poured into the column. When more LAB is then poured into the column it passes much more easily. In order to ensure that the measurements made are of the purified LAB, the first 50 mL of LAB extracted from the column are set aside, because it is likely that this amount came from the LAB used to wet the alumina. With the wet loading it was found that if a small amount of glass wool was put at the bottom of the column before loading the wet alumina it greatly reduced the amount of alumina particulate that seeped into the sample. This improves optical measurements and makes them more reliable because they are not limited by the "impurities" of the alumina beads. Figure 5.1 shows a schematic of the small column set up, with the glass wool at the bottom, followed by packed in aluminum oxide and then the raw LAB on top waiting to go through the column. It is all collected in an

Erlenmeyer flask.

After the column is loaded, and the first 50 mL set aside, the extraction of purified LAB can begin. The purified samples are collected in multiple 250 mL fractions and separate measurements made. For this small column set up, the rate at which the raw LAB passes through the column is extremely slow, on the order of 100 mL/h. The column was not electronically run, meaning that the LAB needed to be added to the column by hand using a small pipet. If this procedure is adapted to larger scale tests the system would have to be electronically controlled, and a larger column used to increase flow rate.

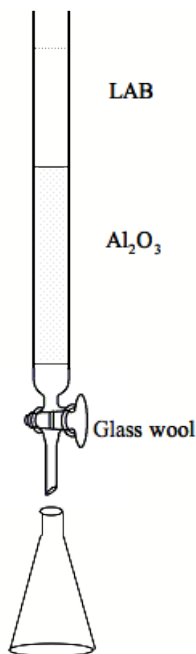


Figure 5.1: Alumina column set up.

The results of optical purification for the different fractions passing through the column are shown in Figure 5.2. It can be seen that the first fraction is considerably more optically pure than the following fractions; however, after the first fraction, the other four are quite close together. The column has maximum purification effect on its first pass through the column, and then there is a small decrease in purification power. Although this result is undesirable, the decrease after the first fraction is not

drastic and the purification power remains almost constant after that point.

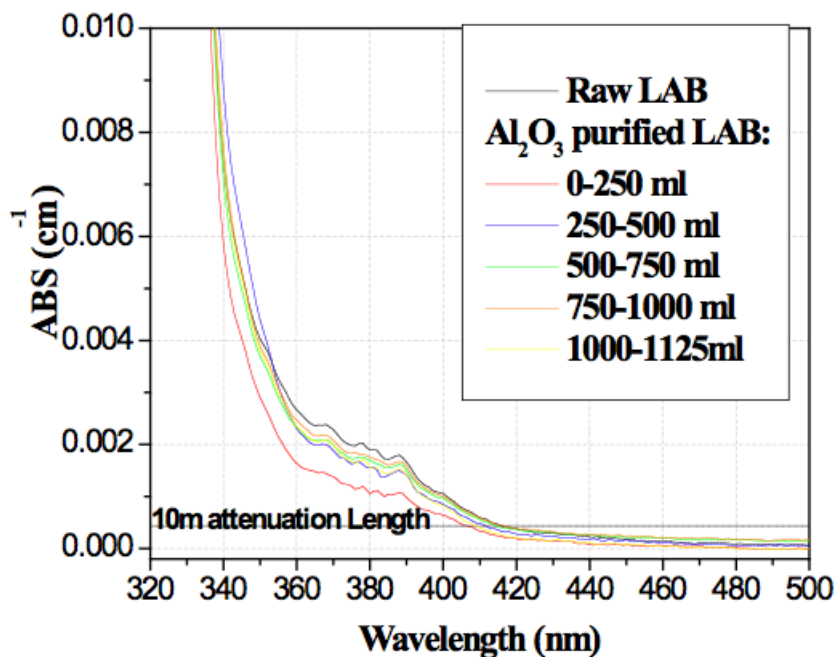


Figure 5.2: Results from optical purification alumina tests.

## 5.2 Other Optical Tests

There were a variety of different optical purification tests tried beyond the simple measurement of fractions. In most situations when adsorption is used for purification there is a point at which the adsorbent becomes exhausted and cannot adsorb more impurities. It is possible to regenerate the adsorbent so that it can continue to be used without replacing it. This process is called regeneration. The alumina that was used in the above measurement was regenerated using hydrochloric acid. The regenerated alumina was then used in a small column as before to determine the success of regeneration and how the optical purity is affected. The results of the regeneration can be seen in Figure 5.3. It is clear in comparison that the regeneration does slightly improve the optical purity from the raw LAB, but it does not fully

regenerate to the quality of the original  $\text{Al}_2\text{O}_3$  purification.

Another variation on the optical purification was to use distilled LAB in the same set up as the radiopurification and purify it a second time using the alumina column. Figure 5.3 shows the results from all the different optical purification tests. It can be seen that overall the double distillation achieves the best optical purification results. There is a slight improvement after putting single distilled LAB through the alumina column, but the change is not significant compared to the results from the double distilled. The result is promising because it means the alumina column is not introducing any new form of optical impurities which would be troublesome if alumina was used in the radiopurification method. The results also show that the regeneration method did not work well and that a larger investigation would have to be done if an alumina column was used for large scale purification in order to figure out the best method to regenerate the alumina. The single distillation and single alumina column pass yield very similar results, however, there is some concern that the alumina column results will deteriorate as the distillation results stay constant as there is nothing to become exhausted in the distillation process.

### 5.3 Optical Purification Conclusions

It is clear from Figure 5.3 that double distillation and the combination of single distillation and alumina purification yield the best results. The benefit of the double distillation is that it is an easier method to implement than the alumina column because it does not become exhausted and does not need regeneration. Also, the optical quality produced by distillation does not deteriorate over time like the alumina column, where the first fraction is considerably better than the following fractions. For optimal optical purity that double distillation should be used, with the possibility of using it in combination with an alumina column. Also of note in Figure 5.3 is that

the single distillation and single  $\text{Al}_2\text{O}_3$  column result in almost the same optical purity.

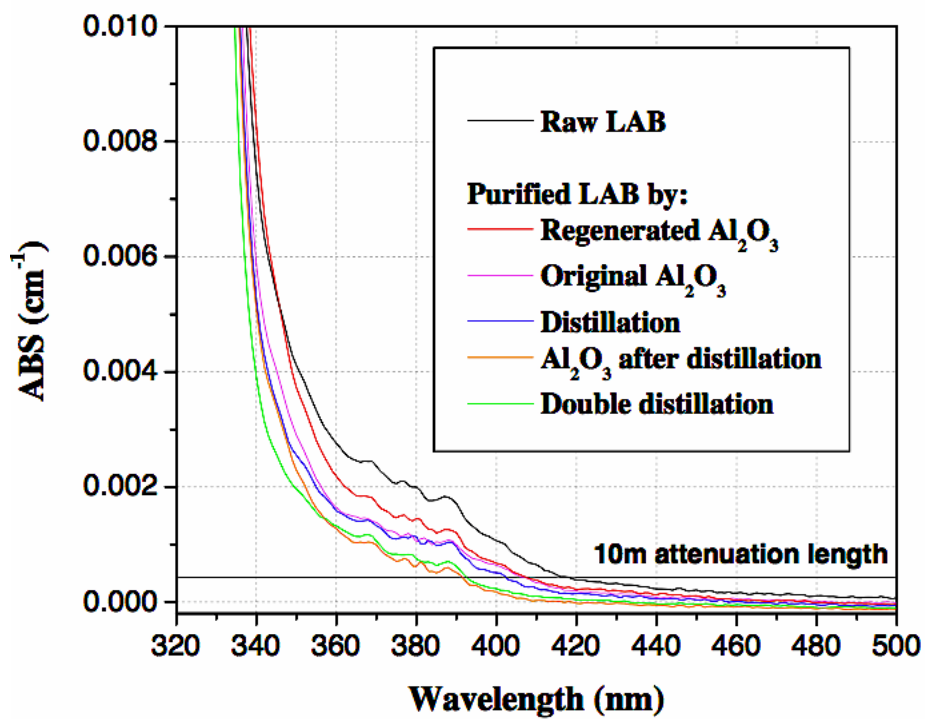


Figure 5.3: Results from all optical purification tests including distillation, double distillation, adsorption with  $\text{Al}_2\text{O}_3$ , regeneration and combination of distillation and adsorption.

# Chapter 6

## Simulation of Background Effects on Signal

Simulations are an important part of an experiment, they are used to accurately estimate (to the best of modeling capabilities) how a system will react to a wide range of conditions that would be impossible to manually impose. This chapter will explore preliminary results from the original code used and information that can be gained by enhancing the simulation code to include more background shapes and signals. As well, constraints using probable equilibrium conditions will be used to determine if simulation results can be improved.

The backgrounds in SNO+ are simulated using a Monte Carlo C++ code. The code used is a standalone code that generates data sets using the energy probability distribution functions (PDFs) that have been calculated using SNOMAN (EGS4) for both signals and backgrounds. EGS4 (Electron Gamma Shower) is a Monte Carlo simulation code that is used for complex geometries to simulate the transport of electrons and photons. SNOMAN stands for SNO Monte Carlo and ANalysis and it is the offline software used to analyze the SNO data and also to do detailed simulation of all backgrounds and signals. SNOMAN can be used for SNO+ because all the

electronics and hardware remain the same and it should be straightforward to adjust for the scintillator target and additional backgrounds [31].

A gaussian energy resolution is applied and then the data is fit using the original PDFs. The input background levels used in the simulations are given in Table 6.1; they are based on KamLAND’s re-purified scintillator goals. All simulations were run using input parameters stated in Table 6.2. The input values are conservative estimations where possible. For example the light output used in the simulation is 400 Nhit/MeV, which corresponds to an energy resolution of 5% at 1 MeV, while the light output in SNO+ will likely be closer to 1200 Nhit/MeV (number of  $\gamma$ /MeV). As well, the live time used is only 1 ktonne-year, but there is the possibility of running for 3 ktonne-year live years, which would greatly improve statistics on the physics values of interest. The alpha quenching factor is the factor by which the efficiency of light emission is reduced by alpha interaction.

<b>Isotope</b>	<b>No. Events (ev./yr/ktonne)</b>	<b>Isotope</b>	<b>No. Events (ev./yr/ktonne)</b>
<sup>238</sup> <b>U</b>	393	<sup>232</sup> <b>Th</b>	1232
<sup>234</sup> <b>Pa</b>	393	<sup>228</sup> <b>Ac</b>	1232
<sup>234</sup> <b>U</b>	393	<sup>228</sup> <b>Th</b>	1232
<sup>230</sup> <b>Th</b>	393	<sup>224</sup> <b>Ra</b>	1232
<sup>226</sup> <b>Ra</b>	393	<sup>220</sup> <b>Rn</b>	1232
<sup>222</sup> <b>Rn</b>	393	<sup>216</sup> <b>Po</b>	1232
<sup>218</sup> <b>Po</b>	393	<sup>212</sup> <b>Po</b>	788
<sup>214</sup> <b>Pb</b>	393	<sup>208</sup> <b>Tl</b>	444
<sup>214</sup> <b>Bi</b>	393	<sup>212</sup> <b>Bi</b>	1232 ( $\beta$ and $\alpha$ )
<sup>214</sup> <b>Po</b>	393	<sup>39</sup> <b>Ar</b>	$\sim 10^3$
<sup>210</sup> <b>Bi</b>	44000	<sup>40</sup> <b>K</b>	$8.1 \times 10^4$
<sup>210</sup> <b>Po</b>	44000	<sup>85</sup> <b>Kr</b>	$3.7 \times 10^4$

Table 6.1: Table of expected internal backgrounds, with values based on KamLAND’s post-purification levels.

## 6.1 Preliminary Code

The first draft of the code to simulate the internal backgrounds in SNO+ was a simplified approach to modeling internal backgrounds. It included seven background shapes:  $^{210}\text{Bi}$ ,  $^{228}\text{Ac}$ ,  $^{214}\text{Bi}$ ,  $^{208}\text{Tl}$ ,  $^{212}\text{Bi}$ ,  $^{234}\text{Pa}$ , and  $^{40}\text{K}$ . These are the  $\beta$  decays with end points above 700 keV. Figure 6.2 shows the simulated energy spectrum using this code for SNO+. As seen from the “Data” box on the plot, the fitted value for the *pep* shape is  $1.269 \times 10^4 \pm 2.973 \times 10^3$ , which is an uncertainty of  $\pm 23.4\%$  on the *pep* measurement. The main cause of the large uncertainty on the *pep* values is that the shape of the  $^{210}\text{Bi}$  curve and the CNO curve are very similar. This causes the fitting code to be unable to distinguish between the two shapes with the result that the code assigns a large uncertainty to both values. This can also be seen in that the value for  $^{210}\text{Bi}$  is  $6.224 \times 10^4 \pm 2.8891 \times 10^4$ , uncertainty value of  $\pm 46.4\%$ . Figure 6.1 shows an example of how the background and signal variables are set up in the preliminary code to simulate the energy spectrum in SNO+.

This inability for the fitting mechanism to clearly distinguish between the  $^{210}\text{Bi}$  and the CNO signal shape requires changes to be made to the code in order for it to be able to discriminate between the two shapes.

Parameter	Value
Livetime	1 ktonne-year
Alpha Quenching Factor	10
Light Output (Nhit/MeV)	400 NHit/MeV
Input Signals (ev/yr/ktonne)	
<i>pep</i>	10834 * livetime
CNO	21900 * livetime
$^7\text{Be}$	199913 * livetime
$^8\text{B}$	1837 * livetime

Table 6.2: Input values used in simulations, including expected experimental parameters and signals.

```

//*****
//Set the average number of the different backgrounds and signals

//number of test data sets to throw
int numtries = 1500;

double livetime = 1.0; //the livetime in years

double numback[10];

numback[0]=1232.*livetime; //Ac228
numback[1]=44000.*livetime; //Bi210
numback[2]=393.*livetime; //Bi214
numback[3]=444.*livetime; //Tl208
numback[4]=22000.*livetime; //K40
numback[5]=393.*livetime; //Pa234
numback[6]=1232.*livetime; //Bi212

double numpep=10834.*livetime; //pep
double numCNO=21900.*livetime; //CNO

```

Figure 6.1: Old code, with only high energy betas, energy threshold of 700 keV.

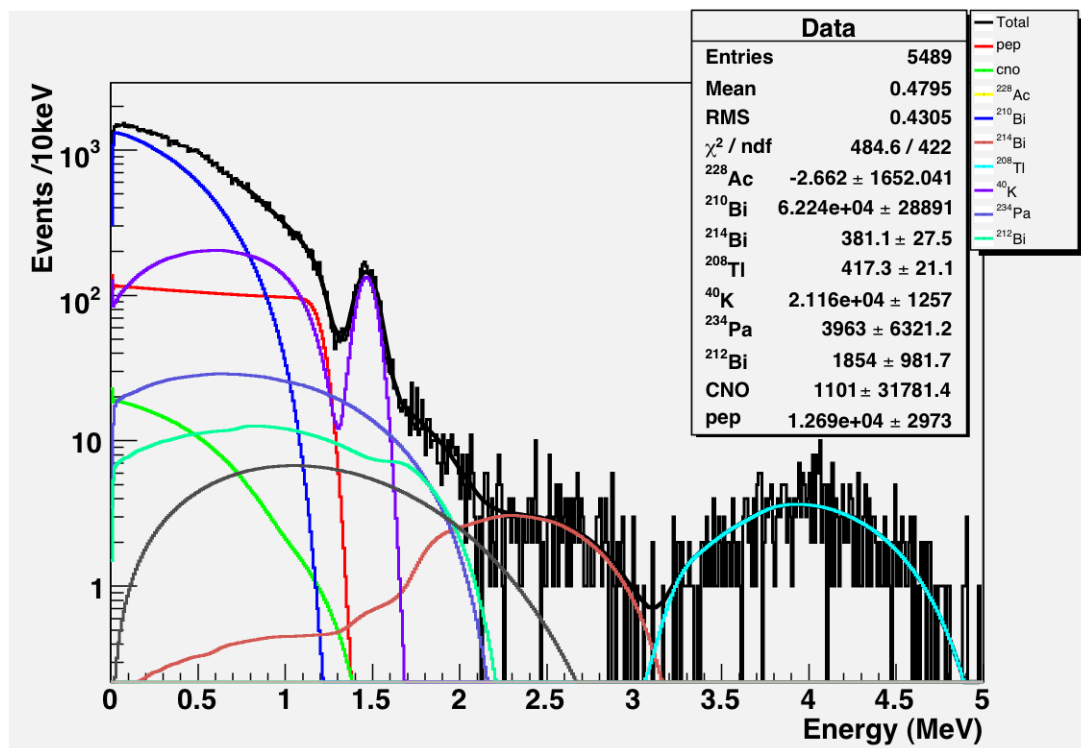


Figure 6.2: Energy spectrum produced using the preliminary code.

### 6.1.1 Enhanced Code: Low energy alphas, equilibrium constraints, ${}^7\text{Be}$ and ${}^8\text{B}$ spectra.

The main problem in the preliminary code was that the fitter part of the program was unable to distinguish between the CNO shape and the  ${}^{210}\text{Bi}$ . One way of trying to fix this problem is to constrain the fitted amount of  ${}^{210}\text{Bi}$  based on secular equilibrium in the decay chain in hopes that the fitter will be able deal with the added shapes from the related equilibrium activity more easily. The first step was including the  ${}^{210}\text{Po}$  alpha event and the low energy events above 400 keV. To increase the discriminating power of the fitter, and in turn lower the uncertainty on key values of interest, many of the background shapes were constrained by equilibrium groupings. Figures 6.3(a) and 6.3(b) show the thorium and uranium chains, respectively, where the different colours indicate the different equilibrium groupings. The equilibrium breaks were decided by length of half life; it is reasonable to assume that isotopes with short half lives will be in secular equilibrium.

In the code, the isotopes in equilibrium (Figure 6.3) are constrained to have the same decay rate. Figure 6.4 shows a similar part of the code as in the previous section, however this time there are many more backgrounds included and it is clearly seen how some isotopes are linked to each other, and how branching ratios are accounted for in the code.

The last improvement on the code was to include the  ${}^7\text{Be}$  and  ${}^8\text{B}$  neutrino shapes as additional backgrounds. This addition helps to complete the entire energy spectrum that SNO+ is likely to see during its solar phase running. The  ${}^7\text{Be}$  is a high-statistics background, so its addition added slightly to the uncertainty of the *pep* value ( $\sim 0.5\%$ ); however, since this shape will be present in the actual data set it is important to include it in the modeling to develop the most complete simulation possible.

The final energy spectrum can be seen in Figure 6.5. Most of the low energy alphas exist in the energy region about 0.5 MeV make the spectrum look quite jumbled

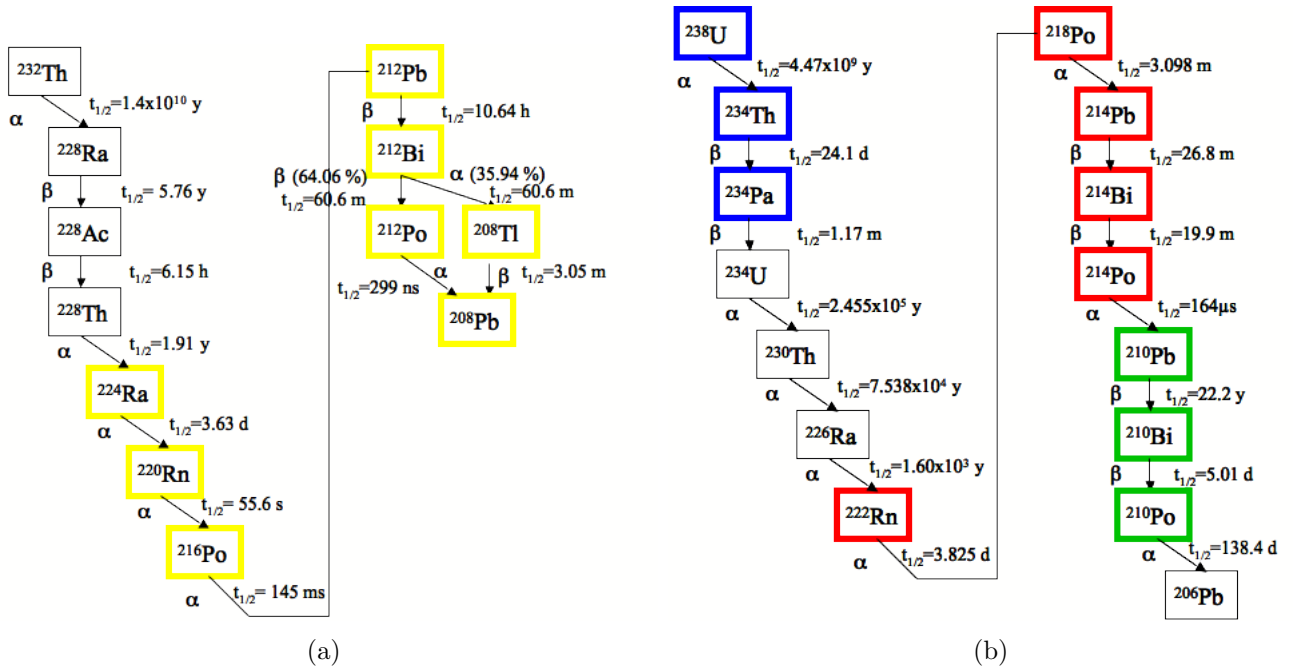


Figure 6.3: (a) The thorium chain with colours indicating decay events in equilibrium. (b) The uranium chain equilibrium with colours indicating decay events in equilibrium.

and complicated. Figure 6.6 shows a zoomed in area of the low energy region. Although the energy spectrum looks much more complicated than it did originally, the additional constraints in the fit improve the *pep* uncertainty from  $\pm 23.4\%$  to  $\pm 8.55\%$ . If extreme care is taken to not introduce radon into the detector environment and if the optimal light output (1200 Nhit/MeV) and live time (3 ktonne years) are reached, the value can decrease to  $\pm 3.2\%$ .

```

//*****
//Set the average number of the different backgrounds and
signals
int numtries = 5000;

double livetime = 1.0; //the livetime in years

double numback[30];
TVirtualFitter::Fitter(0, npts);

numback[0]=1232.*livetime; //Ac228 - beta
numback[1]=44000.*livetime; //Bi210 - beta
numback[2]=393.*livetime; //Bi214 - beta
numback[3]=37000.*livetime; //Kr85 - beta
numback[4]=22000.*livetime; //K40 - beta
numback[5]=393.*livetime; //Pa234 - beta
numback[6]=1232.*livetime; //Bi212 - beta
numback[7]=393.*livetime; //U234 - alpha
numback[8]=393.*livetime; //Th230 - alpha
numback[9]=393.*livetime; //Ra226 - alpha
numback[10]=1232.*livetime; //Th232 - alpha
numback[11]=1232.*livetime; //Th228 - alpha
numback[12]=1000.*livetime; //Ar39 - beta

//these backgrounds are in equilibrium with other fitted
backgrounds and are hence not individually fitted.

numback[18]=numback[6]*(1./0.64)*0.36; //Bi212 - alpha
numback[19]=numback[6]*(1./0.64); //Ra224 - alpha
numback[20]=numback[6]*(1./0.64); //Rn220 - alpha
numback[21]=numback[6]*(1./0.64); //Po216 - alpha
numback[22]=numback[6]; //Po212 - alpha
numback[23]=numback[6]*(1./0.64)*0.36; //Tl208 - beta
numback[24]=numback[2]; //Rn222 - alpha
numback[25]=numback[2]; //Po214 - alpha
numback[26]=numback[2]; //Pb214 - beta
numback[27]=numback[2]; //Po218 - alpha
numback[28]=numback[5]; //U238 - alpha
numback[29]=numback[1]; //Po210 - alpha

double numpep=10834.*livetime; //pep 10834
double numCNO=21900.*livetime; //CNO 21900

```

Figure 6.4: New code, with addition of low energy alphas, energy threshold of 400 keV, and equilibrium used to constraint in fit.

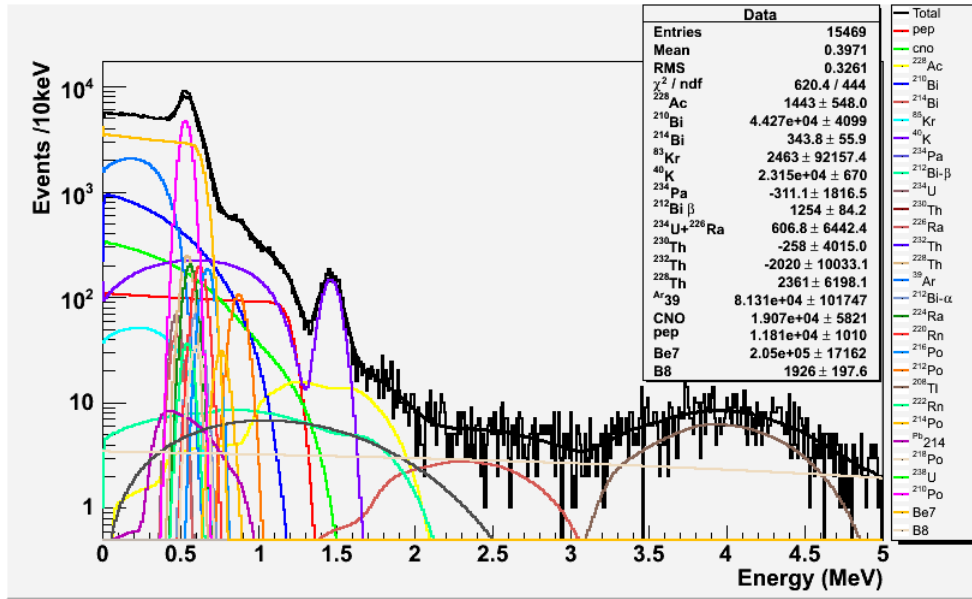


Figure 6.5: Complete energy spectrum including all low energy alphas above 400 keV and equilibrium constraints and <sup>7</sup>B and <sup>8</sup>Be neutrino signals.

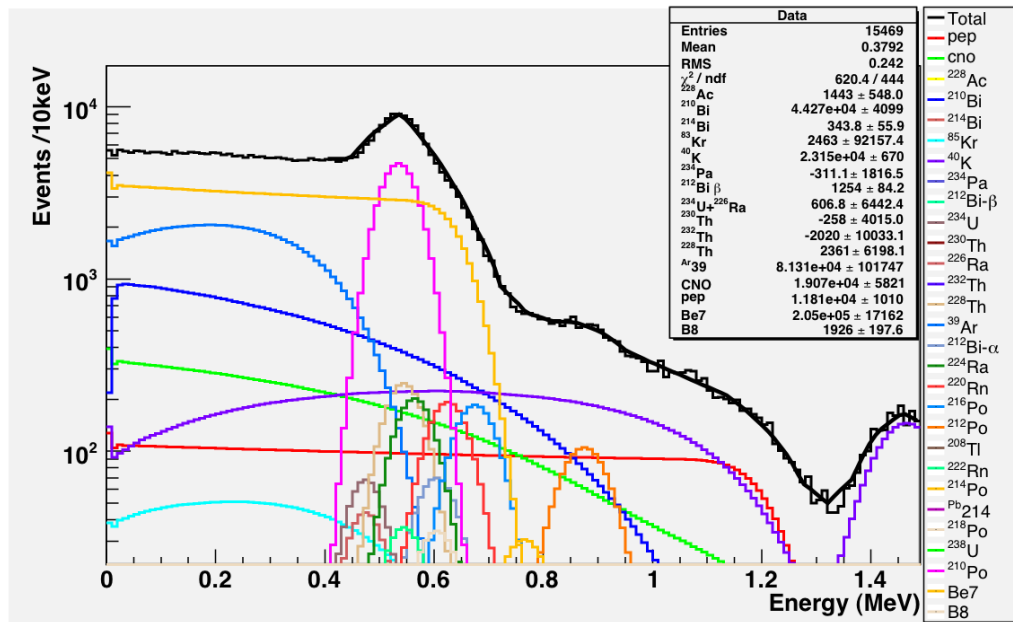


Figure 6.6: Similar spectrum as Figure 6.5 with an expanded low energy region 0-1.5 MeV

## 6.2 Sensitivity Studies

The physics objectives will be greatly affected by internal backgrounds in the detector. It is important to figure out exactly how sensitive the uncertainties on the physics of interest are to fluctuation in and constraints on background levels. The sensitivity indicator used in the following studies is the uncertainty of the *pep* measurement, as it is one of the key measurements that will be made in the solar phase of SNO+. The sensitivity measurements have been split into four main groups of contaminants including the thorium chain, the uranium chain, the noble gases argon and krypton, and potassium.

In Figure 6.7, the sensitivity of fractional *pep* uncertainty with respect to varying values of the thorium chain is shown. Background sources included in the thorium chain are  $^{228}\text{Ac}$ ,  $^{228}\text{Th}$ ,  $^{224}\text{Ra}$ ,  $^{220}\text{Rn}$ ,  $^{216}\text{Po}$ ,  $^{212}\text{Bi}$ ,  $^{212}\text{Po}$ ,  $^{208}\text{Tl}$ , and  $^{232}\text{Th}$ . In Figure 6.7(a), the number of events is varied up to 10x the values in Table 6.1. Figure 6.7(b) shows the number of events up to 100x the tabulated value. It can be seen from both figures that the *pep* uncertainty is sensitive to fluctuations in the thorium chain levels.

The uranium chain is the next background investigated. This task is a little more complicated because  $^{210}\text{Bi}$  and  $^{210}\text{Po}$  can be out of equilibrium with the rest of the uranium chain, and their increased levels pose serious problems if they are not understood properly. In Figure 6.8, there are plots of the uranium chain including elevated levels of  $^{210}\text{Bi}$  and  $^{210}\text{Po}$  (Figures 6.8(c) and 6.8(d)) and plots with those troublesome isotopes at equilibrium with the rest of the uranium chain (Figures 6.8(a) and 6.8(b)). Figure 6.8(a) shows 10x the tabulated levels and Figure 6.8(b) shows 100x. Clearly the *pep* uncertainty becomes larger with increased event number, but at up to 5x the level it does not increase greatly, only from  $\pm 8.5\%$  at the zero level to  $\pm 9.5\%$  at the 5x level. However, when  $^{210}\text{Bi}$  and  $^{210}\text{Po}$  are included in the simulation at 10x (Figure 6.8(c)) and 100x (Figure 6.8(d)) then the *pep* uncertainty becomes

much more sensitive to fluctuations in the event level. The x-axis on the plots that include  $^{210}\text{Bi}$  and  $^{210}\text{Po}$  out of equilibrium are significantly larger in event number to account for 10x/100x the  $^{210}\text{Bi}$  and  $^{210}\text{Po}$  target value (44000), although the other chain value continue to be just 10x/100x their target value (393). With  $^{210}\text{Bi}$  and  $^{210}\text{Po}$  included in the plots at even 5x the tabulated value the uncertainty is  $\pm 10.3\%$  and at 100x the level it is  $\pm 30\%$ .

There is some danger of contaminants  $^{39}\text{Ar}$  and  $^{85}\text{Kr}$  affecting the *pep* uncertainty levels. Figures 6.9(a) and 6.9(b) show plots of *pep* uncertainty for 10x and 100x the tabulated values. The uncertainty levels are quite stable for even 10x the tabulated values and it is at about 20x that there starts to be a significant change.

Lastly,  $^{40}\text{K}$  will definitely be a problem if it contaminates the detector. As seen in Figure 6.10, 6.10(a) is 10x the tabulated value and 6.10(b) is 100x. The slope of both graphs is quite steep, showing that the *pep* uncertainty is fairly sensitive to the  $^{40}\text{K}$  level. Even at 10x the KamLAND background the uncertainty is over 30%. The uncertainty fluctuation and statistics dominate in the 100x plot indicating it would be nearly impossible to make a measurement if  $^{40}\text{K}$  cannot be kept at the target level.

These sensitivity studies show it is imperative to purify the scintillator to the highest level, especially when it comes to  $^{210}\text{Bi}$  and  $^{210}\text{Po}$  and  $^{40}\text{K}$ .

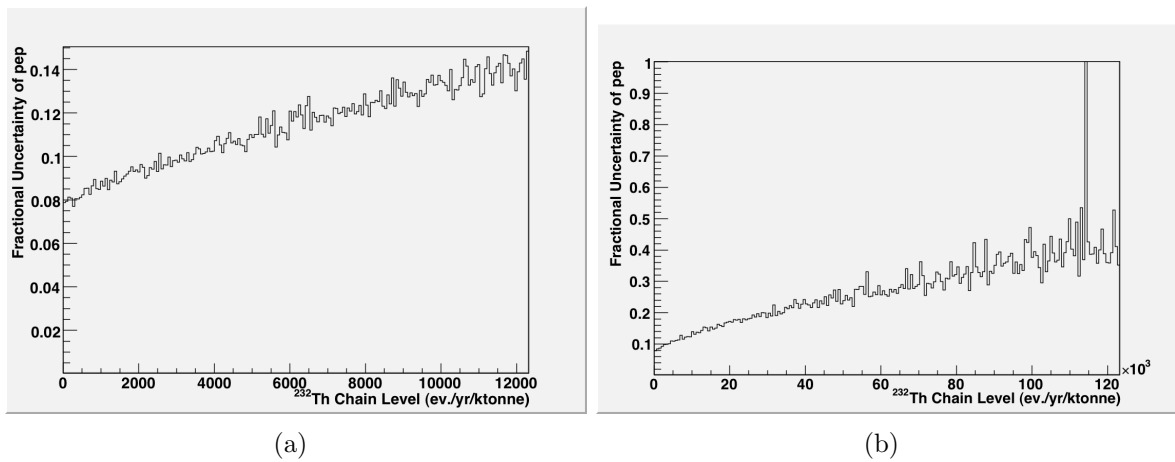


Figure 6.7: (a) The thorium chain event levels 10x higher than the KamLAND re-purified value. (b) The thorium chain event levels 100x higher than the KamLAND re-purified value.

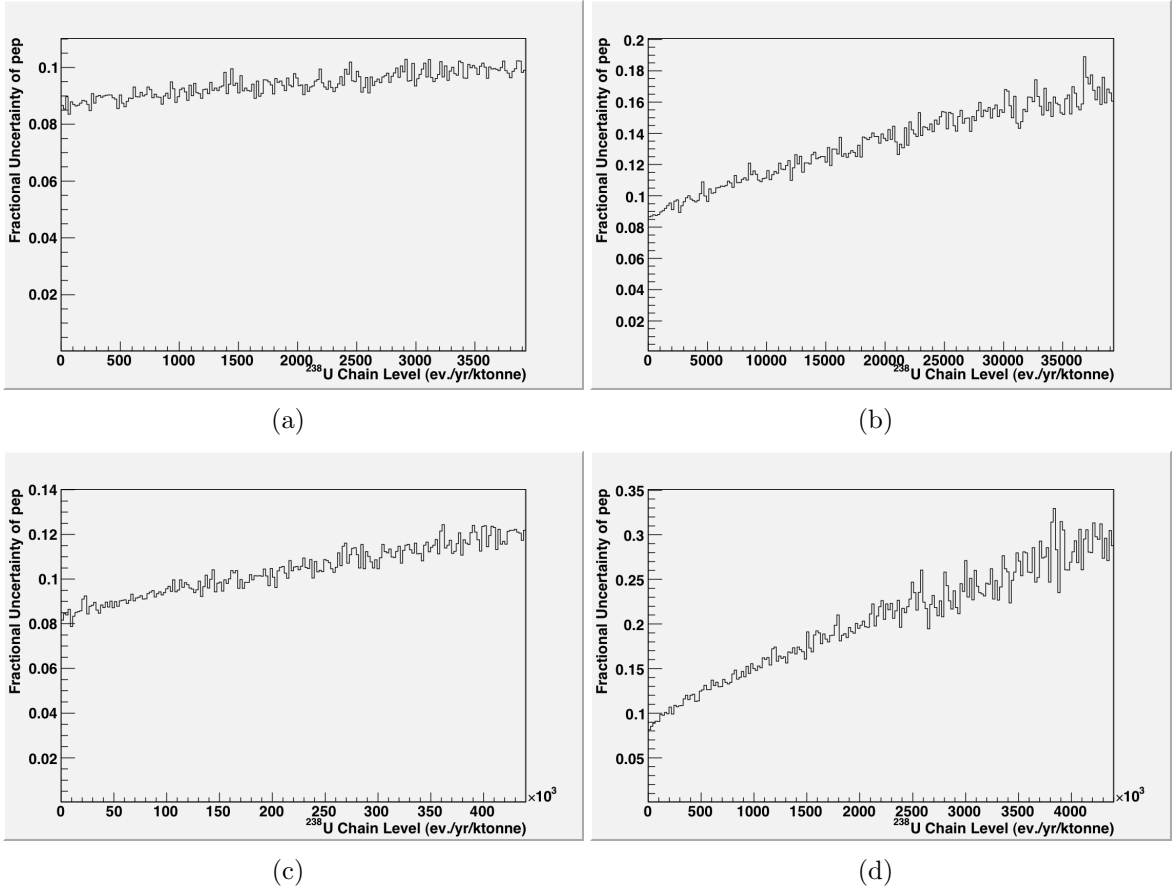


Figure 6.8: (a) Uranium chain event levels 10x KamLAND re-purified without  $^{210}\text{Bi}$  and  $^{210}\text{Po}$  levels held fixed at values given in Table 6.1 (b) Uranium chain event levels 100x KamLAND values without  $^{210}\text{Bi}$  and  $^{210}\text{Po}$  levels fixed. (c) Uranium chain event levels including  $^{210}\text{Bi}$  and  $^{210}\text{Po}$  levels to vary 10x KamLAND re-purified values. (d) Uranium chain event levels including  $^{210}\text{Bi}$  and  $^{210}\text{Po}$  levels varied up to 100x KamLAND re-purified values.

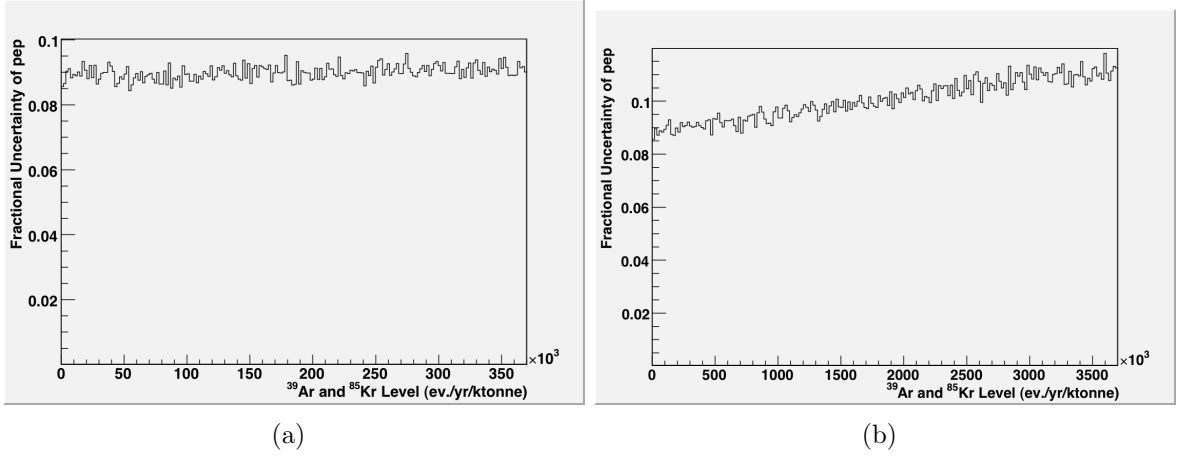


Figure 6.9: (a) The gases <sup>39</sup>Ar and <sup>85</sup>Kr with event levels at 10x the KamLAND re-purified. (b) The gases <sup>39</sup>Ar and <sup>85</sup>Kr with levels at 100x the KamLAND level.

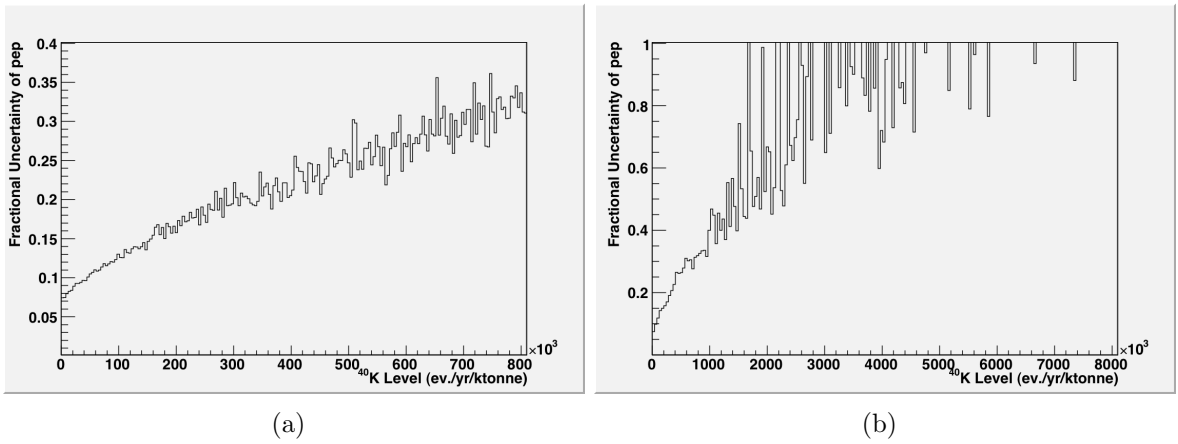


Figure 6.10: (a) <sup>40</sup>K event levels at 10x the KamLAND re-purified. (b) <sup>40</sup>K event level at 100x the KamLAND level.

## 6.3 Constraining lead via bismuth and polonium

$^{210}\text{Po}$  is a daughter of  $^{210}\text{Bi}$  which is a daughter of the problem isotope  $^{210}\text{Pb}$ . The  $^{210}\text{Pb}$  endpoint energy from beta decay is 17 keV, which is too low in energy to be included in the current scope of the simulation (threshold 400 keV). However, the  $^{210}\text{Bi}$  is in equilibrium with the  $^{210}\text{Pb}$  so it is a good indicator of  $^{210}\text{Pb}$  background levels. If  $^{210}\text{Po}$  is in equilibrium with  $^{210}\text{Bi}$  (and consequently  $^{210}\text{Pb}$ ) then its sharp alpha peak is a good way to constrain the  $^{210}\text{Bi}$  in the fits of the energy spectrum. There is a possibility however that the  $^{210}\text{Po}$  will not be in equilibrium with the  $^{210}\text{Bi}$  and  $^{210}\text{Pb}$  if there is a mechanism for it to accumulate on the walls of the acrylic vessel. It is important to determine how breaking of this equilibrium would affect the fit, and in turn the uncertainty on the physics of interest, the *pep* signal.

### 6.3.1 Results of $^{210}\text{Po}$ Constraint

In order to simulate the two possible situations, two variations of the enhanced code are used. The first code, where equilibrium is assumed, is very similar to the normal enhanced code in which the  $^{210}\text{Bi}$  is constrained by the  $^{210}\text{Po}$  alpha. The second code, where an equilibrium breaking is assumed, allows  $^{210}\text{Bi}$  and  $^{210}\text{Po}$  to float freely in the fit, and are in no way constrained to each other. As in the sensitivity studies the comparison of the two options will be reflected in how the constraint or nonconstraint affects the uncertainty level of the *pep* signal.

Figure 6.11 plots the results of the simulations: 6.11(a) is the plot of the *pep* uncertainty with the  $^{210}\text{Bi}$  constrained by the  $^{210}\text{Po}$  alpha, and 6.11(b) is the plot where  $^{210}\text{Bi}$  is unconstrained. Both plots give a range of the event per year per kilotonne of  $^{210}\text{Bi}$  and  $^{210}\text{Po}$ , from zero to ten times the tabulated value (0-440000). It is clear from this figure that the constrained  $^{210}\text{Bi}$  yields an uncertainty considerably lower than the unconstrained  $^{210}\text{Bi}$ . On the constrained plot (Figure 6.11(a)) the uncertainty

of *pep* gradually increases from approximately  $\pm 8\%$  to  $\pm 12\%$ . The unconstrained plot (Figure 6.11(b)) of the *pep* uncertainty shows more statistical fluctuations and has a consistent uncertainty of approximately  $\pm 27\%$  over the entire range of events. At this level of uncertainty, any measurement of *pep* signal may not be scientifically significant.

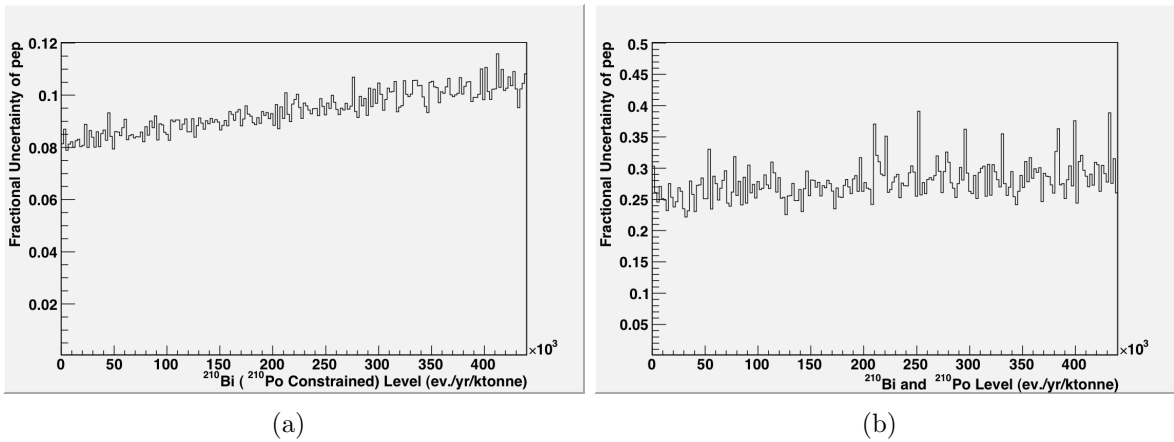


Figure 6.11: (a) Effect of  $^{210}\text{Bi}$  level on the uncertainty of *pep*, assuming that the  $^{210}\text{Po}$  alpha can be used to constrain the  $^{210}\text{Bi}$  (b) Effect of  $^{210}\text{Bi}$  level on the uncertainty of *pep*, assuming that the  $^{210}\text{Po}$  alpha can not be used to constrain the  $^{210}\text{Bi}$ .

The same plots were repeated for the simulation running for three live time years and the results shown in Figure 6.12. Here 6.12(a) is a plot of the increasing  $^{210}\text{Bi}$  level with the constraint of  $^{210}\text{Po}$  and 6.12(b) is a plot of the unconstrained  $^{210}\text{Bi}$  and  $^{210}\text{Po}$  level. As before the constrained  $^{210}\text{Bi}$  yields a much lower uncertainty on the *pep* signal at  $\pm 5\% - \pm 6\%$  and the unconstrained  $^{210}\text{Bi}$  gives a *pep* uncertainty of  $\pm 14\%$ . This is a fairly large improvement from the one year live time results, but it is probably still too large to make a significant measurement. However, if the unconstrained is run with the optimal input values (three live time years, order of ten lower  $^{210}\text{Bi}$  and  $^{210}\text{Po}$  and  $^{40}\text{K}$ , and energy resolution of 1200 nHit/MeV) the results improve to  $\pm 8.5\%$ .

It is clear from the results that it is very important that the  $^{210}\text{Bi}$  be constrained by the  $^{210}\text{Po}$ . The results show that the level of the  $^{210}\text{Bi}$  is less important than how

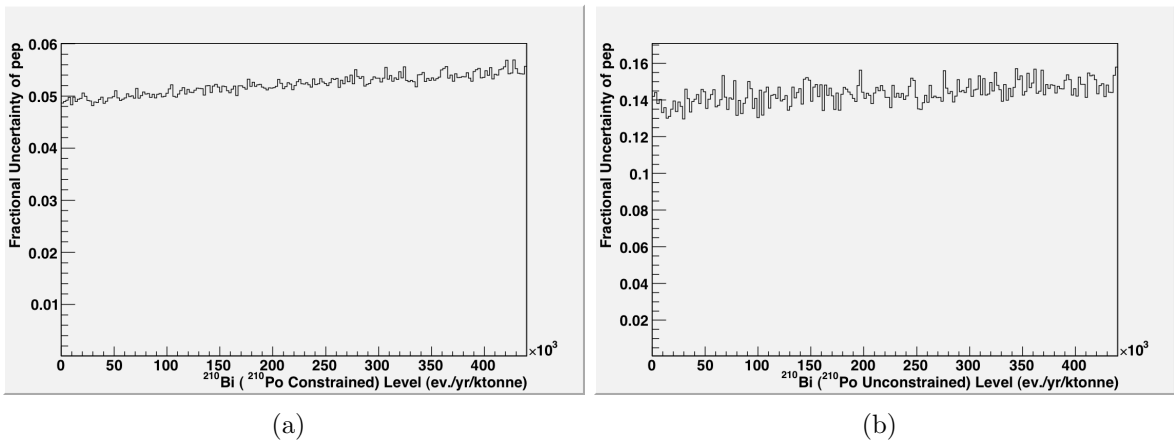


Figure 6.12: (a) Livetime = 3 years. Effect of  $^{210}\text{Bi}$  level on the uncertainty of pep, assuming that the  $^{210}\text{Po}$  alpha can be used to constrain the  $^{210}\text{Bi}$ . (b) Effect of  $^{210}\text{Bi}$  level on the uncertainty of pep, assuming that the  $^{210}\text{Po}$  alpha can not be used to constrain the  $^{210}\text{Bi}$ .

well it is constrained.

# Chapter 7

## Summary and Conclusion

The results from the purification experiments and background level simulations have been combined to characterize the purification goals for the liquid scintillator to be used in SNO+. Using varying purification techniques, radiopurity and optical purity of the liquid scintillator was investigated. The radiopurification was designed to remove lead from the scintillator and the optical purity was to decrease absorption of light in the scintillator.

The radiopurification techniques investigated were water and acid extraction, adsorption using silica gel, hydrous zirconium oxide loaded silica gel and aluminum oxide and vacuum distillation. Preliminary tests were designed to determine the state the lead in the liquid scintillator: ionic, metallic or organic. The water and acid extraction techniques failed to remove the majority of the lead from the scintillator suggesting the lead was most likely not in a ionic or metallic state. Both adsorption and distillation were successful in removing the lead from the scintillator; both methods would be capable of removing lead in an organic state in the scintillator.

Adsorption tests concluded that aluminum oxide was the best adsorbent for this purification task. The aluminum oxide was not easily exhausted and did not readily desorb. The aluminum oxide was able to remove lead with high efficiency and high

---

distribution coefficient, but this method alone was not able to purify the scintillator to the same level vacuum.

Vacuum distillation successfully demonstrated the ability to purify LAB with a reduction of 5000 with double distillation and a reduction factor of approximately 10000 with the combination of distillation and  $\text{Al}_2\text{O}_3$  adsorption. The results from this research lay the ground work to develop the large scale purification system for SNO+. The optical purity of the LAB was improved by both vacuum distillation and adsorption using  $\text{Al}_2\text{O}_3$ .

The simulations demonstrated the need to minimize internal radioactive isotopes in the SNO+ detector. The results from the simulation studies indicate that it is crucial to minimize thorium and uranium chain isotopes, with emphasis on daughter isotopes of  $^{220}\text{Rn}$ :  $^{210}\text{Bi}$  (and  $^{210}\text{Pb}$ ). The studies also suggest the necessity to constrain the  $^{210}\text{Bi}$  level, if possible, by the  $^{210}\text{Po}$  alpha peak. If the  $^{210}\text{Bi}$  cannot be constrained this way it will be imperative to develop another method to constrain the amount of  $^{210}\text{Bi}$ . The simulations indicate that krypton and argon will start to affect the *pep* uncertainty levels if they are at 20 times the KamLAND re-purified level. Lastly, the simulations show that the *pep* uncertainty level is extremely sensitive to  $^{40}\text{K}$  levels and that it is necessary for SNO+ to achieve levels at or lower than KamLAND's projected re-purified level.

The results from this research demonstrate the ability to purify the liquid scintillator for SNO+ by a factor of almost 10000 with an efficiency of 99.99%. The results give preliminary information about the course of action that will have to be taken in order to purify the liquid scintillator at a large scale. The simulations demonstrate the necessity to achieve KamLAND's re-purified background levels and if possible achieve lower levels to reduce the uncertainty on the *pep* measurement. An accurate measurement of the *pep* neutrino flux would be able to test the solar models. A low uncertainty on the *pep* measurement will allow SNO+ to probe new physics including

the vacuum-matter transition region of solar neutrino survival probability as well as the possibility to make a precise measurement of the vacuum mixing angle and a measurement of the  $\Delta m^2$  parameter.

# Bibliography

- [1] Jr. C.L. Cowan and F. Reines et al. Detection of the free neutrino: A confirmation. *Science*, 124:103, 1956.
- [2] Carlo Giunti and Chung W. Kim. *Fundamentals of Neutrino Physics and Astrophysics*. Oxford University Press, 2007.
- [3] W.-M.Yao and et al. (Particle Data Group). The review of particle physics. *Journal of Physics G: Nuclear and Particle Physics*, (2006) and 2007 partial update for the 2008 edition.
- [4] John N. Bahcall, Aldo M. Serenelli, and Sarbani Basu. New solar opacities, abundances, helioseismology, and neutrino fluxes. *The Astrophysical Journal Letters*, 621:85–88, March 2005.
- [5] John N. Bahcall and Aldo M. Serenelli. How do uncertainties in the surface chemical composition of the sun affect the predicted solar neutrino fluxes. *The Astrophysical Journal*, 626(1):530–542, 2005.
- [6] John N. Bahcall and Carlos Pena-Garay. A road map to solar neutrino fluxes, neutrino oscillation parameters, and tests for new physics. *Journal of High Energy Physics*, 0311:004, 2003.
- [7] H. A. Bethe. Energy production in stars. *Physical Review*, 55:434–456, March 1939.

- [8] John N. Bahcall, M.C. Gonzalez-Garcia, and Carlos Pena-Garay. Does the sun shine by pp or CNO fusion reactions? *Physical Review Letters*, 90(13):131301(1–4), April 2003.
- [9] John N. Bahcall and Carlos Pena-Garay. Solar models and solar neutrino oscillations. *New Journal of Physics*, 6, 2004.
- [10] John N. Bahcall, Walter F. Huebner, Stephen H. Lubow, Peter D. Parker, and Roger K. Ulrich. Standard solar models and uncertainties in predicted capture rates of solar neutrinos. *Reviews of Modern Physics*, 54(3):767–799, 1982.
- [11] John N. Bahcall and M.H. Pinsonneault. Standard solar models, with and without helium diffusion, and the solar neutrino problem. *Reviews of Modern Physics*, 64(4):885 – 926, 1992.
- [12] John N. Bahcall and M.H. Pinsonneault. Solar models with helium and heavy-element diffusion. *Reviews of Modern Physics*, 67(4):781 – 808, 1995.
- [13] John N. Bahcall, Sarbani Basu, and M.H. Pinsonneault. How uncertain are solar neutrino predictions? *Physics Letters B*, 433:1–8, 1998.
- [14] John N. Bahcall, M.H. Pinsonneault, and Sarbani Basu. Solar models: current epoch and time dependences, neutrinos, and helioseismological properties. *The Astrophysical Journal*, 555(2):990–1012, 2001.
- [15] John N. Bahcall and M.H. Pinsonneault. What do we (not) know theoretically about solar neutrino fluxes? *Physical Review Letters*, 92(12), 2004.
- [16] Carlos Allende Prieto and David L. Lambert. A reappraisal of the solar photospheric C/O ratio. *The Astrophysical Journal*, 573(2):L137–L140, July 2002.
- [17] P. C. de Holanda and A. Yu. Smirnov. Homestake result, sterile neutrinos, and low energy solar neutrino experiments. *Physical Review D*, 69:113002, 2004.

- [18] Bruce T. Cleveland, Timothy Daily, R. Davis Jr, James R. Distel, Kenneth Lande, C.K. Lee, and Paul S. Wildenhain. Measurement of the solar electron neutrino flux with the homestake chlorine detector. *The Astrophysical Journal*, 496:505–526, 1998.
- [19] Raymond Davis Jr. Solar neutrinos. II. experimental. *Physical Review Letters*, 12(11):303–305, 1964.
- [20] C. Cattadoria, N. Ferrarib, and L. Pandolab. Results from radiochemical experiments with main emphasis on the gallium ones. *Nuclear Physics B (Proc. Suppl.)*, 143:3–12, 2005.
- [21] W. Hampel, J. Handt, and G. Heusser. GALLEX solar neutrino observations: Results for GALLEX IV. *Physical Review B*, 447(127):133, 1999.
- [22] M. Altmann, M. Balata, and P. Belli. Complete results for five years of GNO solar neutrino observations. *Physics Letters B*, 616:174–190, 2005.
- [23] J.N. Abdurashitov, V.N. Gavrin, and S.V. Girin. Measurement of the solar neutrino capture rate with gallium metal. *Physical Review C*, 60, 1999.
- [24] J. N. Abdurashitov, E. P. Veretenkin, and V. M. Vermul. Solar neutrino flux measurements by the soviet–american gallium experiment (SAGE) for half the 22-year solar cycle. *Journal of Experimental and Theoretical Physics*, 95(2):181–193, 2002.
- [25] Lawrence R. Sulak. Massive Cherenkov neutrino facilities...their evolution, their future: Twenty-five years at these International Neutrino Conferences. *Nuclear Physics B (Proc. Suppl.)*, 143:317–326, 2005.
- [26] K.S. Hirata and T. Kajita. Observation in the kamiokande-II detector of the neutrino burst from supernova SN1987a. *Physical Review D*, 38(2):488, 1988.

- [27] Tadao Mitsui. Solar neutrino results. *Nuclear Physics B (Proc. Suppl.)*, 149(13-17), 2005.
- [28] Y. Fukuda, T. Hayakawa, and K. Inoue. Solar neutrino data covering solar cycle 22. *Physical Review Letters*, 77(9):1683–1686, 1996.
- [29] S. Fukuda, Y. Fukuda, and M. Ishitsuka. Solar  $^8\text{B}$  and hep neutrino measurements from 1258 days of Super-KamiokaNDE data. *Physical Review Letters*, 86(25), 2001.
- [30] S. Fukuda et al. Determination of solar neutrino oscillation parameters using 1496 days of Super-Kamiokande-I data. *Physical Review B*, 539:179–187, 2002.
- [31] J. Boger and R.L. Hahn et al. The Sudbury Neutrino Observatory. *Nuclear Instruments and Methods in Physics Research A*, 449:172–207, 2000.
- [32] S. N. Ahmed and A. E. Antyhony et al. Measurement of total active  $^8\text{B}$  solar neutrino flux at the Sudbury Neutrino Observatory with enhanced neutral current sensitivity. *Physical Review Letters*, 92(18), 2004.
- [33] Q. R. Ahmad and R. C. Allen et al. Measurement of the rate of  $\nu_e + d \rightarrow p + p + e^-$  interactions produced by  $^8\text{B}$  solar neutrinos at the Sudbury Neutrino Observatory. *Physical Review Letters*, 87(7), 2001.
- [34] B. Aharmim and Q. R. Ahmad et al. Determination of the  $\nu_e$  and total  $^8\text{B}$  solar neutrino fluxes using the Sudbury Neutrino Observatory phase 1 data set. *Physical Review C*, 75, 2007.
- [35] Q. R. Ahmad et al. Direct evidence for neutrino flavor transformation from neutral-current interactions in the Sudbury Neutrino Observatory. *Physical Review Letters*, 89(1), 2002.

- [36] T. Shutt for the BOREXINO Collaboration. BOREXINO: a status report. *Nuclear Physics B (Proc. Suppl.)*, 110:323–325, 2002.
- [37] Gioacchino Ranucci. BOREXINO. *Nuclear Physics B (Proc. Suppl.)*, 168:111–114, 2007.
- [38] G. Alimonti et al. (BOREXINO Collaboration). BOREXINO. Solar neutrino physics. *LNGS Annual Report 1998*, 1998.
- [39] F.P. Calaprice (for the BOREXINO Collaboration). The BOREXINO experiment: A status report. *Proc. of Sixth International Workshop on Topics in Astroparticle and Underground Physics (TAUP99)*, 1999.
- [40] G. Alimonti et al. A large-scale low background liquid scintillation detector: the counting test facility at Gran Sasso. *Nuclear Instruments and Methods in Physics Research A*, 406(411-426), 1998.
- [41] G. Alimonti et al. Light propagation in a large volume liquid scintillator. *Nuclear Instruments and Methods in Physics Research A*, 440:360–371, 2000.
- [42] G. Alimonti et al. Measurement of the  $^{14}\text{C}$  abundance in a low-background liquid scintillator. *Physical Review B*, 422:349–358, 1998.
- [43] C. Arpesella. First real time detection of  $^7\text{Be}$  solar neutrinos by BOREXINO. *Physics Letters B*, Article in Press, 2007.
- [44] J. Busenitz. The KamLAND experiment. *International Journal of Modern Physics A*, 16:742–744, 2001.
- [45] Junpei Shirai (representing the KamLAND Collaboration). Start of KamLAND. *Nuclear Physics B (Proc. Suppl.)*, 118(15-22), 2003.

- [46] K. Eguchi et al. (KamLAND Collaboration). First results from KamLAND: Evidence for reactor anti-neutrino disappearance. *Physical Review Letters*, 90:021802, 2003.
- [47] T. Araki et al. Experimental investigation of geologically produced antineutrinos with KamLAND. *Nature*, 436:499–503, 2005.
- [48] T. Araki. Measurement of neutrino oscillation with KamLAND: Evidence of spectral distortion. *Physical Review Letters*, 94:081801, March 2005.
- [49] Mark Chen and SNO+ Collaboration. A proposal for the SNO+ experiment at SNOLAB. SNO+ Internal Documents, August 2007.
- [50] Ben Lucht. Removal of implanted radon daughters from acrylic. SNO+ Internal Documents.
- [51] Aksel Hallin. Calculation of recoil for imbedding of radon daughters into and out of acrylic. SNO+ Internal Documents.
- [52] Chris Jillings and Ian Lawson. Backgrounds from lead plateout on acrylic. SNO+ Internal Documents.
- [53] John N. Bahcall, Aldo M. Serenelli, and Sarbani Basu. 10,000 standard solar models: A Monte Carlo simulation. *The Astrophysical Journal Supplement Series*, 165:400–431, July 2006.
- [54] Martin Asplund, Nicolas Grevesse, and A. Jacques Sauval. The solar chemical composition. *Nuclear Physics A*, 777:1–4, 2006.
- [55] Sarbani Basu and William J. Chaplin et al. Solar abundances and helioseismology: Fine-structure spacings and separation ratios of low-degree p-modes. *The Astrophysical Journal*, 665:660–671, 2007.

- [56] J. Bahcall, M. Gonzalez-Garcia, and Carlos Pena-Garay. Does the sun shine by pp or CNO fusion reactions. *Physical Review Letters*, 90(13):131301–131304, 2003.
- [57] Cristiano Galbiati and Andrea Pocar et al. Cosmogenic  $^{11}\text{C}$  production and sensitivity of organic scintillator detectors to pep and CNO neutrinos. *Physical Review C*, 71, 2005.
- [58] J. Bahcall. Why do solar neutrino experiments below 1 MeV. *Low Energy Solar Neutrino Detection*, pages 172–176, 2001.
- [59] H. Back and BOREXINO Collaboration. CNO and pep neutrino spectroscopy in BOREXINO: Measurement of the deep-underground production of cosmogenic  $^{11}\text{C}$  in an organic liquid scintillator. *Physical Review C*, 74, 2006.
- [60] Osvaldo Civitarese, editor. *Nd double beta decay search with SNO+*, volume 942, Prague, Czech Republic, July 2007. Workshop on calculation of double-beta decay matrix elements, American Institute of Physics.
- [61] H. N. Pollack, S. J. Hurter, and J. R. Johnson. Heat loss from the Earth’s interior: analysis of the global data set. *Reviews of Geophysics*, 31(3):267–280, 1993.
- [62] C. Kraus for the SNO+ collaboration. SNO with liquid scintillator: SNO+. *Progress in Particle and Nuclear Physics*, 57:150–152, 2006.
- [63] Chunlin Lan. SNO+ and geoneutrino physics. Master’s thesis, Queen’s University, 2007.
- [64] Petresa Canada. Petresa canada: Our products. <http://www.petresa.ca/en/produit.asp>, 2002.

- [65] G. Heusser. Low radioactivity background techniques. *Annual Review of Nuclear and Particle Science*, 45:543–590, 1995.
- [66] Y. Kishimoto. Liquid scintillator purification. In Bruce Cleveland, Richard Ford, and Mark Chen, editors, *AIP Conference Proceedings*, volume 785, 2005.
- [67] J. Busenitz et al. Proposal for US participation in KamLAND. [http://bama.ua.edu/~andreas/ps\\_files/kamland\\_prop.pdf/](http://bama.ua.edu/~andreas/ps_files/kamland_prop.pdf/), 2003.
- [68] A. Ianni, D. Montanino, and F.L. Villante. How to observe  $^8\text{B}$  solar neutrinos in liquid scintillator. *Physics Letters B*, 627:38–48, 2005.
- [69] Jose Maneira. External background in SNO+. SNO+ Internal Documents, August 2007.
- [70] B.C. Guo, J.W. Purnell, and A.W. Castleman Jr. The clustering reactions of benzene with sodium and lead ions. *Chemical Physics Letters*, 168(2):155–160, April 1990.
- [71] Richard Taplin. *The Use of Photomultipliers in SNO*. PhD thesis, Oxford University, 1995.
- [72] T.C. Andersen and R.A. Black et al. A radium assay technique using hydrous titanium oxide adsorbent for the Sudbury Neutrino Observatory. *Nuclear Instruments and Methods in Physics Research A*, 501:386–398, 2003.
- [73] S.J. Setford. *A Basic Introduction to Separation Science*. Rapra Technology Limited, 1995.